UNIVERSITÉ DE LILLE

Doctoral School **ED SMRE**
University Department **Laboratoire de Physique des Lasers, Atomes et Molécules (PhLAM)**

Thesis defended by

Florent BESSIN

on 21st november 2019

In order to become Doctor from Université de Lille

Academic Field **Physics**
Specialty **Optics and Lasers, Physical Chemistry, Atmosphere**

Experimental observation of different forms of modulation instability in passive fiber cavities

Thesis supervised by	Arnaud MUSSOT	Directeur
	Matteo CONFORTI	Co-directeur

Committee members

Chairman	Alexandre KUDLINSKI	Université de Lille
Referees	Massimo GIUDICI	Université Côte d'Azur
	Costantino DE ANGELIS	Università degli studi di Brescia
Examiners	Julien FATOME	Université de Bourgogne-CNRS
	Alessia PASQUAZI	University of Sussex
	Auro Michele PEREGO	Aston University
Supervisors	Arnaud MUSSOT	Université de Lille
	Matteo CONFORTI	Université de Lille - CNRS

UNIVERSITÉ DE LILLE

École doctorale **ED SMRE**
Unité de recherche **Laboratoire de Physique des Lasers, Atomes et Molécules (PhLAM)**

Thèse présentée par

Florent BESSIN

le 21 Novembre 2019

En vue de l'obtention du grade de docteur de l'Université de Lille

Discipline **Physique**
Spécialité **Optique et Lasers, Physico-Chimie, Atmosphère**

Observation expérimentale de différentes formes d'instabilité de modulation dans les cavités fibrées passives

Thèse dirigée par	Arnaud MUSSOT	Directeur
	Matteo CONFORTI	Co-directeur

Composition du jury

Président	Alexandre KUDLINSKI	Université de Lille
Rapporteurs	Massimo GIUDICI	Université Côte d'Azur
	Costantino DE ANGELIS	Università degli studi di Brescia
Examinateurs	Julien FATOME	Université de Bourgogne-CNRS
	Alessia PASQUAZI	University of Sussex
	Auro Michele PEREGO	Aston University
Directeurs de thèse	Arnaud MUSSOT	Université de Lille
	Matteo CONFORTI	Université de Lille - CNRS

ABSTRACT/RÉSUMÉ

Abstract: Modulation instability (MI) in optics is a nonlinear process where a weak periodic perturbation exponentially grows at the expanse of a strong carrier wave as a result of the perfect balance between dispersion and non-linearity. In passive optical cavities, the coherent superposition between the driving field and the intra-cavity field adds a extra-degree of freedom to this mechanism that enriches its dynamics. In this thesis, we mostly led experimental study of MI in such devices made of optical fibers in unexplored regimes. In particular, we experimentally investigated this process in cavities that operate under weak normal dispersion. We showed that the MI dynamics in such regime is strongly modified compared to standard MI in cavities. We also studied the real-time dynamics of MI in the temporal domain highlighting that the generated temporal pattern can exhibit two distinct behaviors. A part of this work is also dedicated to the experimental study of the gain through loss mechanism. Under specific conditions this process can generate MI and tunable optical frequency combs. These studies are in pretty good agreement with theoretical models and numerical simulations. Finally, we explored analytically the process of coherent seeded MI. We reported that the dynamics of the process is phase-sensitive, which was confirmed experimentally by recording the power and phase evolution of the waves involved in the process.

Keywords: Nonlinear optics; optical fiber; passive fiber cavities; modulation instability

Résumé: L'instabilité de modulation (IM) en optique est un processus non-linéaire responsable de l'amplification exponentielle d'une faible perturbation périodique au dépend d'une onde porteuse de forte puissance, cela en raison du parfait équilibre entre la dispersion et la non linéarité. Dans les cavités optiques passives, la superposition entre le champ injecté dans le système et le champ intra-cavité ajoute un degré de liberté supplémentaire à ce mécanisme, ce qui enrichit sa dynamique. Dans cette thèse, nous avons principalement mené des études expérimentales de l'IM dans de tels dispositifs faits de fibres optiques, dans des régimes inexplorés. En particulier, nous avons étudié expérimentalement ce processus dans des cavités fonctionnant en régime de dispersion faible. Nous avons montré que la dynamique de l'IM dans un tel régime est fortement modifiée par rapport à celle de l'IM standard dans les cavités. Nous avons également étudié la dynamique temporelle de l'IM montrant que le motif temporel généré peut présenter deux comportements distincts. Une partie de ces travaux est également consacrée à l'étude expérimentale du mécanisme de gain induit par les pertes. Dans des conditions spécifiques, ce processus peut générer de l'IM ainsi que des peignes de fréquence ajustables. Ces études sont en bon accord avec les modèles théoriques et les simulations numériques. Dans la dernière partie de ce travail, nous avons exploré analytiquement le processus de l'IM amorcée de façon cohérente. Nous avons montré que la dynamique du processus est sensible à la phase, ce que nous confirmons expérimentalement en enregistrant l'évolution de la puissance et de la phase des ondes impliquées dans le processus.

Mots clés: Optique non-linéaire ; fibres optiques ; cavités fibrées passives ; instabilité de modulation

Remerciements

Je tiens tout d'abord à remercier les membres du jury, Massimo Giudici, Professeur à l'Université Côte d'Azur, Costantino De Angelis, Professeur à l'Université de Brescia, Julien Fatome, Ingénieur de recherche au CNRS à l'Université de Bourgogne, Alessia Pasquazi, Professeure associée à l'Université de Sussex, et Auro Mitchele Perego, Post-doctorant à l'Université d'Aston qui ont accepté d'évaluer, questionner et discuter mon travail.

J'adresse également un très grand merci à mes encadrants : à Arnaud Mussot avec qui j'ai énormément appris, merci pour tous ses encouragements à me dépasser, pour sa patience et ses conseils toujours très avisés afin de me faire progresser, en particulier dans ma manière d'expliquer et de présenter. A Matteo Conforti pour avoir toujours eu la patience de m'expliquer des points de théories obscures pour moi et de m'avoir guidé dans mes démarches "calculatoires" sans queue ni tête. Merci enfin à Alexandre Kudlinski qui m'a offert la possibilité de réaliser mon stage de fin de master dans l'équipe photonique sans quoi je ne me serais pas orienté vers cette thèse.

Je remercie également mes collègues qui m'ont supporté tout au long de ces trois années de thèse, à commencer par les marins avec qui j'ai navigués dans le triangle des Bermudes (de Lille) : à Carlos Mas Arabí avec qui j'ai affronté à vélo les pavés du Paris-Roubaix et le Mont-Saint-Aubert, et à Corentin Naveau critique culinaire spécialisé dans la carbonnade flamande qui m'a hébergé le jour où j'ai perdu mes clés d'appartement. Merci également à François Copie pour ne pas avoir posé de questions à ma soutenance et avoir effacé mes dettes de bières. Je remercie aussi Gang Xu pour les sorties au restaurant chinois, Tomy Marest le normand-picard en chaussette au bureau et Guillaume Vanderhaegen "l'autre de Phelma".

Merci aussi aux autres membres du groupe photonique et du laboratoire Phlam, à Maryna Kudinova la voleuse de desserts, à Patrick Bulot le spécialiste du thé et des gâteaux cuit sans four, à Monika Bouet pour les Makocz maison, ta bonne humeur toujours agréable au bureau 105 et toutes ces petites discussions sympas qu'ont eues, à Marie Fournier (désolé si je t'ai fait peur avec mon stress sur la fin de la rédaction) pour les pauses au P5 et les sorties (plage de Dunkerque en particulier), et tous les autres, Rémi, Stéphane, Karen, Géraud (pour les petites piques), Andy, Laurent, Esben, Yves, Arsène, Javier, Rémy, Damien, Laure (merci pour les réseaux de Bragg), Emeric, Benjamin, Jean, Aurélie ... Et ceux que j'oublie avec qui j'ai passé de bons moments.

Je tiens particulièrement à remercier Auro Mitchele Perego pour cette collaboration fructueuse que nous avons eue au cours de ma thèse et qui ne semble pas finie.

Je ne peux oublier de remercier Gilbert Martilleni qui m'a offert la possibilité d'enseigner et avec qui j'ai eu des discussions passionnantes sur l'enseignement, Pascal Szriftgiser pour tous ses conseils et son aide qu'il a apportée à Corentin et moi ainsi que les prêts de matériels qui ont été décisifs. Je remercie aussi Michaël Fromager, mon prof de physique optique en licence qui a suscité chez moi le déclic qui m'a donné envie et persuadé de continuer dans ce domaine.

Je voudrais aussi remercier Samuel Ladvenu mon ami d'enfance, toujours là pour me supporter, me proposer une bière, et écouter de la science dont il préfèrerait se passer, Charlotte Roussel la collectionneuse de sous-bocks qui vérifie toujours si je suis bien rentré chez moi, ainsi que mes amis de fac Freddie Delépine, Gwendoline Thomas, et tous les autres.

Je remercie ma famille pour l'immense soutien qu'ils m'ont apporté, en particulier mes parents qui ont suivi l'écriture de mon manuscrit jour après jour et son probablement maintenant expert en “saddle point”, mon frère Paul et ma sœur Zoé pour tous leurs conseils et encouragements, je retiens en particulier la phrase “tu n'as jamais été aussi proche de la fin”.

Enfin, je me dois de mentionner les services en ligne Google Traduction, Linguee et Reverso, sans quoi ce manuscrit serait moins compréhensible.

REMERCIEMENTS

Contents

Acronyms and abbreviations

AO acousto-optical modulator

ASE amplified stimulated emission

BPF band-pass filter

CS cavity soliton

CW continuous wave

DC direct current

DFT dispersive Fourier transform

DSF dispersion shifted fiber

EBPF electronic band-pass filter

EDFA erbium doped fiber amplifier

EM electro-magnetic

EOM electro-optical modulator

FBG fiber Bragg grating

FOD four-order dispersion

FSR free spectral range

FWM four wave mixing

GNLSE general nonlinear Schrödinger equation

GTF gain-through-filtering

GTF gain-through-loss

GVD group velocity dispersion

HOD high-order dispersion

LLE Lugiato-Lefever equation

LNA low-noise amplfier

MI modulation instability

NLSE nonlinear Schrödinger equation

ODE ordinary differential equation

OFC optical frequency comb

OSA optical spectrum analyzer

Oscillo. oscilloscope

PBS polarization beam splitter

PC polarization controller

PD photodetector

PID proportional-integrate-derivate controller

PR parametric resonance

Pulse Gen. pulse generator

P$_W$M powermeter

PZT piezoelectricity

RF radio-frequency

RFA radio-frequency amplifier

SBS stimulated Brillouin scattering

SGF super gaussian filter

SMF single mode fiber

SOA semiconductor optical amplifier

SRS stimulated Raman scattering

STR fiber stretcher

SVEA slowly varying envelop approximation

Synth. synthesizer

TOD third-order dispersion

TWM three wave model

WS waveshaper

ZDW zero dispersion wavelength

Introduction

Through the long history of optics, it was commonly though that the interaction between an electro-magnetic (EM) field and matter was linear. Such assumption implies that part of the incident EM field on an optical medium cannot be converted to other frequencies and that the refractive index of this medium is independent to an EM field and its intensity. However, J. Kerr demonstrated in 1875 that this assumption was wrong. He discovered that the application of an electric field on organic liquids and glasses induces a change of the refractive index of the medium (birefringence). More than a half century latter, new nonlinear optical phenomena based on direct light-matter interaction were predicted, such as two-photon absorption by M. Göppert-Mayer [1] and the Raman effect [2] observed in 1928 [3]. Nonetheless, the nonlinear response of a medium to light generally requires a high intensity and during the following decades nonlinear optics, except some studies [4], remains an unexplored curiosity. In 1960, the invention of the laser by T. Maiman [5] led to significantly new possibilities in nonlinear optics, by providing sufficient photon density to explore new nonlinear effects. A year later, the second-harmonic generation was observed for the first time by P.A. Franken [6] and two-photon absorption by W. Kaiser [7]. That was soon followed by the discoveries of other nonlinear effects, such as stimulated Raman scattering (SRS) [8], intensity dependent refractive index to light [9], stimulated Brillouin scattering (SBS) [10] and four-wave mixing (FWM) [11].

The laser discovery did not only impact optical studies in bulk media, but also paved the way to studies in optical fibers in the 1960's [12–14]. Indeed, the laser provides the potential to generate a large amount of light in a spot tiny enough to be focused in the core of an optical fiber. In the early 1960's, optical fibers were used as gain medium to build lasers [12–14], but soon after, it was predicted that such optical components could be used as potential transmission media for laser communication, by keeping the loss under 20 dB/km [15]. However, it took until the early 1970's to see the emergence of such "low-loss" fibers [16], leading to the development of optical communications and at the same time to the investigation of nonlinear fiber optics. In these fibers, the high photon density provided by a laser can be confined in a core of small diameter, over a long distance, which exacerbates the light-matter interaction and therefore nonlinear effects. Soon after, various nonlinear optical processes in such optical fibers were demonstrated by R. H. Stolen *et al.*, including

SBS [17], SRS [18], self-phase modulation [19], the optical Kerr effect [20], and FWM [21, 22]. These works were followed by the generation of optical solitons in optical fibers [23–25].

In 1966, V. I. Bespalov *et al.* and L. A. Ostrovskii the next year predicted that one of the most ubiquitous nonlinear phenomenon observed in the nature [26], in various fields of physics ranging from hydrodynamics [27] to plasma physics [28], discrete nonlinear systems [29], and Fermi-resonant interface waves [30], could be observed in optics in diffractive [31] and dispersive [32] media, respectively. This phenomenon called *Modulation instability* (MI) was first observed in optical fibers in the early 1980's by A. Hasegawa *et al.* [33]. They showed that in the context of optics, MI occurs when a weak periodic optical perturbation grows exponentially at the expense of a strong carrier optical wave because of the interplay between the chromatic dispersion and non-linearity. In the temporal domain, it results in the formation of a periodic pattern and in the spectral domain to the birth of symmetrical sidebands on both sides of the pump frequency. In 1985, this mechanism was observed for the first time in optics, in a single-mode optical fiber [34,35] by using a mode-locked laser. Then, MI in optics was intensively studied since it is known as the main mechanism for the generation of optical solitons [23, 24], supercontinuums [36] and rogues waves [37, 38].

Over the same period, nonlinear optics in passive cavities attracted a lot of attention because of the strong enhancement of nonlinear effects allowed by the multiple passes in the nonlinear medium. First investigations demonstrated that the coherent interaction between the input field and the circulating field inside the cavity does not only enhance nonlinear effects but induces a more complex dynamics such as optical multi-stability, instabilities, chaos and self-oscillations [39–50]. In the late 1980s, MI was observed for the first time in these devices made of fiber by M. Nakazawa *et al.*. However, this experiment was performed without any stabilization to external perturbations to which the system is highly sensitive due to its interferometric nature. In the beginning of the following decade, M. Haelterman *et al.* investigated theoretically MI in synchronously pumped passive cavities operating under stable conditions. They highlighted that MI in such devices leads to the formation of stationary dissipative self-oscillations, contrary to the single pass configuration. Moreover, they demonstrated that the dynamics of this process was strongly modified by the boundary conditions imposed by the periodicity of the system. These theoretical predictions were first observed by S. Coen *et al.* [51, 52], soon followed by experimental evidences of new features of this process like the bistable switching [53, 54] and the generation of ultra-high repetition rate pulse trains [55].

During the last years, passive nonlinear optical fiber-ring cavities were intensively studied, mostly because they support temporal cavity solitons (CSs) [56]: an optical structure that can persist indefinitely without any active gain. These CSs can be independently addressed (turned on or off), thus attracting a lot of attention for generating bits in all optical buffers or optical array processors [57]. More recently, temporal CSs have also been widely studied in microresonators, especially because their counterpart in the spectral domain corresponds to the the formation of broad Kerr optical frequency combs (OFCs) thanks to the high confinement of light. These OFCs, which can even reach an octave [58, 59], found a wealth of applications ranging from metrology [60, 61] with lidars [62], astrophysics for calibration the astronomical spectrometers used to detect Earth-like extra-solar planets [63, 64], to ultra-precise spectroscopy and molecular fingerprinting [65–67]. The generating mechanism of these OFCs (and CSs) relies on MI, which first initiates the exponential growth of sidebands around the pump. Then, subsequent FWM processes lead to the generation of additional lines. Characteristics of the generated OFCs strongly depend on their early stage of formation and a perfect knowledge of MI dynamics is essential to optimize their performances (span, stability, spacing between lines) [68–70]. However, in most of the cases, the fast dynamics of MI in microresonators cannot be experimentally recorded [71, 72]. Indeed, their round-trip time is not compatible with state-of-the-art electronic equipment. Conversely, the study of the formation of MI in passive fiber-ring cavities has many advantages. On the one hand, they are straightforward to construct and can be easily stabilized to external perturbations. On the other hand, thanks to their long cavity length (large round-trip time), the round-trip to round-trip MI dynamics can be recorded with state-of-the-art electronic equipment. Note that both microresonators and passive fiber-ring cavities are ruled by the same physics. Passive fiber cavities are thus the perfect platform to understand the formation of MI in microresonators.

The present work focuses on the study of MI dynamics in passive fiber-ring cavities. We studied this process in specific regimes that remain experimentally unexplored. In particular, we focused our investigations on the observation of (i) the MI process in the weak normal dispersion region, (ii) the real-time dynamics of MI in the temporal domain as well as (iii) the real-time dynamics and phase-sensitivity of coherent seeded MI and (iv) the generation of MI, based on the process of gain-through-filtering (GTF). These experimental observations are compared to theoretical investigations and numerical simulations with a pretty good agreement. This fundamental work provides promising results for suitable applications related to passive resonators, in particular for the generation of tunable OFCs.

The manuscript is organized as follows.

In chapter 1, we give an overview of the fundamental concepts by describing light propagation in passive fiber cavities. In particular, we recall a simple mathematical model that allows to describe the MI dynamics in such cavities. We end up this chapter with the experimental implementation, by highlighting the techniques used to drive and stabilize the cavity. Chapter 2 is dedicated to the experimental study of MI in the weak normal dispersion region of passive fiber-ring cavities. We show that under such condition, higher order dispersion terms must be taken into account in order to accurately describe the whole dynamics of MI. In chapter 3, we study experimentally the round-trip to round-trip dynamics of MI in the temporal domain.

We show that MI can follow two distinct regimes: (i) the temporal pattern being either in phase or, more surprisingly, (ii) out-of-phase round-trip to round-trip. In chapter 4, we study experimentally the generation of a new kind of instability in cavities triggered by the process of gain-through-filtering. Finally, in chapter 5 we study theoretically the coherent seeded MI in passive cavities, by showing that the dynamics is sensitive to the phase of the input components. We provide experimental evidences of such phenomenon through heterodyne measurements of the process.

Chapter 1

Passive fiber cavities: fundamental concepts

Contents

This first chapter is an overview of the fundamental concepts describing light propagation in passive fiber cavities. The first section focuses on single pass configurations and lists the main effects suffered by optical fields in an optical fiber. Then, in a second section, we introduce the concept of passive cavities and we describe field propagation in such architectures, which becomes more complex due to the periodic feedback. The next section develops a mathematical approach to extract a simple model that allows the characterization of the field dynamics in such a system. Finally, we introduce the experimental setup already built at the beginning of this thesis that has been up-graded along the way.

1.1 Light propagation in optical fibers

Optical fibers, in their most basic form, consist in a cylinder of glass of higher refractive index surrounded by a cladding of lower refractive index. In such fibers, called step-index fibers, the phenomenon of total internal reflection [73] confines the light inside the core. In this thesis, we mainly used standard telecommunication fibers and dispersion shifted fibers (DSF) supporting a single transverse mode. In the following, we detail the main phenomena undergone by the light pulses propagating in these fibers, and more specifically in passive fiber cavities.

1.1.1 Losses

When light propagates in an optical fiber, the signal experiences losses. They come mainly from intrinsic absorption of the material: Rayleigh scattering, which becomes important at short wavelengths, and infrared adsorptions at long wavelengths [74]. This attenuation is quantified by the attenuation constant α_f (in m^{-1}), linking the input power P_0 launched in a fiber to the transmitted power P_T over a propagation of length L, by the relation $P_T = P_0 \exp(-\alpha_f L)$ [75]. In silica fibers, the minimum of losses is about 0.2 dB/km (4.5×10^{-5} m^{-1}, record: 0.1419 dB/km in 2018 [76]) at 1.55 µm, the central wavelength of the telecommunication C band.

1.1.2 Chromatic dispersion

Chromatic dispersion consists in the frequency dependence of the refractive index $n(\omega)$ of dielectric media such as silica. Fundamentally, this dependence is characterized by the resonance frequencies where the medium absorbs the electromagnetic wave. To describe this process we introduce the slowly varying envelope approximation (SVEA), implying that the spectral width of the signal ($\Delta\omega$) is really thin compared to the carrier frequency ω_0 ($\Delta\omega \ll \omega_0$). Within the framework of this assumption, we can expand the mode propagation constant $\beta(\omega)$ in a Taylor series around ω_0 such as [75]:

$$\beta(\omega) = \frac{n(\omega)\omega}{c} = \beta_0 + \beta_1(\omega-\omega_0) + \frac{\beta_2}{2}(\omega-\omega_0)^2 + \text{High order terms} \tag{1.1}$$

$$\text{High order terms} = \sum_{n>2} \frac{\beta_n}{n!}(\omega-\omega_0)^n \tag{1.2}$$

$$\beta_n = \left(\frac{d^n\beta}{d\omega^n}\right)_{\omega=\omega_0}, (n = 0, 1, 2, ...) \tag{1.3}$$

where β_n are the dispersive constants of the material that can be calculated from the Sellmeir formula [75]. The parameter β_1 represents the inverse of the group-velocity (expressed in ps/km), velocity at which the envelope of the wave propagates, and β_2 is the group-velocity dispersion (GVD expressed in ps^2/km). This latter term is responsible for the temporal broadening of pulses during the propagation, since the different spectral components do not propagate at the same velocity. Two cases can be distinguished depending on β_2 sign: (i) the normal dispersion regime ($\beta_2 > 0$) where spectral components with the longest wavelengths propagate faster than short wavelengths, and (ii) anomalous dispersion regime ($\beta_2 < 0$) corresponding to the opposite case. These two regimes can be observed in most silica fibers. The transition between them is characterized by the vanishing of β_2 at a peculiar wavelength called zero-dispersion wavelength (λ_{ZDW}). Typically, in single mode fibers (SMF) the group-velocity dispersion term vanishes at $\lambda_{ZDW} \approx 1.3$ µm. It is worth mentioning that at the vicinity of the zero-dispersion wavelength, high-order dispersion terms (β_3,β_4,...) become significant and must be taken into account in Eq. (1.1) to describe the dispersion effects on pulse propagation.

1.1.3 Nonlinearity: Kerr effect

When light propagates in a dielectric medium, the electric polarization field $\overrightarrow{P}$ depends on the strength of the electric field. The field, in the framework of the SVEA can be written in the form $\overrightarrow{\boldsymbol{E}} = A(z,t)\exp(ikz - i\omega t)\vec{u_z}$ ($\vec{u}_z$ stands for the polarization unit vector) where $k = \omega\left[n' + i\alpha c/(2\omega)\right]/c$. In linear optics, meaning for low optical intensity, this polarization field depends linearly on the electric field such as $\overrightarrow{\boldsymbol{P}} = \overrightarrow{\boldsymbol{P}}_{\mathbf{L}} = \epsilon_0\chi^{(1)}\overrightarrow{\boldsymbol{E}}$, where ϵ_o is the vacuum permittivity and $\chi^{(1)}$ is the linear susceptibility. When the optical power becomes strong enough, the optical response becomes nonlinear with respect to $\overrightarrow{E}$ and a more general function expressing the polarization must be expanded in a power series of the electric field. In silica fibers, it results from the centro-symmetry nature of the medium that the second order susceptibility $\chi^{(2)}$ vanishes. Consequently, the first nonlinear term that becomes significant is the third-order term such as [77]:

$$\overrightarrow{\boldsymbol{P}} = \overrightarrow{\boldsymbol{P}}_L + \overrightarrow{\boldsymbol{P}}_{NL} = \epsilon_0(\chi^{(1)}.\overrightarrow{\boldsymbol{E}} + \chi^{(3)}\vdots\overrightarrow{\boldsymbol{E}}\overrightarrow{\boldsymbol{E}}\overrightarrow{\boldsymbol{E}}) \tag{1.4}$$

where $\chi^{(3)}$ is the third-order susceptibility. For $\Re\left(\chi^{(1)}\right) \gg \Im\left(\chi^{(1)}\right), \left|\chi^{(3)}\right|$, it can be found from the Maxwell equation that the refractive index of the medium depends linearly on the optical intensity [75]. This dependence is usually expressed as $n'(\omega, |A|^2) = n(\omega) + n_2|A|^2$ [78] where $n(\omega) = c\beta\left(\omega\right)/\omega = \sqrt{1 + \Re\left(\chi^{(1)}\right)}$ is the linear and $n_2 = 3\Re(\chi^{(3)})/\left(8n\right)$ the nonlinear refractive index. Note that the losses are given by a linear term that corresponds to $\alpha_f = \Im(\chi^{(1)})\omega/\left(2cn\right)$ and a nonlinear term that corresponds to two-photon absorption. This latter term in silica fiber is relatively small, and we neglect it in the following.

1.1.4 The nonlinear Schrödinger equation

Under the above assumptions it has been demonstrated that the propagation of the field envelope $A(z,t)$ of the optic field in an optical fiber can be described by the nonlinear Schrödinger equation (NLSE) [75]. Note that $A(z,t)$ is in units of the electric field (V.m^{-1}). For practical reasons, we introduce $E = \epsilon_0 nc\left|A\right|^2/2$ such that $\left|E\right|^2$ represents the optical power (in W). In this way, E verifies the following NLSE:

$$\frac{\partial E(z,\tau)}{\partial z} = \left(-\frac{\alpha_f}{2} - i\frac{\beta_2}{2}\frac{\partial^2}{\partial\tau^2} + i\gamma|E(z,\tau)|^2\right)E(z,\tau) \tag{1.5}$$

where $\tau = t - \beta_1 z$ is the time in a reference frame moving at the carrier wave group velocity. The parameter $\gamma(\omega_0) = 2\omega_0\mu_0 n_2/A_{eff}$ is the nonlinear coefficient, where A_{eff} is the mode effective area of the fiber (≈ 80 µm^2 at 1.55 µm for standard single mode fibers). Typically, $\gamma(\omega_0)$ varies between 1 and 10 W^{-1}.km^{-1} in standard fibers and can even be higher in silica micro-structured fibers [79] and chalcogenide fibers [80]. This is the simplest equation describing the field propagation in optical fibers including the third-order nonlinear effect, the GVD and losses. It exists more complex and complete equations taking into account additional effects that could occur simultaneously with Kerr effect. As an example, the generalized nonlinear Schrodinger equation (GNLSE) [75] takes into-account high-order dispersion terms and high order effects such as Raman scattering and self-steepening. The complex mathematical structure of the GNLSE requires generally numerical simulations to be solved and simple analytical solution cannot be found. We point out that we neglected Raman scattering and self-steepening in all the investigations led in this thesis. We used long and weak enough pulses (≈ 1 ns) to not trigger these high order effects.

1.2 Light propagation in passive fiber cavities

1.2.1 Mathematical model

A schematic of the operating principle of passive fiber-ring cavities is depicted in Fig. 1.1. These systems are basically a fiber loop where one of the tip is connected to an input and the other to an output port of a star coupler. The coupler is characterized by its reflection, transmission and excess loss coefficients respectively ρ, θ and η, defined by $\rho^2 + \theta^2 = 1 - \eta^2 = \kappa^2$. Through one of the input coupler port (port on the top left in Fig. 1.1), a fraction ($\theta\kappa = \widetilde{\theta}$, transmitted light by the coupler) of a monochromatic signal is injected inside the cavity. This signal propagates over one round-trip of length L and undergoes chromatic dispersion, Kerr non-linearity, and losses which are accounted by the NLSE (Eq. (1.5)). After one round-trip, this signal coherently interacts with the input field E_{in} inside the coupler. A significant part ($\rho\kappa = \rho'$, reflected light by the coupler) recirculates in the resonator while the other part is extracted through the cavity output (port on the top right in Fig. 1.1). This coherent superposition is described by the boundary condition equations coming from the coupler [81]:

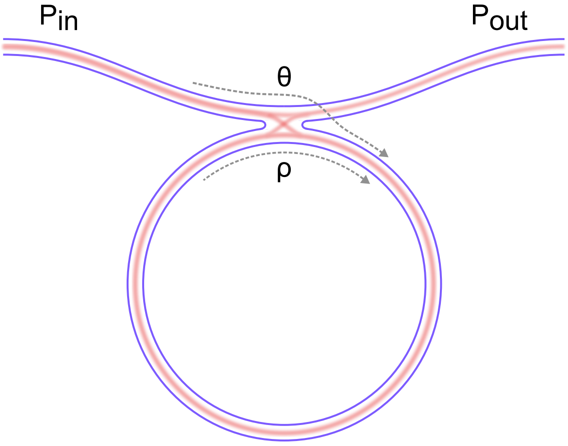

Figure 1.1: Schematic of the operating principle of fiber-ring cavities.

$$\begin{cases} A^{(m+1)}(z=0,\tau) = \widetilde{\theta} E_{in}(\tau) + \rho' A^{(m)}(z=L,\tau)\exp(i\phi_0) & (1.6) \\ E_{out}^{(m+1)}(z=0,\tau) = i\rho' E_{in}(\tau) - i\widetilde{\theta} A^{(m)}(z=L,\tau)\exp(i\phi_0) & (1.7) \end{cases}$$

where the field at the end of round-trip m ($A^{(m)}(z=L,\tau)$) is linked to the field at the beginning of the round-trip $m+1$ ($A^{(m+1)}(z=0,\tau)$) and the cavity output signal ($E_{out}^{(m+1)}(z=0,\tau)$). The term $\phi_0 = \beta_0 L = 2k\pi - \delta_0$ (k integer, $\beta_0 = \omega_0 n/c$) represents the linear phase shift accumulated over one round-trip with δ_0 the detuning of the pump frequency from the closest resonance. We point out that optical fibers we used in this thesis to build cavities are characterized by weak propagation losses

($\alpha_f L < 0.05$ dB) relative to the coupling losses. Consequently, we can perform the substitution $A^{(m)}(z,\tau) \to E^{(m)}(z,\tau)\exp(-\alpha_f z/2)$ such as the full dynamics inside the passive cavity can be described by the following finite-dimensional map:

$$\begin{cases} \dfrac{\partial E^{(m)}(z,\tau)}{\partial z} = i\left(-\dfrac{\beta_2}{2}\dfrac{\partial^2}{\partial \tau^2} + \gamma |E^{(m)}(z,\tau)|^2\right) E^{(m)}(z,\tau) & (1.8) \\ E^{(m+1)}(z=0,\tau) = \widetilde{\theta} E_{in}(\tau) + \widetilde{\rho} E^{(m)}(z=L,\tau)\exp(i\phi_0) & (1.9) \end{cases}$$

where $\widetilde{\rho} = \rho\kappa\exp(-\alpha_f L/2)$. This equation system composed of the NLSE (Eq. (1.5)) and the boundary conditions Eq. (1.7) is also referred to the Ikeda map model [39]. We will see later (section 1.3) that Ikeda map, through some approximations, can be reduced to a single propagation equation, referred to the Lugiato-Lefever equation (LLE) [82].

1.2.2 Steady-state and system resonances

To study this system, the first step is to find steady-states. For this purpose, we search the solution of Eq. (1.8-1.9) where the field is independent of time τ so $\partial^2 E/\partial\tau^2 = 0$. Thus, from Eq. (1.8), we search stationary field inside the fiber as:

$$E^{(m)}(z) = \overline{E}\exp(i\gamma P z)\,,\ P = \left|\overline{E}\right|^2 \tag{1.10}$$

The stationary field condition implied that $E^{(m+1)} = E^{(m)}$ and $E^{(m)}(z=L) = E^{(m)}(z=0)$. By inserting Eq. 1.10 into the boundary condition (Eq. (1.9)), the relation between the field circulating into the cavity and the input pump is (complex field and power):

$$\overline{E} = \frac{\widetilde{\theta} E_{in}}{1-\widetilde{\rho} e^{i\phi}} \tag{1.11}$$

$$\frac{P}{P_{in}} = \frac{\widetilde{\theta}^2}{1+\widetilde{\rho}^2 - 2\widetilde{\rho}\cos(\phi)} \tag{1.12}$$

where $\phi = \gamma L P + \phi_0$ is the total phase shift imposed by the cavity and $P_{in} = |E_{in}|^2$. Similarly, by inserting Eq. (1.10) into the output boundary condition Eq. (1.7) and by applying the substitution $E^{(m)}(z,\tau) \to E^{(m)}(z,\tau)\exp(-\alpha_f z/2)$, we can express the output stationary field (complex field and power):

$$\overline{E}_{out} = \frac{iE_{in}\left[\widetilde{\rho} e^{\alpha_f L/2} - \kappa^4 e^{-\alpha_f L/2 + i\phi}\right]}{1-\widetilde{\rho} e^{i\phi}} \tag{1.13}$$

$$\frac{P_{out}}{P_{in}} = \kappa^4 - \left[1-\kappa^4 e^{-\alpha_f L}\right]\frac{P}{P_{in}} \tag{1.14}$$

where $P_{out} = |\overline{E}_{out}|^2$. Note that with those notations ($\tilde{\theta}$ and $\tilde{\rho}$), that include excess losses of the coupler and propagation losses, the steady-state equations (1.12-1.14) are identical to those of standard Fabry-Pérot resonators [83].

1.2.2.1 Linear resonances

As a first step, we study the Fabry-Perot-like functions Eqs. (1.12-1.14), when the cavity operates in the linear regime ($\phi = \xcancel{\gamma LP} + \phi_0$). We report examples of the cavity response function P/P_{in} versus ϕ_0 for $\theta^2 = 0.05$ in Fig. 1.2(a) depicted with a blue curve. We note that these curves correspond to 2π-periodic Airy functions of ϕ_0. The maxima of $P/P_{in} = f(\phi_0)$ is obtained for $\phi_0 = 2k\pi$ ($k \in \mathbb{Z}$), when the input field and the recirculating field are in phase. These phase values, where the intra-cavity power is maximum, defines the resonances of the system. From the previous definition of the linear phase introduced in section 1.2.1, we note that the linear phase is proportional to the pump frequency f_0 ($\phi_0 = 2\pi f_0 nL/c$). Thus, resonances of the system corresponds to specific frequencies that are spectrally equally spaced. This frequency spacing is called the *free spectral range* (FSR) and is equal to $c/(nL)$. Then, we investigate how the value of θ affects this functions. For this purpose, we superimposed the function $P/P_{in} = f(\phi_0)$ obtained for $\theta^2 = 0.1$ and 0.2 in Fig. 1.2(a) with green and red curves, respectively. We observe that the resonances become thinner and their amplitudes increase with decreasing losses. In the good cavity limit ($\widetilde{\rho} \approx 1$), and for $\delta_0 = 2m\pi - \phi_0 \ll 1$ ($m = \arg\min_n |2n\pi - \phi_0|$) we find

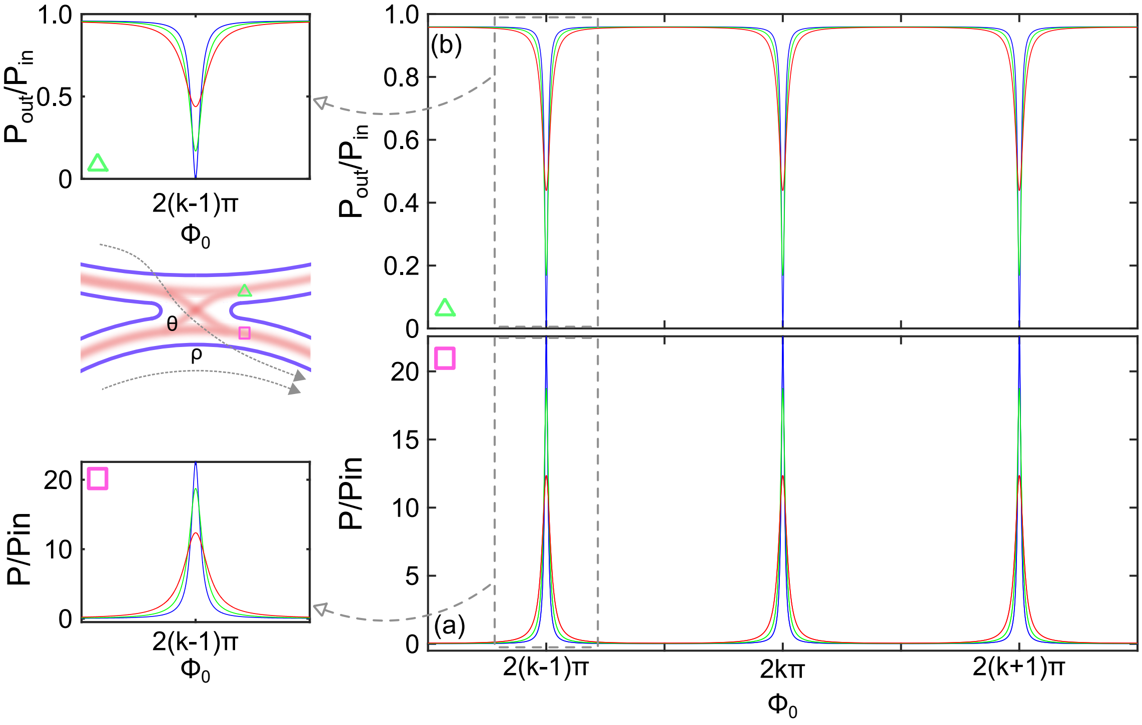

Figure 1.2: Linear resonances of a passive cavity for (a) intra-cavity cavity response (Eq. (1.12)) and (b) output cavity response (Eq. (1.14)). The red, green and blue lines are obtained for $L = 50$ m, $P_{in} = 1$ W and $\theta = \sqrt{0.2}$, $\sqrt{0.1}$, $\sqrt{0.05}$ ($\mathcal{F} \approx 67$, 44, 25), respectively.

that Eq. (1.12) becomes:

$$\frac{P}{P_{in}} = \frac{\tilde{\theta}^2}{\alpha^2 + \delta_0^2} \tag{1.15}$$

where we introduce $\alpha = 1 - \widetilde{\rho}$ that accounts for the overall losses over a cavity round-trip. This approximation of Eq. (1.12) is really useful, it provides an estimation of the overall losses α through parameters that can be recorded in experiments. Indeed, the ratio between the FSR and the full width at half maximum of this lorentzian function (of a resonance) called the *cavity finesse* is given by $\mathcal{F} \approx \pi/\alpha$. In practice, with such a cavity architecture, we cannot access to the intra-cavity field and record the intra-cavity response function. However, we have a direct access to the field at the cavity output, and its transfer function $P_{out}/P_{in} = g(\phi_0)$ follows the opposite evolution of the intra-cavity transfer function. We report examples of this cavity response for $\theta^2 = 0.05$, 0.01 and 0.2 in Fig. 1.2(b), with blue, green, and red curves, respectively. From an experimental point of view, we measure from this function the cavity finesse that follows the same previous enunciated definition, and then determinate the overall cavity losses.

1.2.2.2 Resonances in nonlinear regime: impact of Kerr effect

To go further, we investigate the impact of non-linearity on these resonances. When the pump becomes strong enough, in Kerr nonlinear medium, the nonlinear part in the phase term ϕ becomes significant with respect to the linear part and adds an additional phase shift at each round-trip $\phi_{NL} = \gamma L P$. This term modifies the

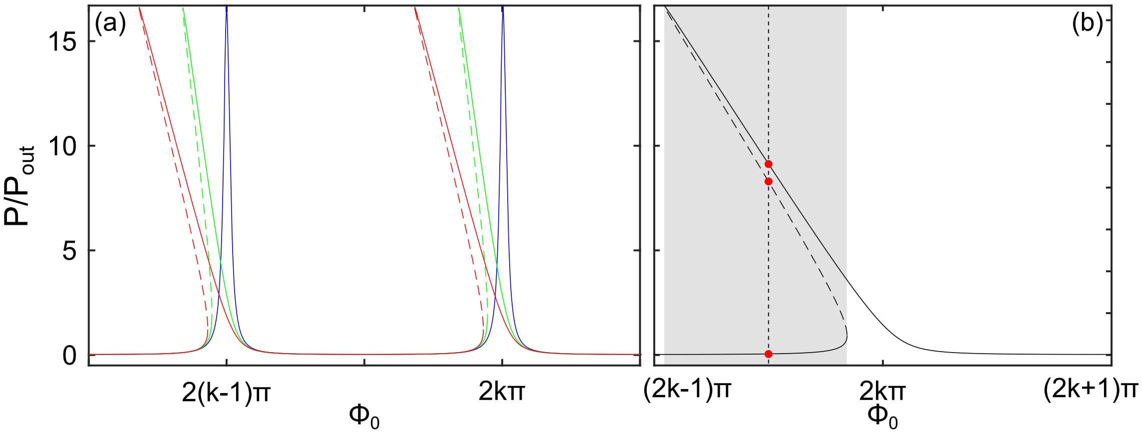

Figure 1.3: (a) Nonlinear resonances for three different input pump powers. Blue, red and green lines are obtained for $P_{in} = 0.01$, 1, 2 W, respectively. Solid lines and dashed lines stand for stable and unstable homogeneous solutions, respectively. (b) Nonlinear resonances for $P_{in} = 0.01$ W. Gray area corresponds to multi-valued domains. Red dots stands for steady-state values for $\phi_0 = (2k - 1/2)\pi$ (black dashed line). Parameters: $L = 50$ m, $\theta = \sqrt{0.1}$, $\gamma = 1.2$ W^{-1}.km^{-1}.

shape of the resonances and shifts their peaks to negative values ($\phi_{NL,peaks} = \gamma L P_{in}$). To illustrate this behavior, we plot in Fig. 1.3(a) the cavity response function (Eq. (1.12)) versus the linear phase ϕ_0 for three different values of P_{in}. Blue, green, and red lines stand for $P_{in} = 0.01$, 1, 2 W, respectively. We note that resonances become more and more tilted as the input power is increased. Moreover, for sufficiently large shifts of the peak resonances, the response becomes multi-valued (green and red curves) on certain domains of ϕ_0. We plot in Fig. 1.3(b) an example of this case, where three intra-cavity powers exist satisfying the steady-states equation 1.12 on the gray domain (see red dots). We will see further that steady-states that belong to the intermediate branch of the resonances (dashed lines) are unstable. Finally, if the displacement of peak resonances exceeds the phase spacing between resonances, the system can exhibit more than three steady-state solutions. Such cases present a complex dynamics [84, 85] that was not investigated in this thesis.

1.3 Lugiato-Lefever Equation

Due to the complex mathematical structure of the map system Eqs. (1.8-1.9), it is difficult to find an analytical description to study the cavity dynamics. Nevertheless, it has been shown that for cavity with high finesse, the system of coupled difference-differential equations Eqs. (1.8-1.9) can be reduced to a single partial differential equation [86], which strongly simplifies analytic investigations of the system dynamics. This equation called Lugiato-Lefever Equation (LLE) [82] is given by:

$$\frac{\partial E(z,\tau)}{\partial z} = \left(-\frac{\alpha}{L} - i\frac{\delta_0}{L} - i\frac{\beta_2}{2}\frac{\partial^2}{\partial \tau^2} + i\gamma|E(z,\tau)|\right) E(z,\tau) + \frac{\tilde{\theta}}{L}E_{in} \qquad (1.16)$$

It is obtained by assuming that only one longitudinal mode is excited in the framework of the mean-field approximation, which implies that the intra-cavity field between two consecutive round-trips does not evolve significantly. Consequently, all effects undergone by the intra-cavity field over one round-trip must be small. Thus, the overall cavity phase detuning (which includes both linear and nonlinear phase shifts) is of the order of θ^2 or even smaller. Hence, $\delta_0 \ll 1$, $\gamma L P \ll 1$, $\alpha \ll 1$ (high finesse) and the cavity length must be shorter than the dispersion length such that $L_D \approx \left[(\Delta\omega)^2\beta_2/2\right]^{-1} \gg L$ (where $\Delta\omega$ is the total spectral width of the generated spectrum).

1.3.1 Steady-states

We can express the steady-state solution ($\partial^2 E/\partial^2\tau = \partial E/\partial z = 0$) of Eq. (1.16) as follows:

$$E = \frac{\tilde{\theta} E_{in}}{i\left(\delta_0 - \gamma L P\right) + \alpha} \tag{1.17}$$

$$\frac{P}{P_{in}} = \frac{\tilde{\theta}^2}{\left(\delta_0 - \gamma L P\right)^2 + \alpha^2} \tag{1.18}$$

To illustrate theses equations, we plotted in Fig. 1.4(a) with red curves the steady-state solution P/P_{in} versus the detuning δ_0 for three different values of P_{in}. We note from Eq. (1.18) and from Fig. 1.4(a) that the cavity response is a lorentzian function, which becomes more and more tilted as the input power is increased. Note that the x-axis corresponds to the detuning $\delta_0 = -\phi_0 + 2k\pi$ ($k \in \mathbb{Z}$), consequently, the resonances are tilted on the opposite side of resonances depicted in Fig. 1.3, where the x-axis is defined by ϕ_0. To go further, we compared in Fig. 1.4(a) these LLE steady-state solutions (Eq. (1.18)) to the full map steady-state solutions (Eq. (1.12), depicted with blue curves). This LLE response function reproduces quite well only one resonance, but is unable to represent the others. This comes from the initial hypothesis used to derive the LLE model, where we assumed that only one longitudinal mode propagates inside the cavity. Fig. 1.4(b) shows a zoom on Fig. 1.4(a) (delimited by gray dotted lines) that illustrates the limitation implied by this hypothesis. For large enough detunings $|\delta_0| > \pi$ (gray area), or for large enough nonlinear phase shifts, the tilted resonance cover the next resonance (see most tilted

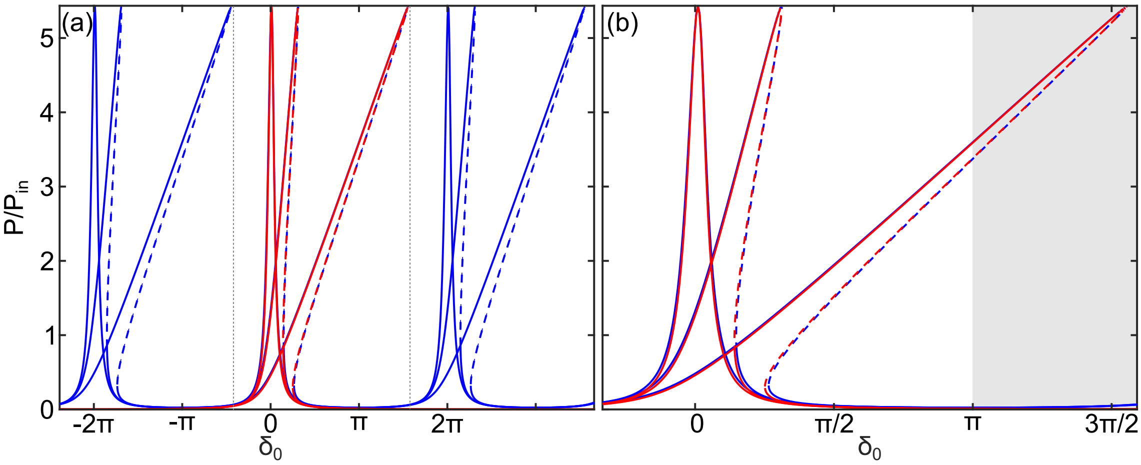

Figure 1.4: (a) Cavity response function from LLE model and Ikeda map model red and blue curves, respectively. (b) Zoom on the central resonance. The corresponding input powers from the less to the most tilted function are respectively $P_{in} = 0.1, 3, 15$ W. Solid lines and dashed lines stand for stable and unstable homogeneous solutions, respectively. Parameters: $\gamma = 1.2$ .W^{-1}.km^{-1}, $L = 50$ m, $\theta = \sqrt{0.1}$ ($\mathcal{F} \approx 25$).

function). Hence, LLE model fails to describe the dynamics since other modes are implied.

1.3.2 Monostability, bistability and stability of cw solutions

By remaining within the validity domain of the LLE, we can go further and study analytically the stability and multi-stability of these stationary states. Indeed, we saw in section 1.2.2.2 that the system exhibits multiple steady-state values for large detunings. However, due to the complex mathematical structure of the cavity response (Eq. (1.12)), it is difficult to find a simple expression giving the range of detunings for which the system is monostable or multi-stable. From this new simple equation (Eq. (1.16)), we can analytically find this critical detuning $\delta_{0,c}$. By actually looking another representation of this response function $P = f(P_{in})$, it can be easily understood how to obtain this critical value. If the detuning is below $\delta_{0,c}$, the system operates in a monostable regime and this curve is an increasing monotonous function. This case is illustrated in Fig. 1.5(a) by the red curve obtained for $\delta_0 = 0$ rad. However, beyond the threshold δ_c, the system becomes multi-valued for a certain range of input powers and the response function display an S-shape curve with a negative slope branch connected to two positives ones. This can be seen from the blue curve in Fig. 1.5(a) ($\delta_0 = 0.5$ rad). Consequently, we can easily find this peculiar detuning by studying the slope of this function. Indeed, for $\delta_0 = \delta_c$ there is only one solution where $dP_{in}/dP = 0$ (see green solid curve in Fig. 1.5(a)). Beyond it, there is two points where $dP_{in}/dP = 0$, which correspond to the knees of the S-shape curve (labeled $P_+$and P_- in Fig. 1.5(a)). For $\delta_0 < \delta_c$ the function $P = f(P_{in})$ increases monotonously. The solutions of $dP_{in}/dP = 0$ are given by:

$$P_\pm = \frac{2\delta_0 \pm \sqrt{\delta_0^2 - 3\alpha^2}}{3\gamma L} \tag{1.19}$$

where $P_\pm$ are the intra-cavity power from respectively the upper and lower knee of the S-shape curve. Consequently, the critical detuning is obtained by imposing $P_+ = P_-$ which gives $\delta_{0,c} = \sqrt{3}\alpha$ (green curve $\delta_0 = \delta_{0,c}$in Fig. 1.5(a)). For the sake of simplicity, we will introduce the normalized detuning $\Delta = \delta_0/\alpha$ that is commonly used in the literature since it allows directly to identify the operating regime. Thus, the critical value for bistable regimes is $\Delta_c = \sqrt{3}$ with this normalization.

In a second step, we will demonstrate that the negative slope of the response function $P = f(P_{in})$ is unstable. This is performed by applying a linear stability analysis of the LLE by adding a small perturbation to the steady-state solution such as $E = E_s + a(0)\exp(\lambda z)$. After linearization around the stationary solutions and straightforward calculations, one finds that homogeneous solutions are unstable whenever the parameter [86, 87]:

$$\lambda = -\frac{\alpha}{L} \pm \sqrt{4\frac{\delta_0}{L}\gamma P - \left(\frac{\delta_0}{L}\right)^2 - 3(\gamma P)^2} \tag{1.20}$$

is positive. By solving the inequality $\lambda > 0$, we find that unstable states exist only in the multi-valued case and correspond exactly to the states belonging to the negative slope of the S-shape curve in the interval $[P_-; P_+]$ (and intermediate branch of the resonance in Figs. 1.3-1.4). Therefore, when $\Delta > \sqrt{3}$ it is usual to talk about a bistable cycle where in the multi-valued range $[P_{in-}; P_{in+}]$ the system presents two stable and one unstable solutions. Note that a similar analysis (details in appendix A) can be performed to study the stability of the steady-states of the Ikeda-map model. It shows that the cw states belonging to the negative slopes of the steady-state curve (and intermediate branch of the resonances in Fig. 1.4) are unstable.

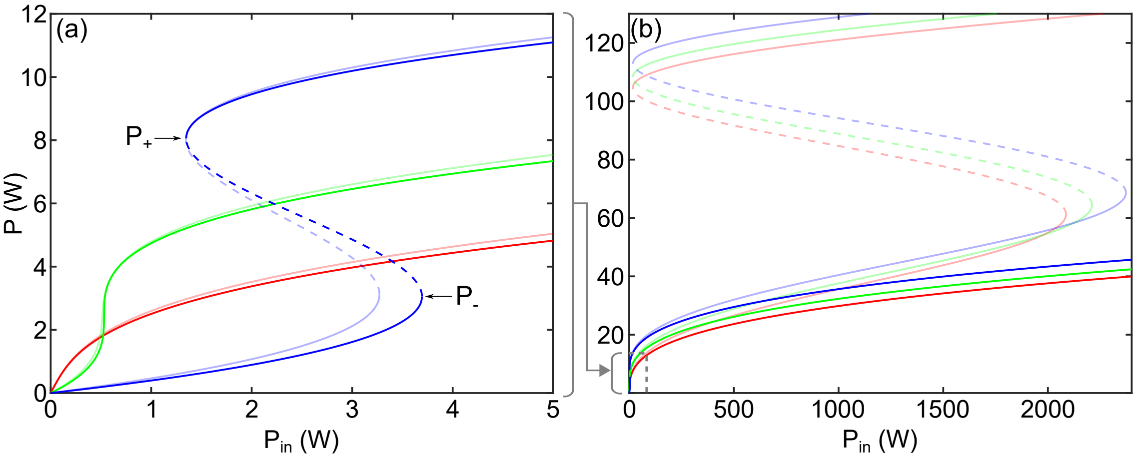

Figure 1.5: (a) Steady-states curves from LLE model (solid lines) and Ikeda map model (shaded lines) for $\Delta = 0$, $\sqrt{3}$, 4, respectively red, green and blue curves. (b) Zoom on gray inset from (a). Dashed lines stand for the cw unstable states.

In Fig. 1.5(a), we superimposed to the representations $P = f(P_{in})$ from LLE model (calculated from Eq. (1.18)) those obtained from Ikeda map model (calculated from Eq. (1.12)) for the same three detuning (shaded red curve $\delta_0 = 0$ rad, shaded green curve $\delta_0 = \delta_{0,c}$, shaded blue curve $\delta_0 = 0.5$ rad). As we note, for low detunings LLE model accurately reproduces the function $P = f(P_{in})$ from the Ikeda map model (see red and green curves in 1.5(a)). However, for higher detunings (see blue curve in Fig. 1.5(a)), especially in bistable regimes, we observe that LLE model fails to describe the lower knee P_-. Note that we also observe the discrepancy between the LLE and the Ikeda map increases with the intra-cavity power. This is even more evident in extreme nonlinear regimes. Fig. 1.5(b) represents the evolution of P for huge values of P_{in}, more than three orders of magnitude of P_{in} in Fig. 1.5(b). We observe that beyond an intra-cavity power threshold that depends on the detuning (in Fig. 1.5(b) $P'_{th} \approx 15,\ 18,\ 20$ W for $\delta_0 = 0,\ \delta_{0,c},\ 0.5$ rad respectively), the LLE model is meaningless.

1.4 Theory of modulation instability

In this section, we describe the process of modulation instability (MI), one of the most ubiquitous nonlinear phenomena observed in the nature [26] in different fields of physics ranging from hydrodynamics [27] to nonlinear optics [32] and plasma physics [28]. In optics, it has been shown that this phenomenon can occur in self-focusing Kerr media. MI originates from the exponential growth of a weak periodic perturbation at the expense of a strong carrier wave, under the combined action of chromatic dispersion and non-linearity. In the temporal domain, it results in the formation of a periodic pattern and, in the spectral domain, in the birth of symmetrical sidebands on both sides of the pump frequency. This effect has been firstly observed in nonlinear fiber optics in 1986 by K. Tai *et al.* [34], in anomalous dispersion region. In the case of normal dispersion, it has been demonstrated that such phenomenon can be achieved only with the help of an extra degree of freedom such as the coupling of two nonlinear orthogonally polarized waves [88], or the influence of additional dispersion terms [89]. MI has also been investigated in cavities, where it has been firstly observed in 1988 by M. Nakazawa *et al.* [90]. It was latter highlighted in 1997 by Coen *et al.* [51] that MI could be extended to normal dispersion region thanks to the extra-degree of freedom provided by boundary conditions imposed by the cavity. MI in passive cavities has also been widely studied in anomalous dispersion, since it operates at the early stage of higher nonlinear structures such as temporal cavity solitons [56]), whose the spectral counterpart corresponds to frequency combs [91]. In the following, we will focus on MI process in passive fiber cavities and we will recall the investigations led in Ref. [86, 87].

1.4.1 Linear stability analysis

The formation of MI can be studied through a linear stability analysis of the LLE. This is performed by looking at the evolution of a perturbed solution $E(z,\tau) = E_0 + a(z,\tau)\exp(i\Omega\tau) + b(z,\tau)\exp(-i\Omega\tau)$, where the steady state E_0 previously established (Eq. (1.18)) is perturbed by a combination of two weak symmetric sidebands located at $\pm\Omega = \pm\omega - \omega_0$ (ω_0 stands for the pulsation of the pump). By linearizing the LLE with respect to $a(z,\tau)$ and $b(z,\tau)$, the Fourier transform of $[a(z,\tau); b^*(z,\tau)]^T$satisfies the following linear system:

$$\frac{\partial}{\partial z}\begin{pmatrix} \tilde{a}(z,\Omega) \\ \tilde{b}^*(z,\Omega) \end{pmatrix} = \begin{pmatrix} i\psi^2 - \dfrac{\alpha}{L} & i\gamma E_0^2 \\ -i\gamma E_0^{*2} & -i\omega^2 - \dfrac{\alpha}{L} \end{pmatrix} \begin{pmatrix} \tilde{a}(z) \\ \tilde{b}^*(z) \end{pmatrix} \tag{1.21}$$

where $\psi = \sqrt{\beta_2\Omega^2/2 + 2\gamma P - \delta_0/L}$ and $\widetilde{f}(\Omega)$ denotes the Fourier transform of $f(\tau)$. As a result, the stability of this system depends on eigenvalues of Eq. (1.21), which are expressed as:

$$\lambda_\pm = -\frac{\alpha}{L} \pm \sqrt{\gamma^2P^2 - \psi^4} \tag{1.22}$$

When one of these eigenvalues has a positive real part, the steady-state cw solution becomes unstable and perturbations grow exponentially with the parametric gain:

$$g(\Omega) = -\frac{\alpha}{L} + \sqrt{\gamma^2 P^2 - \psi^4} \tag{1.23}$$

In the spectral domain, it entails the emergence of bands on each side of the pump. From Eq. (1.23), we find the most unstable frequencies and their corresponding growth rates:

$$\Omega_T = \pm\sqrt{\frac{2}{\beta_2}\left(\frac{\delta_0}{L} - 2\gamma P\right)}, \text{ and } g(\Omega_T) = \frac{-\alpha}{L} + \gamma P \tag{1.24}$$

These unstable frequencies require specific conditions to exist, which will be described in the next section.

1.4.2 Conditions for modulation instability and impact of the group-velocity dispersion

Equations (1.22-1.24) give the conditions under which MI exists inside the cavity. Indeed, MI arises if the parametric gain $g(\Omega_T)$ is positive and if the most unstable frequencies Ω_T are real. We can identify two cases depending on the dispersion sign described in the following two points.

1.4.2.1 Normal dispersion regime ($\beta_2 > 0$)

In the case of normal dispersion regime ($\beta_2 > 0$), MI arises if:

$$\boxed{\beta_2 > 0, \text{ and } P_{th} = \frac{\alpha}{\gamma L} < P < P_\Omega = \frac{\delta_0}{2\gamma L}} \tag{1.25}$$

where P_{th} is the MI cavity threshold imposed by $g(\Omega_T) = 0$ and P_Ω is the threshold above which the solutions Ω_T are complex. We illustrate this case in Fig. 1.6(a) by plotting the maximum of the gain (calculated from Eq. (2.3)) in the (Δ, P) plane. The black horizontal line stands for the MI cavity threshold P_{th} and the red line for the threshold P_Ω. The gray area labeled *"cw unstable states"* corresponds to the homogeneous unstable states (negative slope branch of the bistable curve between the knees P_+ and P_-), colored areas for the modulationally unstable regions and blank areas for the stable domains. From this representation, we can see that MI arises only if the system is bistable, on the lower-branch of the bistable cycle. More precisely MI arises only if Δ>2, which is the detuning of the intersection between the curve P_Ω and P_-.

As an example we plot in Fig. 1.6(b) the steady-state curve for a detuning $\Delta = 6.25 > 2$ that corresponds to the red dotted vertical line in Fig. 1.6(a). The black solid curves correspond to the stable states (blank area in Fig. 1.6(a)) and black dotted line between the knees labeled P_- and P_+ (green dots in Fig. 1.6(a)-(b)) to the homogeneous unstable states (gray area in Fig. 1.6(a)). The colored area stands for the domain where MI can arise. It is worth noting that in the normal dispersion region MI exist only on the lower-branch of the bistable cycle.

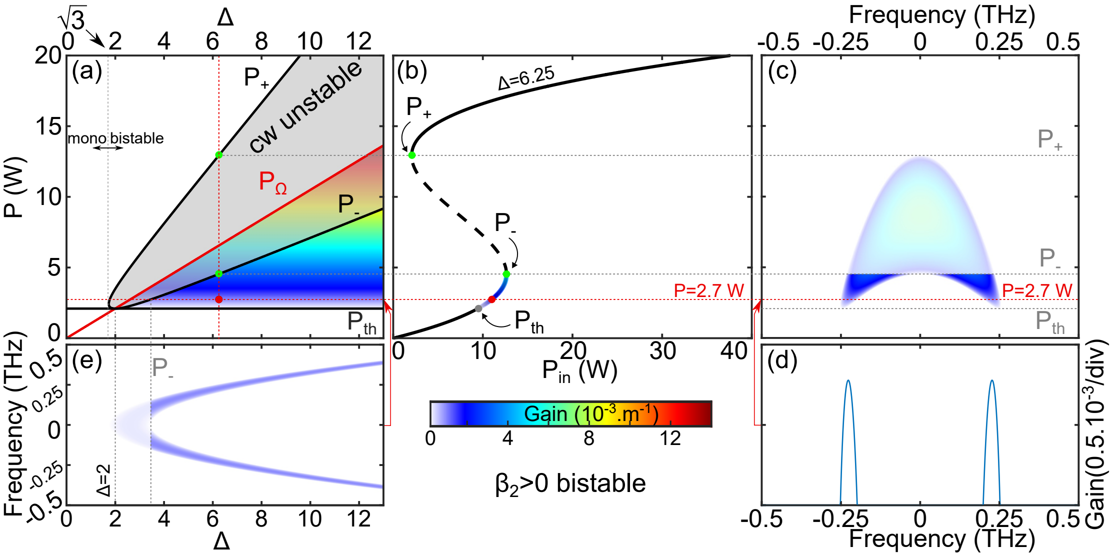

Figure 1.6: (a) 2D-map of the maximum gain in the plane (Δ, P). (b) and (c) are respectively the steady-state curve and the 2D map of MI gain in the plane (Frequency, P) for $\delta_0 = \pi/4$ rad (red vertical line (a)). Colored part of bistable cycle stands for MI regimes. (d) Gain spectrum for $\delta_0 = \pi/4$ rad, $P_{in} = 11$ W (red dot (a), (b)). (e) Gain 2D-map in the plane (Δ, Frequency) for $P = 2.7$ W. Parameters: $\gamma = 1.2\ .\mathrm{W}^{-1}.\mathrm{m}^{-1}$, $L = 50$ m, $\beta_2 = 9$ ps^2.m^{-1}, $\theta = \sqrt{0.1}$, $\kappa e^{-\alpha_f L/2} \approx 0.92$ ($\mathcal{F} \approx 25$).

Fig. 1.6(c) shows for $\Delta = 6.25$ (red dotted vertical line in Fig. 1.6(a)) the evolution of the gain spectrum calculated from Eq. (1.23) versus P as a 2D-color plot. It displays two thin and weak symmetrical sidebands arising above the MI cavity threshold P_{th}. The gain of these bands increases slowly and their frequencies shift toward the central frequency with increasing intra-cavity power. Above the gray dotted line (labeled P_-) that corresponds to the lower knee of the bistable cycle, MI no longer exists since it corresponds to homogeneous unstable states. In Fig. 1.6(d) we give as an example the gain spectrum calculated for the peculiar values $P = 2.7$ W, $\Delta = 6.25$ that corresponds to the red horizontal dotted line in Fig. 1.6(b) (red dots in Fig. 1.6(a)-(b)).

Finally in Fig. 1.6(e) we show for $P = 2.7$ W above the cavity threshold (red horizontal dotted line in Fig. 1.6(a)) the evolution of the gain spectrum calculated from Eq. (1.23) versus Δ as a 2D-color plot. The left gray vertical dotted line stands for the threshold $\Delta = 2$ below which MI does not exist, the right one corresponds to the detuning threshold above which the system becomes modulationally unstable. Above this value of the detuning, we observe two sidebands that shift away from the central frequency and become thinner when the detuning increases.

1.4.2.2 Anomalous dispersion regime ($\beta_2 < 0$)

In the case of anomalous dispersion regime ($\beta_2 < 0$), MI arises if:

$$\boxed{\beta_2 < 0,\ P > P_{th} = \frac{\alpha}{\gamma L} \text{ and } P > P_\Omega = \frac{\delta_0}{2\gamma L}} \tag{1.26}$$

where P_{th} is the MI cavity threshold imposed from $g(\Omega_T)$=0 and P_Ω is the threshold below which the solutions Ω_T are no longer real. We gave an overview of the MI arising conditions following the same representation than Fig. 1.6 in Fig.1.7(a). We note that, contrary to the previous case, that MI can arise whatever the detuning. Moreover, two cases can be identified: (i) the monostable regime and (ii) the bistable regime. These two cases are illustrated in Fig. 1.7 and in Fig. 1.8, respectively.

Monostable regime

In the monostable regime in Fig. 1.7(a), the system becomes modulationally unstable above P_{th}. We highlighted this in the steady-state curve obtained for $\Delta = 0.8 < \sqrt{3}$ (red vertical line in Fig. 1.7(a)) in Fig. 1.7(b) by a transition from a black curve to colored curve. We show in Fig. 1.7(c) the evolution of the gain spectrum calculated from Eq. (1.23) versus P as a 2D-color plot. It displays two weak sidebands at the MI cavity threshold of increasing amplitudes shifting away from the central frequency. An example of a gain spectrum is shown in Fig. 1.7(d) that corresponds to the red dot configuration in Fig. 1.7(a)-(b) and red dotted line in Fig. 1.7(c) ($\Delta = 0.8$, $P = 5.9$ W). Finally, we show in Fig. 1.7(e) the evolution of the gain spectrum calculated from Eq. (1.23) versus Δ as a 2D-color plot for $P = 5.9$ W (red horizontal line in Fig. 1.7(a)). It displays two sidebands shifting toward the central frequency until the threshold labeled P_+. Above it, the homogeneous states are unstable.

Bistable regime

In the bistable regime in Fig. 1.8(a), the system becomes modulationally unstable above P_+ on the upper-branch of the bistable cycle. We highlighted this in the steady-state curve obtained for $\Delta = 5.7 > \sqrt{3}$ (blue vertical line in Fig. 1.8(a)) in Fig. 1.8(b) by a transition from black solid and dashed curves corresponding to homogeneous stable and unstable states, respectively, to colored curve. We show

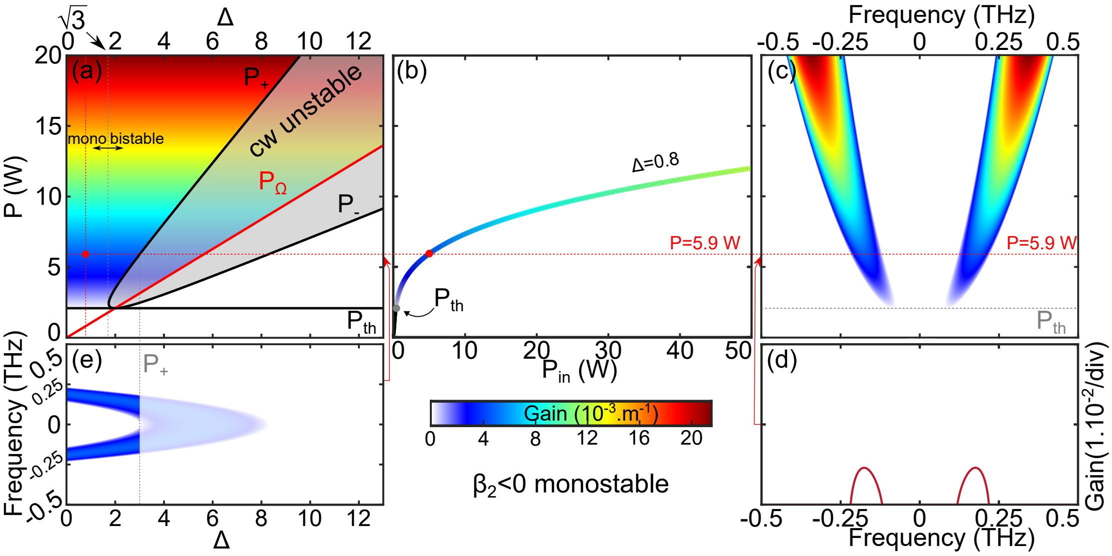

Figure 1.7: (a) 2D-map of the maximum gain in the plane (Δ, P). (b) Steady-states curve (red vertical line (a)) and (c) the gain spectrum versus P for $\Delta = 0.8$. Colored part of the bistable cycle stands for MI regimes, and the black curve for homogeneous stable states. (e) Gain spectrum for $\Delta = 0.8$ and $P = 5.9$ W (red dot (a), (b)). (e) Gain spectrum versus Δ for $P = 5.9$ W. Parameters: $\beta_2 = -20$ ps^2.km^{-1}, and see caption's Fig. 1.6.

in Fig. 1.7(c) the evolution of the gain spectrum calculated from Eq. (1.23) versus P as a 2D-color plot. It displays two sidebands at the threshold labeled P_+ of increasing amplitudes shifting away from the central frequency. Below this threshold, the homogeneous states are unstable. An example of a gain spectrum is shown in Fig. 1.7(d), it corresponds to the blue dot configuration in Fig. 1.7(a)-(b) and blue dotted line in Fig. 1.8(c) ($\Delta = 5.7$, $P = 15.5$ W). Finally, we show in Fig. 1.8(e) the evolution of the gain spectrum calculated from Eq. (1.23) versus Δ as a 2D-color plot for $P = 15.5$ W (blue horizontal line in Fig. 1.8(a)). It displays two sidebands shifting toward the central frequency until the threshold labeled P_+. Above it, the homogeneous states are unstable.

To summarize, we identified two MI cases depending on the dispersion sign. In the normal dispersion regime, MI exists only if $\Delta > 2$ on the lower-branch of the bistable cavity response. In the anomalous dispersion regime, MI exists whatever the detuning. In the monostable regime, MI arises when P is above the cavity threshold P_{th}. In the bistable regime, MI arises only on the upper-branch of the bistable cycle. We emphasize that contrary to MI in single pass in monomode isotropic fiber, where the process is observed only in anomalous dispersion region, in passive fiber cavities, this process is extended to normal dispersion region [51,86,87] thanks to the contribution of the cavity detuning.

These figures have been obtained from a linear stability analysis of the LLE that provides the gain spectrum and the conditions under which MI arises with respect

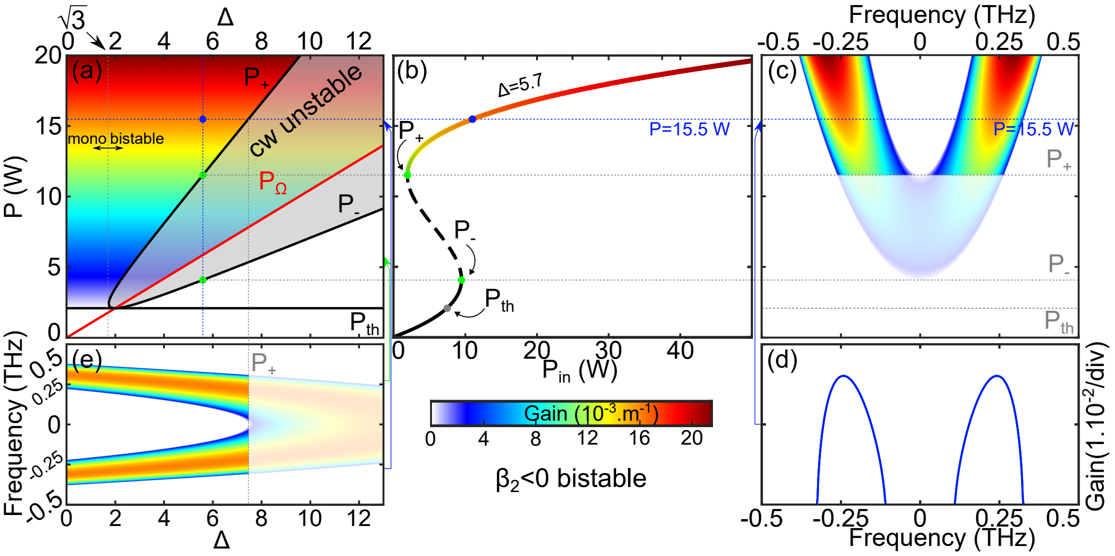

Figure 1.8: (a) 2D-map of the maximum gain in the plane (Δ, P). (b) Steady-states curve (red vertical line (a)) and (c) the gain spectrum versus P for $\Delta = 5.7$. Colored part of the bistable cycle stands for MI regimes, and the black curve for homogeneous stable states. (e) Gain spectrum for $\Delta = 0.8$ and $P = 5.9$ W (red dot (a), (b)). (g)-(h) Gain spectrum versus Δ for $P = 15.5$ W. Parameters: $\beta_2 = -20$ ps^2.km^{-1}, and see caption's Fig. 1.6.

to small perturbations. However, this analysis does not provide any information on the dynamics of large amplitude modulated states. In the normal dispersion regime, it has been demonstrated from the original study about such instabilities by Lugiato and Lefever [82] that the system bifurcates *subcritically* for $\Delta > 41/30$. Consequently, the system bifurcates from the steady-state branch to a MI branch above the MI cavity threshold ($P_{th} = \alpha/(\gamma L)$). This means that the amplitude of MI pattern is of the order of the homogeneous solution, even close to the vicinity of the MI threshold P_{th}. Therefore, the linear stability of the LLE does not provide an accurate description of the cavity dynamics. To overcome this limitation it has been suggested by Coen *et al.* [53] to describe the system by means of a truncated Fourier mode expansion of the field [92], by taking into account both the homogeneous mode ($\Omega = 0$) and modulated mode ($\pm\Omega_T$). This analysis allows to calculate from a numerical approach the new branch and its stability around the critical point P_{th}. The main result of this study is that the system can experience MI stable patterns only if $\Delta > 4.25$. To illustrate this study, we depicted this bifurcation for three different values of the detuning in Fig. 1.9 in the case of bistable regimes. From left to right, the three bifurcations correspond to $\Delta = 4.0$, 4.25, 4.5 respectively. Black solid curves and black dashed curves stand for the stable and unstable homogeneous, respectively. Red solid curves correspond to the stable portion of MI branch and red dashed curves to its unstable states. We note that the MI branch connects the MI threshold labeled A on the lower-branch to the negative slope of the bistable cycle at the point B. For $\Delta < 4.25$, illustrated in Fig. 1.9 by the bifurcation on the left

($\Delta = 4.0$), the stable portion of MI appears below the input power of the bifurcation points A. This means that by increasing the input power above the bifurcation point A, the system switches to the upper-branch of the bistable cycle, which is the only stable state for this range of input powers. By increasing the detuning, the range of input powers where the MI is stable increases and for $\Delta \geq 4.25$ (see Fig. 1.9 middle and right bifurcations) this MI branch becomes accessible. This study shows that in normal dispersion region, MI can be observed on a more constrained range of detunings compared to the linear stability analysis that predicted MI on the lower-branch since $\Delta > 2$ (see section 1.4.2.1).

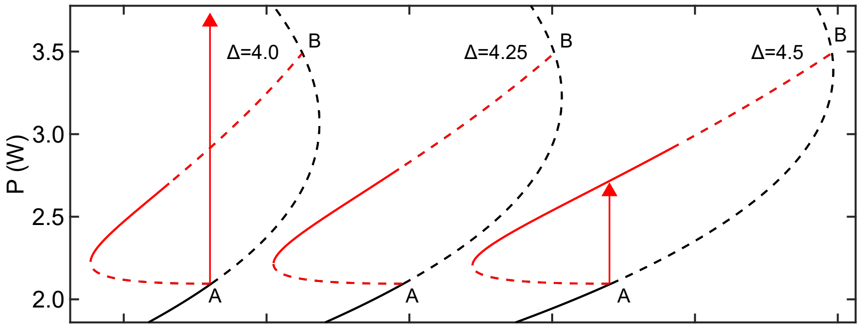

Figure 1.9: Bifurcation diagrams for three different values of Δ. From left to right $\Delta = 4.0$, 4.25, and 4.5, respectively. Homogeneous stable (unstable) states are depicted with black solid (dashed) lines and MI stable (unstable) states with red solid (dashed).

1.5 Experimental setup

In this section, we describe the experimental setup build by Fançois Copie during his PhD thesis [93]. It allows to introduce and clearly identify the different parts required to experimentally investigate MI in passive fiber cavities. This setup is depicted in Fig. 1.10 where we identify three main lines: (i) the driving line (blue fibers), (ii) the line to control and measure the cavity detuning (red fibers and cables), and (iii) the detection line (green fibers and cables). These different lines are described in the following sections.

1.5.1 Driving system

We start by describing the part of the system which allows to generate the pump (identified by blue fibers). The driving field is a train of square pulses of

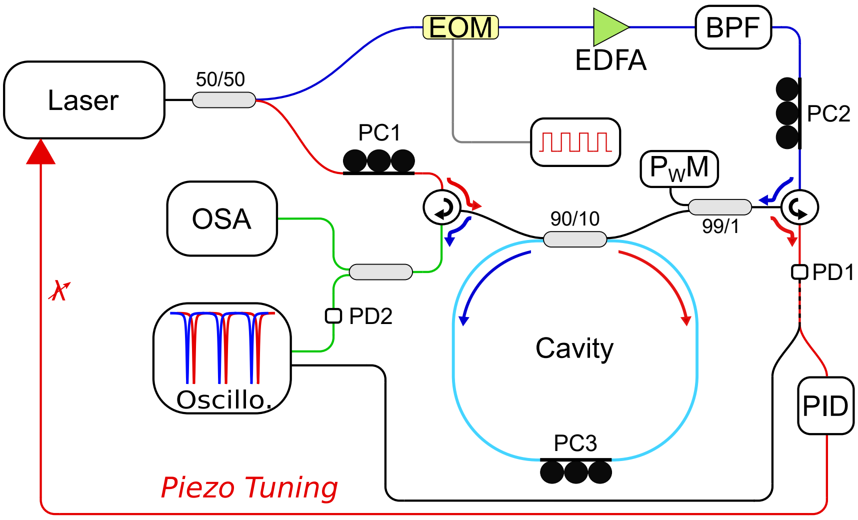

Figure 1.10: Experimental setup. EOM, electro-optical modulator; PC_{1-3}, polarization controller; PD_{1-2}, photodetector; OSA, optical spectrum analyzer; EDFA, erbium-doped fiber amplifier; BPF, band-pass filter; Oscillo., oscilloscope; PID, proportional-integrate-derivative controller; $P_W M$, powermeter.

$\approx$ 1 ns duration. It allows to prevent Stimulated Brillouin scattering[1] and to get high peak power to trig the MI process. These pulses are generated from a cw laser with a thin spectral bandwidth (less than 100 Hz) chopped by an electro-optic modulator (EOM) to generate a train of square nanosecond pulses. The repetition rate, thanks to an arbitrary waveform generator driving the EOM, is set to match with the repetition rate of the cavity, in order to drive synchronously the cavity and get one pulse per round-trip. These pulses are then amplified through an erbium-doped fiber amplifier (EDFA) and filtered through a thin filter (BPF, 100 GHz) to remove amplified spontaneous emission (ASE) in excess. Finally, these pump pulses are injected into the cavity through the right port of the cavity and propagate in the anti-clockwise direction (blue arrow in Fig. 1.10). Note that we added a 99/1 coupler just before the input port of the cavity in order to measure the power of the input pulses thanks to a powermeter ($P_W M$).

---

[1] Stimulated Brillouin Scattering (SBS) is a nonlinear process resulting from the interaction between the pump, a Stokes field and an acoustic wave to generate new waves. From the momentum and energy conservation this phenomenon has a strong angular dependence and it maximum efficiency is obtained for backward scattering. The generation of this backward wave (whose the frequency shift from the pump $f_{SBS} = 2nv/\lambda_0$ (v: sound velocity) is around 10 GHz in silica fiber at $\lambda_0 = 1550$ nm [94]) and depletes the pump power. To prevent this, different methods can be used among which adding an isolator to stop the backward waves but with the disadvantage of decreasing the cavity finesse due to its insertion loss. The other method we implemented in our setup consists to use pulses shorter than the lifetime of an acoustic phonon ($\approx$ 11 ns for silica [94]) where the threshold of SBS becomes significant is raised to high power.

1.5.2 Cavity detuning control and measure

1.5.2.1 Stabilization and control of the detuning

The second line, identified by red fibers and cables in Fig. 1.10, allows to stabilize the accumulated linear phase $\phi_0 = 2\pi cnL/\lambda_0$ seen by the pump which is essential owing to the interferometric nature of the system. Indeed, this parameter is really sensitive to external perturbations such as the change in the pressure (with the external sound) or even the change in the temperature, leading to a phase sensitivity of $-2.2 \times 10^{-5}\pi$/Pa/m and $-26 \times 10^{-5}\pi$/°C/m, respectively [95]. For our investigations, we want that this linear phase (and consequently the detuning) remains constant during the experiments. The solution is to use a feedback loop system to finely tune in real-time either the cavity length L as originally investigated by Coen *et al.* [52] or the laser wavelength λ_0 [93,96], to ensure that the linear phase remains constant. For this purpose, two circulators at each output of the cavity are implemented, which allow to use independently the two propagation directions of the cavity. While the pump propagates in the anti-clockwise direction, a fraction of the cw laser field (low power, linear regime) propagates in the clockwise direction and undergoes the same perturbations as the pump. This field is then detected at the cavity output by a photodetector (PD1) and a PID (proportional-integrate-derivative) controller, providing an error signal between the current level of this reference field and a setpoint value. The PID controller drives the integrated laser piezoelectric module (PZT) and minimize the error signal by finely tuning the pump wavelength. Its bandwidth of 16 kHz allows a sufficiently fast response of the loop to compensate for the linear phase variations induced by the external perturbation frequencies. We emphasize that the pump beam and reference beams are provided by the same laser, which means that there is no drift of the linear phase between the two fields. Consequently, when the linear phase seen by the reference field is locked, the one seen by the pump is also locked.

1.5.2.2 Measure of the detuning

The experimental cavity transfer function $P_{out} = f(\phi_0)$ (see Fig. 1.2(b)) of the two fields (pump and reference fields) can be obtained by recording the evolution of the cavity output powers by executing a linear phase scan. This scan is performed by applying a linear variation of the laser PZT module voltage. Indeed, it is proportional to the change in pump wavelength, and we checked that it induces a linear variation of the linear phase ϕ_0. Consequently, thanks to a photodetector at each output of the cavity (PD1 and PD2 in Fig. 1.10) and an oscilloscope, by scanning the cavity, we recorded and observed a set of equally spaced resonances. An example of this transfer function is depicted by the red curve in Fig. 1.11(a), where we normalized the detected power to its maximum value. The gray triangle function corresponds to the normalized voltage applied to the laser PZT module.

Note that for decreasing (increasing) voltage, the pump wavelength decreases (increases) but the linear phase increases (decreases) since $\phi_0 \propto 1/\lambda_0$. We point out that for non-PM fibers (that is the case in our work), fibers exhibits random residual and stress-induced birefringence providing two orthogonal polarization eigenstates. Since the refractive index is not the same on both states, each of them provides a different set of resonances. As an example, we plot in Fig. 1.11(a) with the red and blue curves standing for the two sets of resonances, one corresponding to the slow mode and the other to the fast mode. Note that if the input field does not match one of the polarization mode, we observe an overlapping between the two sets of cavity resonances. For our experiments, we added two polarization controllers (PC1 on red line and PC2 on blue line in Fig. 1.10), which allow to propagate the pump beam on one polarization mode and the reference field on the other. Such configuration has two main benefits: (i) it minimizes the interaction between the pump and reference beams inside the cavity (cross-phase modulation [75]) and (ii) it provides a continuous tuning of the detuning as we will explain below.

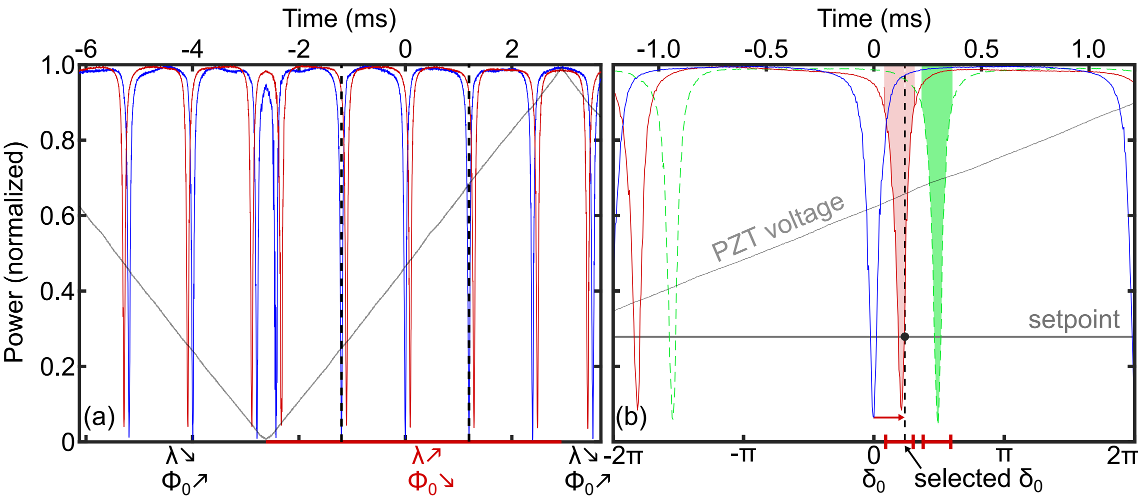

Figure 1.11: (a) Cavity complementary transmission functions. Blue and red curves stand for the pump and reference response functions, respectively. Gray curve: triangular tension applied on laser integrated PZT. (b) Zoom on red delimited part in (a). Horizontal gray line: setpoint tension; black dot: draw tension setpoint, red parts: available detuning range from their respective transmission function.

Finally, we can measure the detuning by recording consecutive resonances from both field in the linear regime. As an example, we show in Fig. 1.11(b) the sets of resonances from the reference and pump beams with the solid red and solid blue curves, respectively. Note that we directly scaled the x-axis with respect to the detuning ($\phi_0 = -\delta_0 + 2k\pi$, k integer) by taking the low extremity of a pump resonances as a reference and by noting that the space between two resonances corresponds to 2π. The chosen setpoint value fixed by the PID controller corresponds to the gray line, consequently the detuning corresponds to the abscissa of the crossing between setpoint curve and the reference beam resonances. In the depicted example in Fig. 1.11(b), we chose to stabilize the cavity on the black crossing point (on the positive slope of the reference beam resonance) corresponding to the detuning marked by the black dashed line. Obviously, it can be chosen to stabilize the cavity on the other crossing point (negative slope of the reference beam resonance). We point out that the cavity can be stabilized only on a limited range of detunings that corresponds approximately to the width of the resonance (see red area in Fig. 1.11(b)). Indeed, beyond the wings of the resonance, a small derivation from the setpoint induces a large variation of the detuning. To overcome this limitation, we incorporate a polarization controller (PC3) inside the cavity [51, 52, 97]. It induces a controllable additional birefringence and modified the optical path between the polarization states. This allows to play between the spaces between the two sets of resonances, and achieve any value of the detuning. As an example, we plot in Fig. 1.11(b) a new set of resonances. The blue curve stands for the resonances of the pump field and green dashed curves for the resonances of the reference field. The new available range of detuning corresponds to the green area. In this way, we can measure the detuning with a precision estimated at 0.05 rad.

1.5.3 Detection system

The last part highlighted by green fibers and cables placed at the nonlinear beam cavity output in Fig. 1.10 stands for the detection system. In the simplest case, we use a photodetector with an oscilloscope to record the cavity response function, and/or an optical spectrum analyzer (OSA) to record the MI output cavity spectrum. Additional instruments can be added at this output to get a dynamical characteristic of the cavity either in the spectral domain, by means of dispersive Fourier transform (DFT) [98–100] or in the time domain, with a time-lens system [101–103]. This latter equipment will be described in chapter 3 where it will be used.

Summary

We first recalled the main linear effects (loss and dispersion) experienced by an optical field during its propagation along a single mode fiber. Then we introduced the nonlinear effects, more precisely the Kerr effect, which is a phenomenon where the refractive index of the material becomes proportional to the intensity of the applied field. We recalled the nonlinear Schrödinger equation that describes the field propagation in a medium with these properties.

In a second step, we presented the cavity concept and the Ikeda model ruling the field propagation along the multiple pass inside the cavity. We showed the interferometric nature of this system exhibits resonances as in Fabry-Perot systems. Moreover, we pointed out the impact of the nonlinearity on such resonances.

We then introduced the Lugiato-Lefever model, which allows to derive a simple equation from the Ikeda map model assuming that the field is not significantly modified from a round-trip to another. This equation called *Lugiato-Lefever Equation* (LLE) is really convenient as it allows to derive simple theoretical analysis to describe MI close to the cavity threshold.

Finally, we described the experimental setup, the utility of each line that composed it, and explained the necessity and the technique to control and measure the detuning based on a PID feedback loop.

Chapter 2

Modulation instability in the weak normal dispersion of fiber-ring cavities

Contents

Modulation instability in Kerr passive resonators has been widely studied during the last decades as it is known as a precursor for frequency comb generation [91] and ultrahigh repetition rate pulse trains [55]. We saw in the previous chapter that the group-velocity dispersion (GVD) plays a significant role in the mechanism of MI. Indeed, MI sideband position (see Eq. (2.1)) is inversely proportional to the square root of β_2. To date, most studies of MI in passive fiber cavities have been carried out in large normal or anomalous dispersion regions, far away from the ZDW. In these cases, expanding the propagation constant in Taylor series up to the second order dispersion term (β_2) is enough to capture the whole dynamics of the system [51, 90]. However, close to the ZDW (weak dispersion regions), the MI spectrum becomes wider (see Eq. (2.1)). Thus, high-order dispersion (HOD) terms must be considered in order to take into account the variation of the propagation constant over the whole spectrum and capture the MI dynamics. On the one hand, it has been shown theoretically and experimentally that in passive cavities, the third order dispersion (TOD) term: (i) was responsible for convective MI in weak dispersion regions [104, 105] characterized by a spectral symmetry breaking, and (ii) for the generation of dispersive waves in the context of cavity solitons, which stabilize the underlying Kerr frequency combs [106]. One the other hand, it has been demonstrated theoretically that fourth-order dispersion (FOD) term modifies strongly the dynamics of the system: (i) it allows for new phase-matching frequencies, extends MI dynamics in normal dispersion region, as in single pass configurations [89, 107, 108], (ii) leads to the disappearance of MI when the pump exceeds a certain threshold [109], and more surprisingly, (iii) to the generation of tens of quasi-phase-matched MI sidebands in dispersion oscillating passive fiber cavities. Note that recent investigations showed that TOD and FOD were also responsible for the generation of widely tunable parametric oscillation [58, 110] (octave-spanning), particularly appealing for spectroscopy, and *"clustered"* OFC [111] in the context of Kerr microresonators. In the following work, we present an experimental study of MI in the weak normal dispersion region of a passive fiber cavity, just above the MI cavity threshold in both monostable and bistable regimes. We show that FOD leads to significant modifications of MI features, namely the generation of new sidebands.

The chapter is organized as follows. In the first section, we recall the extended LLE that allows to study the MI dynamics in such weak dispersion regime, by taking into account HOD terms [97, 109, 112]. Then, in the second section, we briefly describe the experimental setup which is similar to the one presented in the previous chapter (see section 1.5) and we give the cavity parameters. Finally, in the last section, we show our experimental results and compare them to theoretical predictions and numerical simulations.

2.1 Theory: extended Lugiato-Lefever equation including high-order dispersion terms

In this section, we first recall the model that allows to describe the MI dynamics in the vicinity of the ZDW of optical fibers, and we give the new MI phase-matching relation. Then we study the extended MI occurrence conditions and we focus particularly on the weak normal dispersion regime, where the FOD term leads to significant modifications of MI dynamics, such as the generation of additional bands.

2.1.1 Extended LLE and phase-matching relation

As shown in chapter 1, for low power and low detuning, the light propagation and modulation instability dynamics are well modeled by the Lugiato-Lefever equation. However, in the low dispersion regime close to the vicinity of the fiber zero-dispersion wavelength, high-order dispersion terms must be considered. This leads to an extended version of the original LLE taking into account these terms such as [109]:

$$\frac{\partial E(z,\tau)}{\partial z} = \left(-\frac{\alpha}{L} - i\frac{\delta_0}{L} + i\sum_{n=2}^{n=4} i^n \frac{\beta_n}{n!}\frac{\partial^n}{\partial \tau^n} + i\gamma|E(z,\tau)|\right) E(z,\tau) + \frac{\tilde{\theta}}{L}E_{in} \tag{2.1}$$

Note that we expand the dispersion only up to β_4 since higher-order dispersion terms, in realistic passive fiber cavities, are negligible. By proceeding to a linear stability analysis in a similar way that was developed in section 1.4.1, it is straightforward to find the parametric gain:

$$g(\Omega) = -\frac{\alpha}{L} + \sqrt{\gamma^2 P^2 - \psi^4} \tag{2.2}$$

where $\psi = \sqrt{\beta_2\Omega^2/2 + \beta_4\Omega^2/24 + 2\gamma P - \delta_0/L}$. The most unstable frequencies and their respective growth rates are given by:

$$\Omega_{T\pm} = \pm\sqrt{\frac{-6\beta_2 \pm 6\sqrt{\beta_2^2 - \frac{2}{3}\beta_4\left(2\gamma P - \frac{\delta_0}{L}\right)}}{\beta_4}}, \text{ and } g\left(\Omega_{T\pm}\right) = -\frac{\alpha}{L} + \gamma P \tag{2.3}$$

As it can be seen from these expressions, MI existence conditions are modified with respect to standard MI. Note that only even dispersion terms (β_2 and β_4 in Eqs. (2.2-2.3)) affect modulation instability, in particular odd dispersion terms β_3 does not enter into play.

2.1.2 Extended MI occurrence conditions

MI exists when one or both unstable frequencies $\Omega_{T\pm}$ are real and when $g\left(\Omega_{T\pm}\right)$ is (are) positive. MI can arise in multiple configurations depending on β_2 and β_4 relative signs. In the following, we will focus on configurations where $\beta_4 < 0$, which is the case in most optical fibers. We can identify two cases depending on the dispersion sign described in the following two points.

2.1.2.1 Normal dispersion regime ($\beta_2 > 0$)

In the case of normal dispersion regimes ($\beta_2 > 0$), MI arises if:

$$\beta_2 > 0 \text{ and } \Omega_{T-} \text{ real}: \; P > P_{th}, \; P > P_{\beta_2} \tag{2.4}$$

$$\text{and } \Omega_{T+} \text{ real}: \; P > P_{th}, \; P_{\beta_2} < P < P_{\Omega} \tag{2.5}$$

where $P_{th} = \alpha/(\gamma L)$ is the MI cavity threshold imposed from $g(\Omega_{T\pm}) = 0$, $P_{\Omega} = \delta_0/\left(2\gamma L\right)$ the threshold above which the solution Ω_{T+} are complex, and $P_{\beta_2} = P_{\Omega} + \left(3\beta_2^2\right)/\left(4\beta_4\gamma\right)$ the threshold below which the solutions Ω_{T+} and Ω_{T-} are complex. The map of the maximum of the gain (calculated from Eq. (2.3)) in the $(\Delta,\, P)$

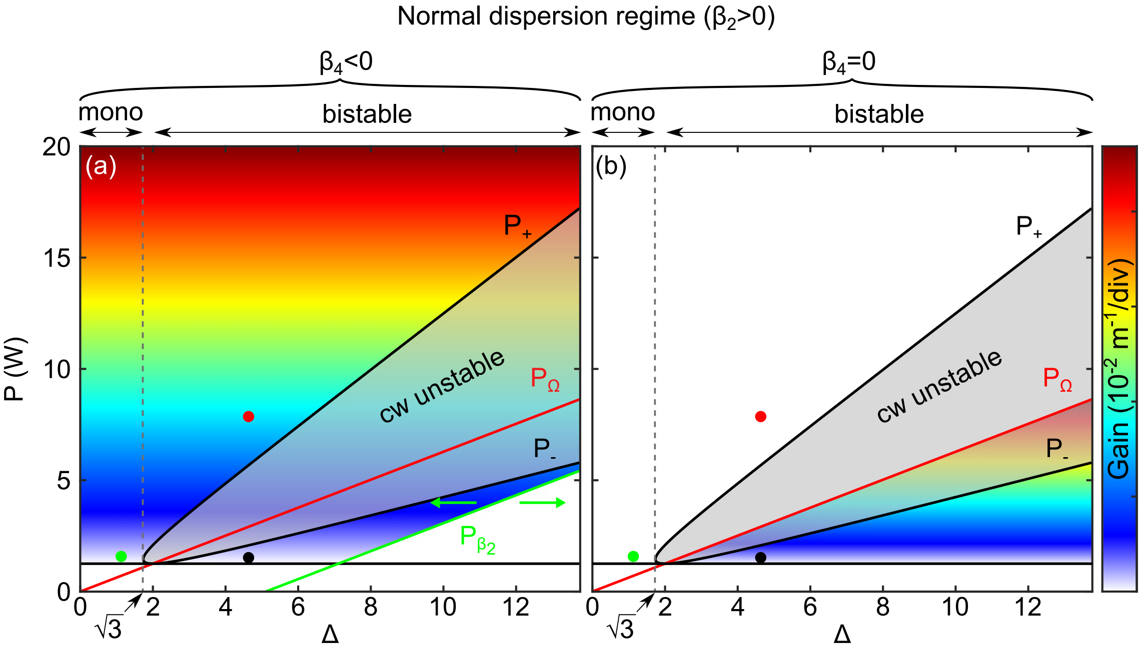

Figure 2.1: 2D-maps of the maximum gain (Eq. (2.3)) in the $(\Delta,\, P)$ plane in the case of a normal dispersion regime, (a) with β_4 and (b) without β_4. Parameters: $\beta_2 = 0.08$ ps^2.km^{-1}, $\mathcal{F} \approx 26.5$ ($\alpha = 0.118$), $L = 37.9$ m, $\theta = \sqrt{0.1}$, $\gamma = 2.5$ W^{-1}.km^{-1}, and $\beta_4 = -6 \times 10^{-4}$ ps^4.km^{-1}.

plane corresponding to $\beta_2 > 0$ and $\beta_4 < 0$ is shown in Fig. 2.1(a), by using the same representation than in chapter 1 (see Fig. 1.6(b)). To make easier the comparison between the case where $\beta_2 > 0$ and $\beta_4 < 0$ with the case where $\beta_2 > 0$ and $\beta_4 = 0$, we report the latter in Fig. 2.1(b). The black horizontal line stands for the MI cavity threshold P_{th}. The red and green lines correspond to the threshold P_Ω and P_{β_2}, respectively. The gray area labeled *"cw unstable states"* stands for the homogeneous unstable sates (negative slope branch of the bistable curve between the knees P_+ and P_-), colored area for the modulationally unstable regions and blank areas for the stable domains. [34, 53, 76]. We observe some differences between these two cases. First, for $\beta_4 = 0$ (see Fig. 2.1(b)) MI is restricted to bistable regime ($\Delta > 2$), while for $\beta_4 < 0$ the MI domain is extended to monostable regimes and to the upper-branch of bistable regimes. Second, for $\beta_4 < 0$ the MI domain on the lower-branch is restricted compared to the case where $\beta_4 = 0$ [1].

2.1.2.2 Anomalous dispersion regime ($\beta_2 < 0$)

In the case of anomalous dispersion regimes ($\beta_2 < 0$), MI arises if:

$$\beta_2 < 0 \text{ and } \Omega_{T-} \text{ real}: \; P > P_{th}, \; P > P_\Omega \tag{2.6}$$

$$\text{and } \Omega_{T+} \text{ real}: \; \text{no solution} \tag{2.7}$$

where $P_{th} = \alpha/(\gamma L)$ is the MI cavity threshold imposed from $g(\Omega_{T\pm}) > 0$, and P_Ω the threshold above which the solution Ω_{T-} is complex. Note that these conditions are identical to those of the standard MI in anomalous dispersion regimes except that the MI sidebands are located to $\pm\Omega_{T-}$ (Eq. (1.24)). In the following, we do not investigate this case since only the position of MI sidebands are affected without affecting the MI domains. We decided to focus on the normal dispersion regime ($\beta_2 > 0$) that exhibits a more complex dynamics. We point out that the specific case, where $\beta_4 > 0$ and $\beta_2 < 0$, has been studied theoretically in Ref. [109], and shows, in particular, that pairs of MI sidebands can arise at the MI cavity threshold. When the input power increases, bands widen and merge in a pair of large bands and disappear above a secondary threshold, and the system return to a stationary state.

By looking at the position of the most unstable frequencies, we see that it depends on β_2. In experiments, it is possible to change this parameter by tuning the pump wavelength[2]. Thus, by using a cavity made of fiber for which $\beta_4 < 0$, it is possible to investigate the position of the sidebands in both dispersion regimes in a single experiment. This behavior is studied in the following section.

---

[1] Note that the threshold P_{β_2} depends on β_2^2/β_4 (green lines in Fig. 2.1(a)). This dispersion term depends on the pump wavelength. This means that by changing the pump wavelength, the line labeledP_{β_2} in Fig. 2.1(a) is shifted, on the left or right side restricting or extending the MI domain on the lower branch of bistable cycle.

[2]

$$\beta_2 = \frac{S_0}{8\pi c}\left(\frac{\lambda_{ZDW}^4}{\lambda_{pump}} - \lambda_{pump}^3\right) \tag{2.8}$$

where S_0 is the zero-dispersion slope specific to the fiber used.

2.1.3 Evolution of MI bands with the pump wavelength

We investigate, in the configuration $\beta_4 < 0$, the evolution of the most unstable frequencies calculated from Eq. (2.3) for the three operating regimes of the cavity: (i) the monostable regime, (ii) the lower-branch and (iii) the upper-branch of the bistable regime. We represent this evolution across the normal dispersion ($\beta_2 > 0$) and anomalous dispersion ($\beta_2 < 0$) regions in Fig. 2.2(a)-(b)-(c), respectively. The black dashed lines stand for the standard MI case (without β_4) and the blue lines for the MI case with $\beta_4 < 0$. The red dotted lines correspond to the ZDW and the blue and red domains to anomalous and normal dispersion regions, respectively (see right y-axis in Fig. 2.2(c)). The impact of β_4 is similar in the monostable regime (Fig. 2.2(a)) and on the upper-branch of the bistable regime (Fig. 2.2(c)). In absence of FOD (black dashed lines), MI only exists in the normal dispersion region with two sidebands that shift towards infinity when moving closer to the ZDW, while with β_4, owing to its negative value, it exists a perfect phase-matching whatever the dispersion region. The MI bands with β_4 (blue curves) tend to merge with standard MI bands (without β_4) towards the long wavelengths whereas they shift to high frequency shifts toward short wavelengths in the normal dispersion region. The second category corresponds to the lower-branch of the bistable regime (Fig. 2.2(b)). In this regime, MI only exists in the normal dispersion region with and without β_4. In the case of standard MI (without β_4), two sidebands exist, which shift towards infinity while moving closer to the ZDW whereas in the case of MI with $\beta_4 < 0$, two pairs of sidebands exist simultaneously below a pump wavelength threshold ($\lambda_{pump,th}$ = 1551.1 nm, $\beta_{2,th}$ =0.046 ps^2.km^{-1}). One pair of sidebands

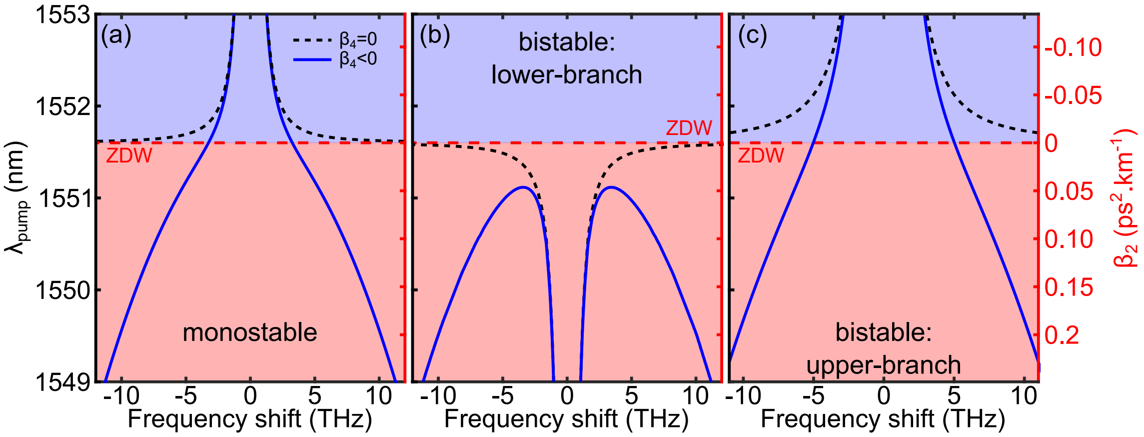

Figure 2.2: Frequency shifts calculated from Eq. (2.3) with (blue lines) and without (dashed black lines) β_4 calculated from Eq. (1.24). (a) In the monostable case for Δ = 1.1 and P = 1.58 W (green dots in Fig. 2.1, in the bistable case Δ = 4.6, (b) on the lower-branch for P = 1.83 W (black dots in Fig. 2.1), (c) on the upper-branch for P = 7.86 W (red dots in Fig. 2.1). Red (blue) part: normal (anomalous) dispersion regimes. Parameters: see caption of Fig. 2.1.

shifts toward large frequencies while the other one tends to merge with the standard MI sidebands when the pump wavelength decreases.

2.2 Experimental setup

In order to check the theoretical predictions reported in the previous section, we used the experimental setup described in the previous chapter and we implemented a cavity built with a fiber whose group-velocity is slightly normal at the pump wavelength ($\lambda_{pump} \approx 1550$ nm). The cavity consists in a dispersion shifted fiber (DSF) closed by a 90/10 coupler made of the same fiber to get a perfectly uniform cavity and avoid parametric instabilities that might arise in dispersion managed cavities [96,98]. The total cavity length is about 37.9 m corresponding to a repetition rate of 5.4 MHz. The DSF has a nonlinear coefficient of $\gamma = 2.5$ W^{-1}.km^{-1} and a zero dispersion wavelength (ZDW) at 1551.6 nm. We investigated MI in this cavity by using trains of 1.5 ns pulses whose wavelength is tunable between 1549.5 and 1550.5 nm, so that the group-velocity dispersion varies over a weak positive range, between $\beta_2 = 0.20$ and 0.11 ps^2.km^{-1}. TOD and FOD terms on this domain are $\beta_3 = 0.12$ ps^3.km^{-1} and $\beta_4 = -6.0 \times 10^{-4}$ ps^4.km^{-1}, respectively.

2.3 Experimental results

In this section, we report our experimental results by illustrating the striking contributions of β_4 in normal dispersion regimes in three cases: monostable regimes, and lower/upper-branch of bistable regimes. These results are compared to theoretical predictions and numerical simulations. In addition, we investigated the peculiar situation of bistable regimes versus the input power to capture the hysteresis cycle followed by the MI.

2.3.1 Monostable case

As a first step, we extracted from the transmission function the cavity finesse estimated to $\mathcal{F}= 26.5$, corresponding to total cavity losses of $\alpha = 0.118$. Then we set the detuning to $\delta_0 = 0.13$ rad in order to work in the monostable regime (normalized detuning is $\Delta = \delta_0/\alpha = 1.1 < \sqrt{3}$). We increased the input power until $P_{in} = 0.23$ W, just above the cavity MI threshold. This configuration is depicted by green dots in Fig. 2.1 and in Fig. 2.3(a) showing the corresponding steady-state curve. We initially set the pump wavelength to 1549.9 nm, 1.7 nm below the ZDW, where $\beta_2 = 0.16$ ps^2.km^{-1}. The output cavity spectra is depicted in Fig. 2.3(b). It exhibits two weak narrow symmetrical bands on both sides of the pump whose frequency shifts are ±9.28 THz. These results are in good agreement with the theoretical gain spectrum (Fig. 2.3(d)) calculated from Eq. (2.2), the theoretical predictions from the phase-matching equation (Eq. (2.3), bands at 9.25 THz, gray dotted vertical lines) and numerical simulations from the LLE model (Fig. 2.3(c)).

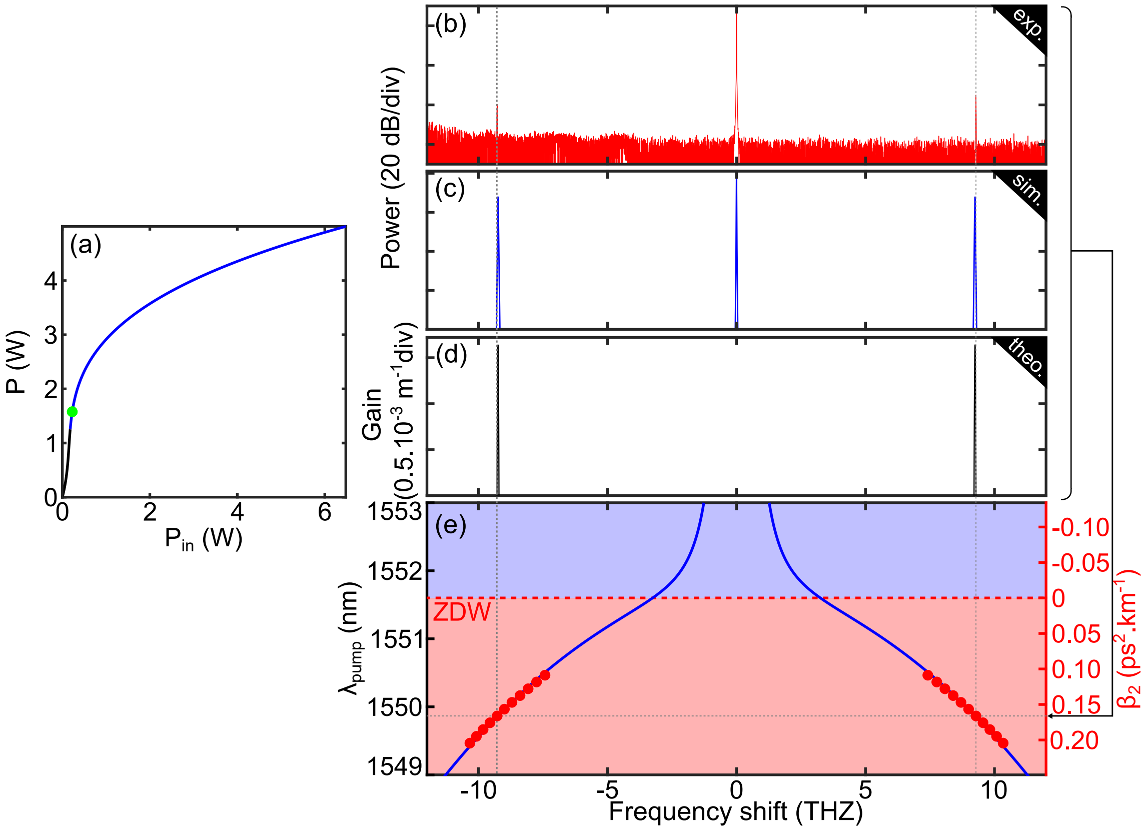

Figure 2.3: Experimental results in the monostable regime. (a) Steady-state curve, solid blue lines: modulationally unstable states, green dot: investigated setpoint. (b) Experimental output spectrum compared to (c) numerical simulations and (d) gain spectrum (Eq. (2.2)). (e) Evolution of MI sideband positions versus the pump wavelength. Solid blue lines stand for the theory (Eq. (2.3)) and red dots for experimental measurements. Parameters: $\Delta = 1.1 < \sqrt{3}$, $\lambda_{pump} = 1549.9$ nm, and $P_{in} = 0.23$ W.

To go further and validate the theoretical predictions regarding the evolution of the sideband positions versus the pump wavelength, we recorded the output spectra for a pump wavelength ranging from 1549.5 to 1550.5 nm. These experimental results are displayed in Fig. 2.3(e) by red dots. As expected, by increasing the pump wavelength leads to MI sidebands to get closer to the pump wavelength. We obtain an excellent agreement between theoretical predictions from Eq. (2.3) and experimental recordings, depicted by blue curves and red dots in Fig. 2.3(e), respectively. Experimental dots looks quasi superimposed on the theoretical curves.

2.3.2 Bistable case

In a second step, we focused on the bistable regime of the cavity by setting the detuning to $\delta_0 = 0.54$ rad. The normalized detuning is $\Delta = 4.6 > \sqrt{3}$, which is above the critical value of 4.25, where stable MI patterns arise on the lower-branch of the bistable cycle (see section 1.4.2).

2.3.2.1 Lower-branch

We first gradually increased the input power until $P_{in} = 2.69$ W just above the cavity MI threshold on the lower-branch switching on the additional branch (see the black dot on the bistable cycle in Fig.2.4(a) and in Fig. 2.1). As it can be

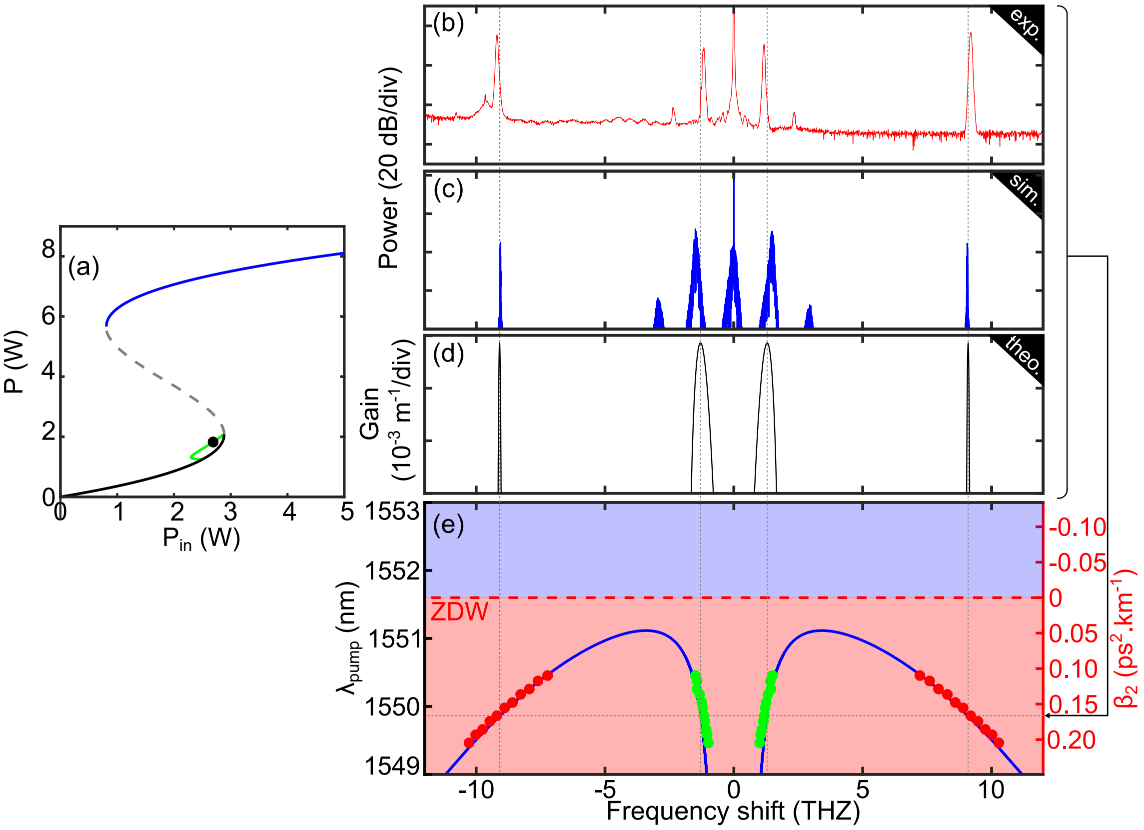

Figure 2.4: Experimental results from the lower-branch of the bistable regime. (a) Steady-state curve. Solid blue/green lines: modulationally unstable states. Black dot: investigated setpoint. (b) Experimental output cavity spectrum compared to (c) numerical simulations and (d) gain spectrum (Eq. (2.2)). (e) Evolution of MI sideband positions versus the pump wavelength. Solid blue lines stand for the theory (Eq. (2.3)) and red/green dots for experimental measurements. Parameters: $\Delta = 4.6$, $\lambda_{pump} = 1549.9$ nm, and $P_{in} = 2.69$ W.

seen from the experimental output spectrum depicted in Fig. 2.4(b), two pairs of symmetric bands can be observed. The first pair is located at ±1.18 THz, while the second pair exhibits a larger frequency shift and is located at ±9.19 THz from the pump frequency. It is noteworthy that harmonics of the first sidebands are also observed located at ±2.36 THz due to additional degenerated four-wave-mixing between the pump and the sidebands. These results match very well with theoretical predictions from Eq. (2.3) (±1.29 and ±9.09 THz) as well as the gain spectrum (Fig. 2.4(d)) and numerical simulations (Fig. 2.4(c)) from the LLE model. Particularly, we note that numerical simulations exhibit the birth of harmonics from the first pair of sidebands, as in experiments. In addition, the two new pairs of bands reach quite similar amplitudes both in experiments and in numerical simulations. That confirms the theoretical predictions from Eq. (2.2) (see Fig. 2.4(d)), where each band experience the same gain.

Then, as previously, we investigated the evolution of MI sideband positions versus the pump wavelength, whose results are displayed in Fig. 2.4(e). Green dots and reds dots stand for the position of the first and second pair of MI bands, respectively. As expected from theory (blue solid lines), by getting closer to the ZDW the frequency shifts of the first pair of sidebands increases while it decreases for the second pair. These bands seem to converge towards each other and should merge from theoretical predictions for a specific (β_2, λ_{pump}) threshold, above which we do not expect to observe MI. This feature originates directly from the contribution of β_4 as we saw in section 2.1.2 from the gain mapping in the plane (Δ, P) in Fig. 2.1. Indeed, the MI states on the lower-branch can be extended (reduced) to high (low) detuning by decreasing (increasing) the pump wavelength. The transition corresponds to the case where the curve P_{β_2} crosses the investigated point (black dot) in Fig. 2.1(a). We found that this transition appears for $\lambda_{pump} = 1551.1$ nm ($\beta_2 =$0.046 ps^2.km^{-1}). Unfortunately, we were not able to record this transition due to the limited tunable laser wavelength range preventing us to reach this specific regime.

2.3.2.2 Upper-branch

We then studied the upper-branch of the bistable regime by increasing the input power until $P_{in} = 4.09$ W (see red dots on steady-states curve in Fig. 2.5(a) and in Fig. 2.1) to switch the system from the lower to the upper-branch, which is well above the MI cavity threshold. Experimental results are reported in Fig. 2.5. We can see from the experimental output cavity spectrum in Fig. 2.5(b) that two broad asymmetric lobes with large frequency shifts are generated on both sides of the pump at ±9.35 THz (±9.56 THz from theoretical predictions, see gray dotted vertical lines and gain spectrum in Fig. 2.5(d)). This feature is in good agreement with numerical simulations (c), which reproduce also the spectral asymmetry. We checked numerically that it originates from the contribution of TOD term, which induces a nonlinear symmetry breaking of the MI process in fiber cavities [105]. The evolution of MI sideband positions versus the pump wavelength is depicted in Fig. 2.5(e) and shows a similar behavior to the monostable case. We observe that by increasing the pump wavelength, the sidebands gets closer to the pump, in excellent agreement with theoretical predictions (blue in Fig. 2.5(e) from Eq. (2.3)).

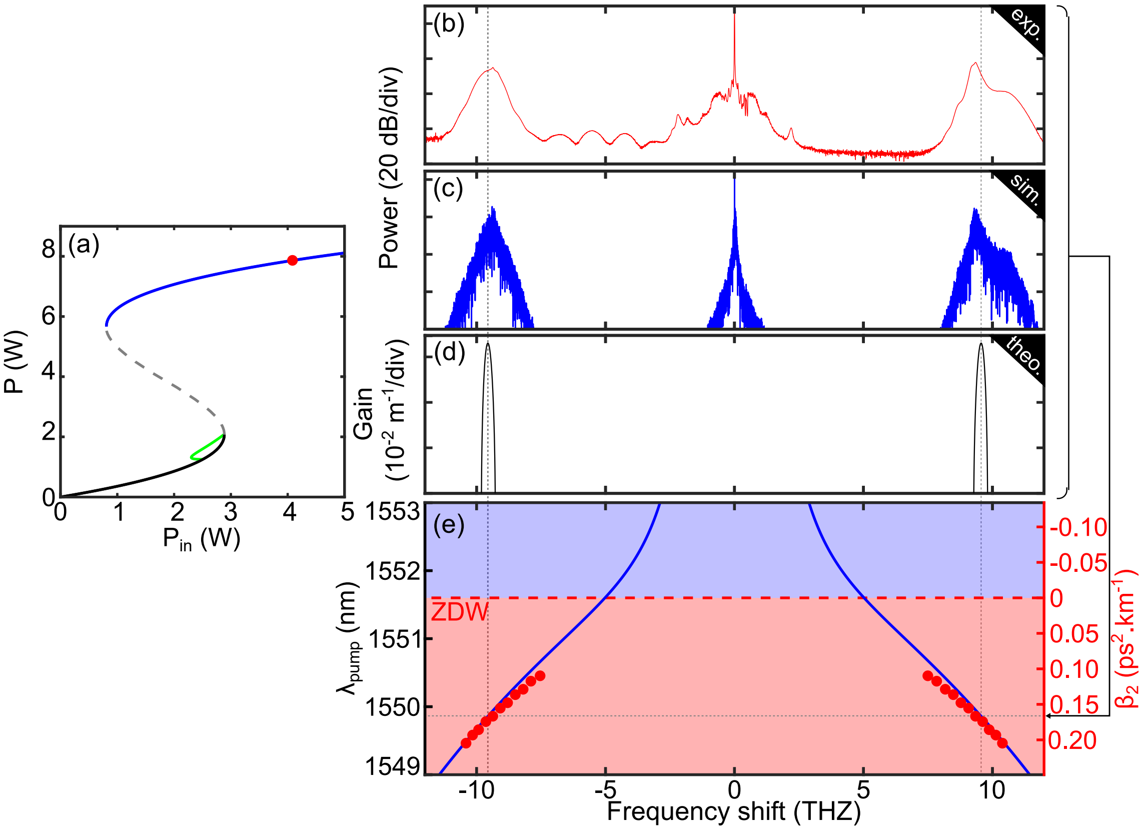

Figure 2.5: Experimental results from the upper-branch of the bistable regime. (a) Steady-state curve, solid blue/green lines: modulationally unstable states, red dot: investigated setpoint. (b) Experimental output cavity spectrum compared to (c) numerical simulations and (d) theoretical gain spectrum (Eq. (2.2)). (e) Evolution of MI sideband positions versus the pump wavelength. Solid blue lines stand for the theory (Eq. (2.3)) and red dots for experimental measurements. Parameters: $\Delta = 4.6$, $\lambda_{pump} = 1549.9$ nm, and $P_{in} = 4.09$ W.

2.3.2.3 Hysteresis cycle

In order to get a deeper insight of this process, we analyzed the transition from the lower-branch to the upper-branch of the bistable response of the cavity and *vice versa*. This has been performed by gradually increasing/decreasing the input power while recording the output cavity spectra. We set the pump wavelength at $\lambda_{pump} = 1549.7$ nm and the cavity detuning to $\delta_0 = 0.65$ rad such as the normalized

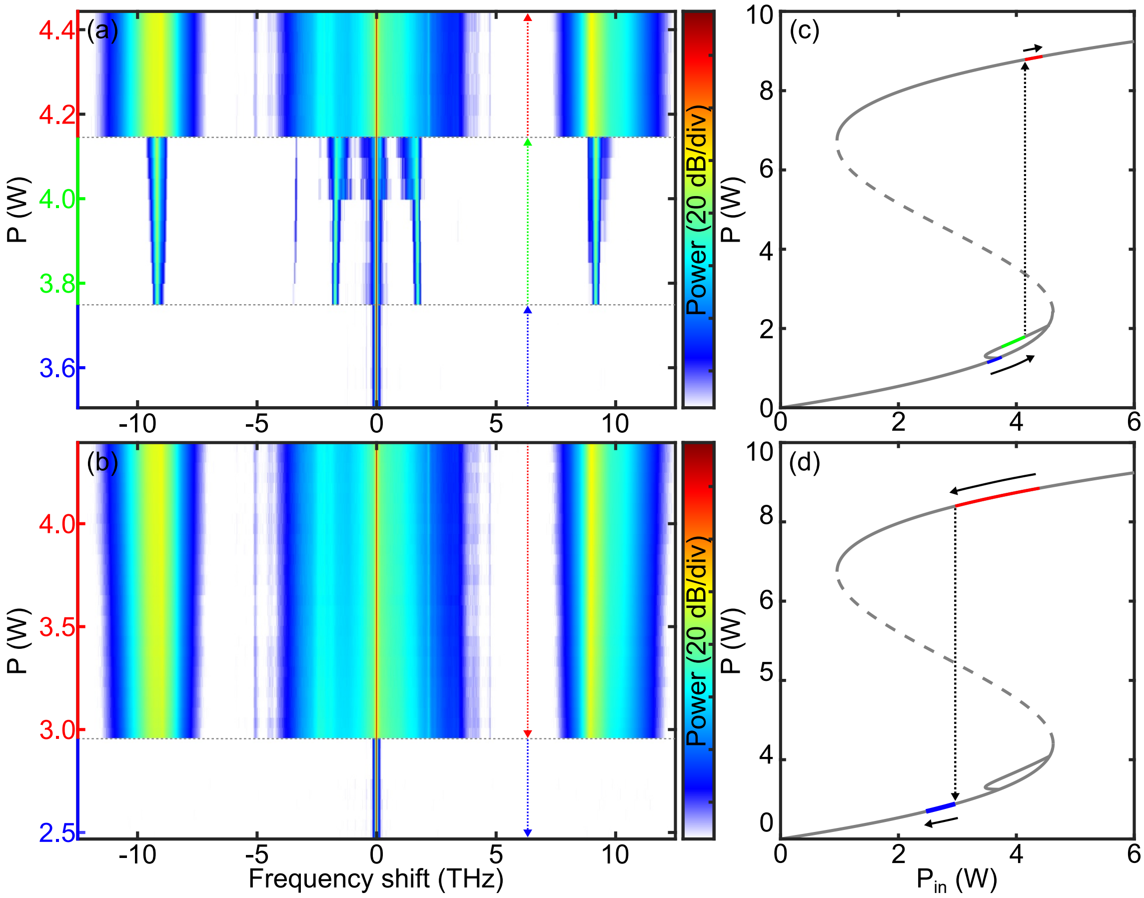

Figure 2.6: 2D-map of experimental output cavity spectrum versus the input power in the bistable regime. (a) For increasing power from the lower-branch to the upper. (b) For decreasing power from the upper-branch to the lower. (c)-(d) Steady-states curve showing the increasing and decreasing power cases, respectively, where colored part corresponds to domain investigated on 2D-map in (a)-(b), receptively and highlighted by colored arrows and Y-axes. Parameters: $\Delta = 5.5$, $\lambda_{pump} = 1549.7$ nm.

detuning is set to $\Delta = 5.5 > 4.25$, allowing to observe MI on the lower-branch. Fig. 2.5(a)-(b) shows our experimental results in a 2D-color plot of the evolution of output spectra versus the input pump power from respectively lower/upper to upper/lower branch. We can see that for an input power below $P_{in} = 3.75$ W (blue line on steady-states curve in Fig. 2.6(c) and blue arrow in Fig. 2.6(a)), that the cavity is stable and we do not observe MI bands. Then, from this threshold and up to $P_{in} = 4.15$ W (green curve in Fig. 2.6(c)), two pairs of MI sidebands arise on the lower-branch (green arrow in Fig. 2.6(a)). Above this threshold, the system abruptly up-switches on the upper-branch (red curve in Fig. 2.6(c)), where the bands with the smaller frequency shifts disappear, while the bands with highest one broadens and slightly shift away from the pump frequency (red arrow in Fig. 2.6(a)). Then we decreased the input power such as the system remains on the upper-branch until down-switching (red line on steady-states curve in Fig. 2.6(d) and red arrow in Fig. 2.6(b)). This transition appears for $P_{in} = 2.96$ W, below the MI cavity threshold where the cavity is stable on the lower-branch (blue curve in Fig. 2.6(d), blue arrow in Fig. 2.6(b)) and highlight in particular the hysteresis cycle of the cavity for such high detuning.

Summary

We showed that it is necessary to consider HOD terms when the pump wavelength is close to the ZDW of the fiber to accurately describe the full dynamics of MI. The position of MI sidebands has been predicted by a linear stability analysis from the extended LLE model developed in Ref. [97, 109]. Many configurations can be studied, however, we focused on passive fiber cavities for which the FOD term is negative corresponding to the most common case. In particular, we showed that β_4 is responsible for extending the MI process to normal dispersion regimes: (i) in monostable regimes and (ii) on the upper-branch of bistable regimes compared to the basic configuration for which $\beta_4 = 0$. Moreover, we saw that for bistable regimes where $\Delta > 4.25$, allowing MI to arise on lower-branch, two pairs of sidebands are predicted above a certain pump wavelength threshold. We checked experimentally this behavior in a passive cavity made of a DSF, by pumping the system just above the ZDW in the normal dispersion regime. We obtained a really good agreement with theoretical predictions and numerical simulations. Furthermore, we also investigated experimentally the transition from the lower to the upper branch of bistable cycle and *vice-versa*. We recorded the cavity output spectrum for increasing/decreasing input power, pointing out the hysteresis cycle of the system. Our investigations led in this chapter focus on the impact of the FOD term in the context of MI just above the cavity threshold, but we expect that FOD term should also impact a wide range of higher order nonlinear effects such as cavity solitons and frequency comb generation as it was recently shown in Ref [111].

Chapter 3

Experimental observation of modulation instability period-doubling in cavities

Contents

Recent investigations of MI have been conducted in passive resonators, in the weak dispersion region [113–115] (see chapter 2), under strong cavity driving regimes to reach nonlinear shifts larger than 2π [58, 84, 85, 116], through polarization effects [117, 118], or even in dispersion oscillating cavities [96, 97, 119, 120]. The common thread between these studies is that new parametric resonances are excited [58, 85, 96, 97, 113–117, 119–122] compared to the original studies of MI in cavities [51, 90]. The striking feature is not limited to the generation of new modulationally unstable frequencies but modifies also the behavior of the system. Indeed, from a theoretical point of view, these parametric resonances correspond to new eigenvalues of the system. These one can be positive or negative, leading to a temporal shift of the output pattern round-trip to round-trip [116, 120, 123, 124]. In the context of MI [82, 125], the periodic temporal pattern from the cavity output can be out-of-phase from round-trip to round-trip, which is denoted as P2 regime or, conversely, in phase in the so-called P1 regime [120]. In particular, the P2 regime is inherently associated to the parametric resonance that can originates from different sources such as the intrinsic periodicity of the boundary conditions [51, 52, 126–128] in uniform cavities, or modulation of one of the cavity parameters (e.g. dispersion [96, 98, 119, 120], nonlinearity [122], etc.). To our knowledge, the evidence of such P1 and P2 MI regimes has been obtained only from indirect methods, through the observation of the cavity output spectrum, where both regimes can be identified from their sidebands frequency and/or spectral dynamics (see Ref. [52] for uniform cavities and Refs. [96, 98] for dispersion oscillating cavities). The true assessment of P1 and P2 regimes requires the direct temporal observation, which is extremely challenging and has never been reported so far. The general importance of the P2 regime characterization is that it is a well known mechanism in nonlinear bistable system. P2 regime has been first predicted by Ikeda *et al.* [39] and identified has the first step on the route to chaos. It has been first observed indirectly in passive fiber cavities [50, 90, 129], then in active lasers [130–134]. In this chapter, we investigate experimentally the P1 and P2 regimes in the temporal domain of passive uniform cavities. Such characterization remains extremely challenging, since standard techniques to record the temporal domain does not provides at the same time: (i) a high resolution to identify the MI periodic pattern that lies in the picosecond scale and (ii) a round-trip to round-trip measurement. In order to satisfy both conditions, we implemented in our setup a time-lens [102], a recent instrument based on the space-time duality [101]. It allows to stretch in the temporal domain the signal to analyze and then detect it with a fast photodiode and a broadband oscilloscope [135–137]. Thus, temporal shift experienced by the output pattern round-trip to round-trip can be observed, and the nature of the MI regime identified.

In this chapter, we recall in the first section the analysis of Ikeda map model that predicts the parametric gain and P1 and P2 domains in uniform cavities. In the next section we detail the different modifications brought to the setup to both implement the time-lens system and improved the stabilization system. Finally, in the last section, we report the direct observation in the time domain of P1 and P2 regimes that we compare to numerical simulations and theoretical predictions.

3.1 Theory: Ikeda Map model

3.1.1 Linear stability analysis

The dynamics of the system can be analyzed by applying a Floquet analysis [138] on the full Ikeda map system (Eqs. (1.8-1.9)) as detailed in Ref. [120] and in Appendix A. These analysis provide the following eigenvalues describing the MI dynamics:

$$\lambda_{\pm} = (1-\alpha)\left[\Psi \pm \sqrt{\Psi^2 - 1}\right] \tag{3.1}$$

with

$$\Psi = \cos(\mu L)\cos(\phi) - \zeta \operatorname{sinc}(\mu L)\sin(\phi) \tag{3.2}$$

The parameter $\phi = \phi_0 + \gamma L P$ corresponds to the total phase accumulated over a cavity round-trip and:

$$\mu = \sqrt{\beta_2^2 \Omega^4/4 + \beta_2 \gamma P \Omega^2} \tag{3.3}$$

is the standard MI gain with Ω the pulsation of the perturbation and $\zeta = \beta_2\Omega^2 L/2 + \gamma P L$. It can be easily checked that unstable eigenvalues ($|\lambda_{\pm}|>1$) appear only for $|\Psi| > (1-\alpha+1/(1-\alpha))/2$ and are always real such as these eigenvalues can be expressed as $\lambda = |\lambda| e^{im\pi}$ with m integer. We introduce λ' that corresponds to the eigenvalue $\lambda_{\pm}$ with the highest modulus, hence the unstable spectral components grow from noise as $\exp(G(\Omega)L) = [|\lambda'|\exp(im\pi)]$ at each round-trip. Consequently, the gain can be expressed as $G(\Omega) = [\ln(|\lambda'|) + im\pi]/L$ and it follows two distinct cases depending on m parity. In both cases, the initial perturbation grows exponentially with the power growth rate $g(\Omega) = \ln(|\lambda'|)/L$ ($\Re(G(\Omega))$) round-trip to round-trip. This leads to a periodic modulation of the initial cw state. In the even case (i.e. $\lambda' > 1$), the perturbation increases in phase ($\Im(nG(\Omega)L) = 2n\pi$, n: round-trip number) at every round-trip following a P1 regime (see Fig. 3.1(a) showing two consecutive round-trip temporal traces of this regime). However, for the odd case (i.e. $\lambda' < 1$), the perturbation changes of sign at every round-trip ($\Im(nG(\Omega)L) = n\pi$)

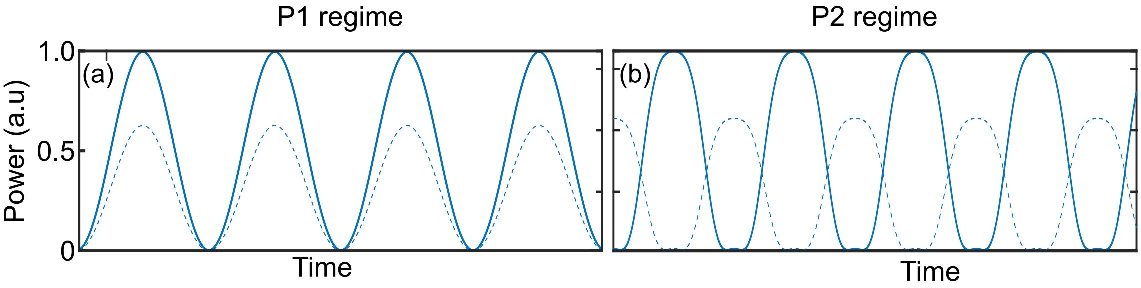

Figure 3.1: Cartoon of two temporal traces of consecutive round-trips for (a) P1 regime and (b) P2 regime. The dashed lines stand for the round-trip 1 and solid lines for round-trip 2.

that is characteristic of P2 regimes. It results in a clear evidence of this regime in the temporal domain, where the periodic pattern experiences an additional π phase shift round-trip to round-trip (see Fig. 3.1(b)) contrary to the P1 regime.

3.1.2 P1 and P2 regimes occurrence conditions

As in the previous chapters, MI exists when the most unstable frequencies $\pm\Omega_T$ are real and when $g(\Omega_T)$ is real and positive. Further developments of the linear stability analysis of the full Ikeda map system has been proposed in Ref. [120], giving analytical solutions of $\pm\Omega_T$ and $g(\Omega_T)$. These solutions are obtained in the case of a high cavity finesse and moderate power. It allows to predict analytically the range of parameters where P1 and P2 regimes arise close to the MI cavity threshold. Our experimental investigations of the P1 and P2 regimes were performed in a cavity with a moderate finesse ($\mathcal{F} \approx 19$). Moreover, we even study some configurations where P is one order of magnitude higher than the cavity threshold preventing us from using this analytical approximation. Thus, we use numerical analysis of Eq. (3.1) to get an accurate description of the MI dynamics. This procedure provides a clear overview of the behavior of the system in terms of P1/P2 regimes by looking at the maximum gain value calculated from the growth rate g

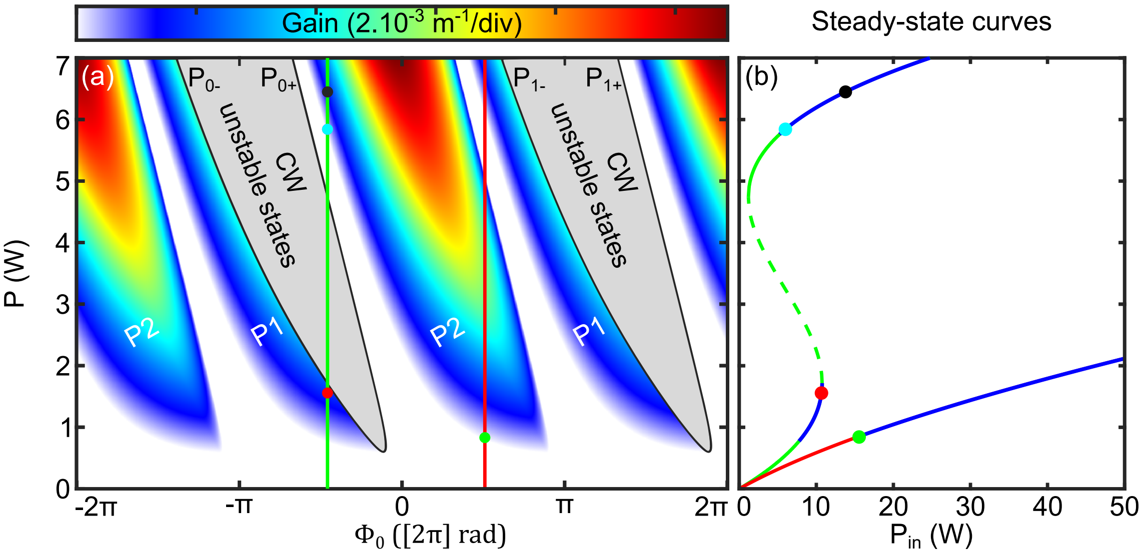

Figure 3.2: (a) 2D-map of the maximum parametric gain in the plane (Φ_0, P) from the Ikeda map model in the case of a normal dispersion regime. The green and red vertical lines stand for $\delta_0 = 1.44$ rad and $\delta_0 = -1.6$ rad, respectively. (b) Steady-state curves with the same color code. CW unstable states correspond to gray areas in (a) and dashed curve in (b) while blue curves in (b) stand for the region where P1 and P2 regimes can be excited in (a). Parameters: $\beta_2 = 9$ ps^2.km^{-1}, $L = 120.6$ m, $\gamma = 2.5$ W^{-1}.km^{-1}, and $\alpha = 0.165$.

in the (ϕ_0, P) plane (see Fig. 3.2(a) for normal dispersion regimes and Fig. 3.3(a) for anomalous dispersion regime). This representation is relevant since it allows a comprehensible description of the system and these parameters correspond to those that are easily managed in experiments: $\phi_0 = 2k\pi - \delta_0$ through the detuning δ_0, and $P = \tilde{\theta}^2 P_{in}/\left[1+\tilde{\rho}^2 - 2\tilde{\rho}\cos(\phi)\right]$ (steady-state Eq. (1.12)) through the input power P_{in}. Let's first analyze the case of the normal dispersion regime depicted in Fig. 3.2(a). We observe two gray domains bounded by the curves $P_{k\pm}$ ($k \in \mathbb{Z}$) and labeled *"CW unstable states"*. They correspond to unstable regions with respect to homogeneous perturbations (negative slopes of the steady-state curve Eq. (1.12)). Beyond this observation, the system alternates between narrow instability tongues emerging on the left side of *"CW unstable states"* domains and broad instability tongues. These tongues are associated to P1 and P2 regimes, respectively. Note that as soon as the pump power is above a certain threshold that depends on the amount of losses, the system might enter in one of the unstable region. We can point out that this mapping is necessarily 2π-periodic with respect to ϕ_0, owing to the periodicity of the linear resonances of the cavity. Then, we compared the case of normal dispersion regimes to the anomalous ones, depicted in Fig. 3.3. Gray area bounded by the curves $P_{k\pm}$ ($k \in \mathbb{Z}$) corresponds to unstable regions with respect to homogeneous perturbations. We observe a 2π-periodic alternation with Φ_0 of P1 and P2 instability tongues. However, we note some differences with the previous case. First, the P1 and P2 tongues emerge respectively on the right side and left side of *"CW unstable states"* domains. Second, the domain of the P1 and P2 instability tongues are quite more important. Finally, the P1 and P2 instability domains merge at some points. The latter difference is likely to hinder the distinct observation of both regime dynamics in experiments, that's why we focus our work

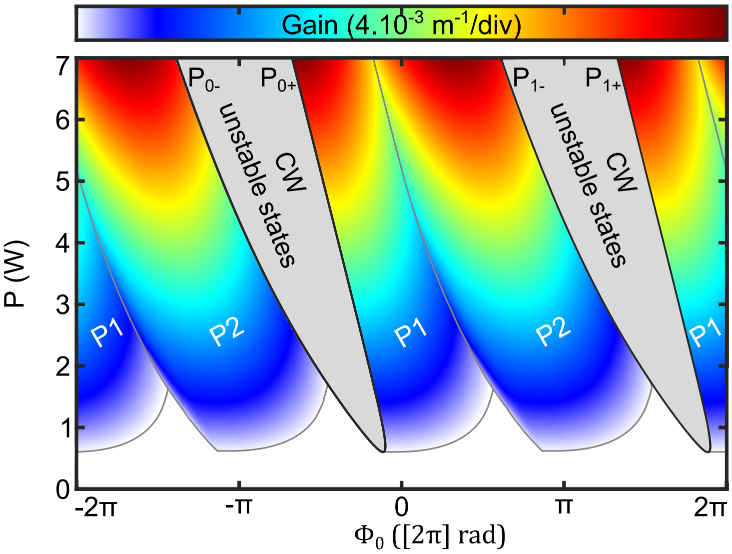

Figure 3.3: 2D-map of the maximum parametric gain in the plane (Φ_0, P) from the Ikeda map model in the case of an anomalous dispersion regime. Parameters: $\beta_2 = -9$ ps^2.km^{-1}, $L = 120.6$ m, $\gamma = 2.5$ W^{-1}.km^{-1}, $\alpha = 0.165$.

and our experiments on cavities operating in the normal dispersion regime.

It has been highlighted in Ref. [51] that most of the features of the system can be illustrated by considering only two scenarios at the MI cavity threshold: the first one, where the nonlinear phase is close to $2k\pi$ ($k \in \mathbb{Z}$), and the second one where the phase is close to $(2k+1)\pi$ ($k \in \mathbb{Z}$). These two cases have been called resonant (P1 regime) and anti-resonant (P2 regime) cases in Ref. [51], respectively. Nevertheless, well above this threshold this denomination is not relevant anymore. Indeed, the nonlinear phase shift ($\phi_{NL} = \gamma L P$) induces a displacement of resonances peaks of several radians. Thus, we shall use the more relevant denomination of positive and negative detuning (δ_0) in order to correctly identify the different scenarios.

From this denomination we first consider the case of positive detuning as regards the central resonance ($\phi_0 = 0$ rad, $k = 0$) and we set as an example the detuning to $\delta_0 = 1.44$ rad ($\phi_0 = -1.44$ rad) indicated by the green vertical line in Fig. 3.2(a). As we can see from the steady-state curve (Eq. (1.12)) depicted with the green line in Fig. 3.2(b), the cavity operates in a bistable regime ($\Delta = 8.7$). Dashed part stands for cw unstable states (grayed part in Fig. 3.2(a)) belonging to negative slope of the steady-state curve while blue lines indicate MI unstable states as regards unstable domains in Fig. 3.2(a) (gray areas). By increasing the pump power above the first instability threshold until $P = 1.56$ W (red dots in Fig. 3.2(a)-(b)), we expect to observe a stable periodic pattern round-trip to round-trip that corresponds to the P1 regime. Indeed, the lower-branch is known to be modulationally unstable for a normalized detuning $\Delta > 4.25$ [55]. By increasing the intra-cavity power until $P = 6.44$ W (black dots in Fig. 3.2(a)-(b)), the system switches on the upper-branch of the steady-state curve and falls within another instability tongue associated to a P2 regime. Then, by decreasing the intra-cavity power until $P = 5.84$ W (cyan dots on Fig. 3.2(a)-(b)) we reach the left side limit of the P2 instability tongues and the MI threshold of the upper-branch. Below this limit the system comes back to a stationary steady-state and eventually switches on the lower-branch of the bistable cycle below $4,74$ W.

Then, we set the detuning to the negative value $\delta_0 = -1.6$ rad ($\phi_0 = 1.6$ rad) indicated by the red vertical line in Fig. 3.2(a). As we can see from steady-state curves (Eq. (1.12)) depicted with the red line in Fig. 3.2(b), the cavity operates in a monostable regime ($\Delta = -9.7$). For such detuning by increasing the power above the first instability threshold until $P = 0.83$ W (green dots in Fig. 3.2(a)-(b)), we expect to observe a stable periodic pattern round-trip to round-trip that corresponds to the P2 regime. As the previously studied positive detuning case, it is also possible to switch to the next P1 tongues. However, it requires a huge amount of power $P_{in} \approx 180$ W, which is not easily accessible with experimental setups, including the one we have built to investigate these different cases presented here.

3.2 Modified experimental setup and time-lens implementation

The experimental setup is depicted in Fig. 3.4. It consists of a passive fiber cavity built with a specially designed dispersion shifted fiber (DSF, $\beta_2^{DSF} = 9$ ps^2.km^{-1} at $\lambda_{pump} = 1550.5$ nm and $\gamma^{DSF} = 2.5$ W^{-1}.km^{-1}) and a 90/10 coupler made of the same fiber to get a perfectly uniform cavity of 120.6 m long (coupler+fiber). The operating principle of this device to stabilize and analyze the dynamics of the system is similar to the one presented in chapter 1, but we added two major modifications. The first one consists in implementing a time-lens system to record the MI temporal pattern from the cavity output signal, and the second one to improve the cavity stabilization, which has been necessary to observe P1 and P2 regimes.

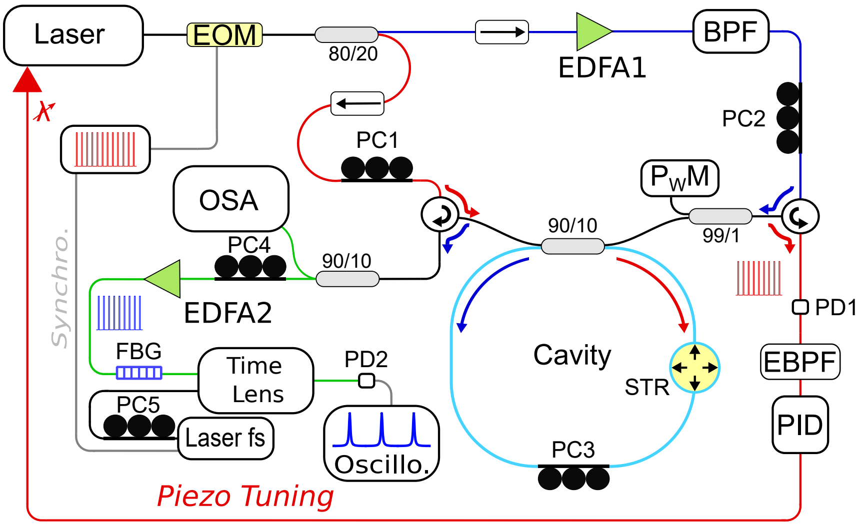

Figure 3.4: Experimental setup. EOM, electro-optical modulator; PC$_{1-5}$, polarization controller; PD$_{1-2}$, photodetector; OSA, optical spectrum analyzer; EDFA, erbium-doped fiber amplifier; BPF, band-pass filter; EBPF: electronic band-pass filter; STR: fibre stretcher; Laser fs: femtosecond laser; Oscillo., oscilloscope; PID, proportional-integrate-derivate controller; FBG, fiber Bragg grating; P$_W$M, power-meter.

3.2.1 Setup improvement

First, we wanted to be able to observe both P1 and P2 regimes at the MI cavity threshold, but the latter requires more power than allowed by the initial setup. Either we changed the pump beam line to reach these power or we used a longer cavity to decrease the MI cavity threshold ($P_{th} = \alpha/(\gamma L)$). We chose the latter solution but we faced a major problem. Indeed, by using longer cavity decreased at the same time the MI and SBS thresholds. Consequently, the cw reference generates an additional Brillouin wave propagating in the anti-clockwise direction that affects the pump beam. If we reduce the power of the cw reference to stay below this SBS threshold, we obtain a too low signal to noise ratio to stabilize the cavity. To prevent this, instead of using a fraction of the cw laser field for the reference, we take a part of the EOM output power through a 80/20 coupler propagating a train of 1 ns pulses in the cavity, short enough to avoid Brillouin effects. Therefore, the cavity output pulse train envelope from the reference carries the variations undergone by the beam during its propagation inside the cavity. This signal is then detected from the cavity output by a photodetector (PD1) and filtered through an electronic band-pass filter (EBPF) to extract this envelope used as a reference signal by the PID to stabilize the system. As an example, we show in Fig. 3.5(a) the cavity output signal from the reference when we are performing a wavelength scan. The red curve stands for reference pulse train recorded before the EBPF where we distinguish each of the pulses only from the zoom on the resonance (b). The black curve corresponds to the recorded signal of EBPF output giving the pulse train envelope with a quite good accuracy. A strong noise is observed on the top level, but it does not affect the stabilization since we stabilize on the response function slope. Note that through this method we sample the perturbations experienced by the pump beam. Nevertheless, the pulse repetition rate of the MHz order for cavities of such length is significantly larger than the external perturbation frequencies, which permits to obtain the stabilization.

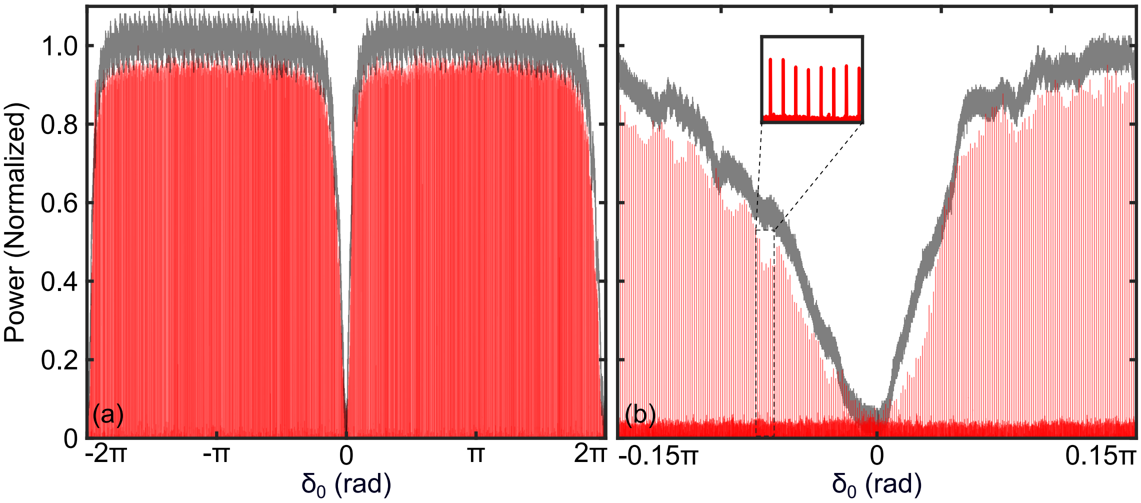

Figure 3.5: (a) Output cavity reference response function. Red lines, before the electronic band-pass filter (EBPF), and black line after. (b) Zoom on a resonance.

3.2.2 Time-lens implementation

The second modification brought to this setup was to implement a device to record the MI temporal pattern with a sub-picosecond resolution in real-time. Indeed, even an ultra-broadband oscilloscope combined to a high-speed photodiode, providing single-shot recordings, does not allow to reach a sufficiently high resolution to discern the temporal waveforms whose period lies in the picosecond scale (max 100 GHz of bandwidth). Obviously, multiple-shot sampling and auto-correlation techniques [55, 56, 90] can achieve the required resolution, but these techniques do not allow to record fast events such as MI process in real-time. We need a single-shot measurement to observe the round-trip to round-trip dynamics. To fulfill both conditions we used a time-lens system [102]. This recent instrument has attracted a lot of attention and has been used to study, in real-time, optical rogues waves [135,136] and breathers [136] as well as to characterize the transient dynamics in active lasers [137]. Time-lens relies on the fundamental concepts of time-imaging and space-time duality originally proposed by Kolner *et al.* in 1989 [101]. This concept implies that for a spatial optical component such as a lens, it exists its temporal counterpart namely a time-lens. A spatial optical lens magnify the image of an object in front of the lens without distorsion, whereas a time-lens magnify the temporal waveform without distortion. Note that spatial lens adds to the optical field a quadratic phase delay in the spatial domain, so time-lens must also add a quadratic phase but in the time domain. In our case, we implemented in our setup a commercial time-lens (Picoluz ultra-fast temporal magnifier, Thorlabs) based on the results published in Ref. [102], where the quadratic phase is ensured by a nonlinear process. A strong pump is linearly chirped in order to impose a temporally quadratic phase profile. Then, this pump field (E_i) is mixed with the signal field (E_s) to analyze in a device based on silicon nano-waveguide. It generates an idler field (E_i) via four-wave mixing (FWM) process on which the quadratic phase of the pump is imprinted ($E_i \propto E_p^2 E_s^*$). Note that we added polarization controllers on each path (PC4-5 in Fig. 3.4) in order to optimize the FWM process efficiency. This idler wave is isolated from the pump and the signal thanks to a highly selective band pass filter. This idler wave after propagation in a fiber corresponds to the magnified signal that can be observed thanks to a ultra-broadband sampling oscilloscope and a high-speed photodiode (70 GHz bandpass each). The pump used in this work is a femtosecond laser centered at 1570 nm that provides pulses with a fixed repetition rate of about 100 MHz. This laser serves as a reference clock for the EOM such as the repetition rate of pulses sent to the cavity is an exact multiple of the femtosecond laser (typically 59 times in our case). To drive coherently the cavity, we roughly adjusted the cavity length by cutting or adding pieces of fiber with a precision of a few centimeters. We then added a fiber stretcher (STR) to finely tune this length (range of 8 cm, ≈ 1 kHz) in order to match the cavity repetition rate to the one of the pulse train sent to pump the system. Thanks to this time-lens with a magnification factor of 57, we were able to record the temporal pattern of the output pulses over a window of 50 ps. The resolution achieved with this time-lens is approximately of 300 fs, which is short enough to resolve the MI temporal pattern (period as short as 3.7 ps as we will see below) round-trip to round-trip.

3.3 Experimental results

We investigated the different regimes identified by red, cyan, black and green points in Fig. 3.2. We recorded, for each case, the output cavity spectra obtained from an OSA as well as their consecutive temporal traces when the system has reached a stationary regime. These experimental results have been compared to numerical simulations of the Ikeda map model. They have been carried out by using square pulses of 1 ns as in experiments by adding a weak random noise. In the case of P1 regime (Turing instability on the lower branch of the bistable cycle), we used a cw pump including monochromatic signal located at the maximum gain frequency (Eq. (3.1)) to seed the process. For such large detunings $\Delta > 4.25$ the process can arise on the lower branch of the steady-states cycle. Nevertheless, the area of instability is really restricted and the system is extremely sensitive to perturbations. Consequently, by seeding the process in such cases with noise should lead to unexpected switches over the upper-branch and avoid the observation of stable temporal patterns over a large number of round-trips (typically 1000 in numerical simulations).

3.3.1 Positive detuning

We first investigated the case of positive detuning by setting $\delta_0 = 1.44$ rad ($\phi_0 = -1.44$ rad). It corresponds to the case of the bistable regime depicted by the green lines in Fig. 3.2(a)-(b).

3.3.1.1 P1 regime

We first increased the input power to reach the first instability tongue corresponding to P1 regime. It corresponds to the red point (see Fig. 3.2, $P = 1.56$ W) located on the lower branch of the steady-state function as depicted in Fig. 3.6(a). We note from the experimental output cavity spectrum displayed by an orange line in Fig. 3.6(b) that a pair of sidebands located at ±140 GHz arises with amplitudes of approximately 35 dB below the pump power. These results are in excellent agreement with numerical simulations and theoretical predictions from Eq. (3.1) depicted by blue and green dotted lines (±154 GHz), respectively. It is quite noteworthy that numerical simulations and experiments give a very similar sidebands powers. However, we discern a spectrum asymmetry from experimental recording. In particular, we observe a consistent first harmonic on the Stokes side of the spectrum, but these first harmonic is almost indistinguishable from the noise on the Anti-Stokes side. It has been demonstrated that third-order dispersion term could be responsible for such behavior [105,114]. Indeed, by performing numerical simulations (not reported here) by adding this term, we observed this symmetry breaking. Nevertheless, the

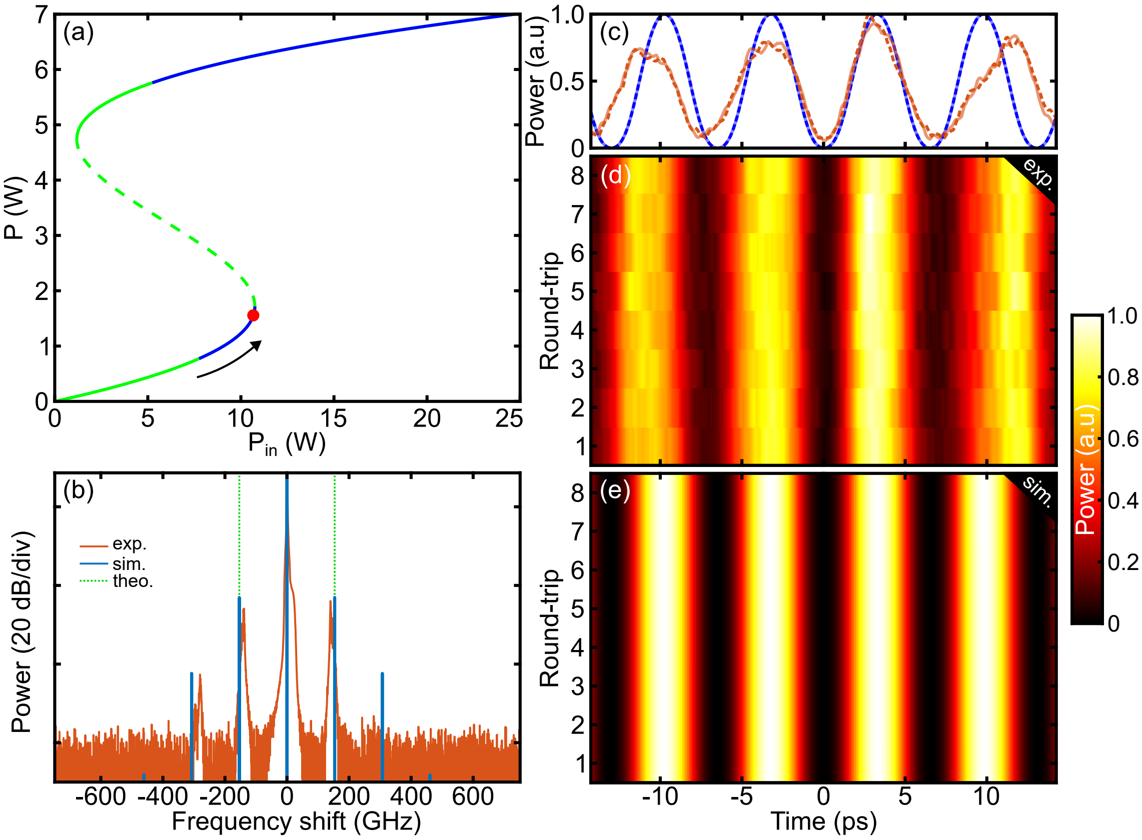

Figure 3.6: (a) Steady-state curve, blue parts: instability domains, red dot: investigated configuration. (b) Output cavity spectra from experiments and numerical simulations. 2D-color plot of 8 consecutive temporal traces from experiments (d) and numerical simulations (e). (c) Last two consecutive traces from experiments (orange lines) and simulations (blue lines), dotted and solid lines stand for round-trip 7 and 8, respectively. Parameters: see Fig. 3.2's captions.

ratio between Stokes and Anti-Stokes harmonics is only a few decibels when it is about 10 dB in experiments. Fig. 3.6(d) displays 8 consecutive temporal traces recorded in a 2D-color plot when the system reached a stationary regime. Note that we removed the cw component from this traces (since the pump wavelength is filtered) and we normalized the traces such as the maximum and the minimum of them correspond respectively to 1 and 0. This normalization allows for a clear overview of the pattern and easily identify the type of MI regime. In Fig. 3.6(d) we observe that a periodic pattern with a period of 6.93 ps settles down inside the cavity, reproducing itself round-trip after round-trip. Moreover, the plot of the last two consecutive temporal traces depicted with orange lines in Fig. 3.6(c) shows a quasi-perfect overlap. Thus, it proves that the cavity operates in a P1 regime as predicted by the theory. These results are confirmed by numerical simulations[1] whose

---

[1] For a clear contrast of the modulation in the temporal domain, we prefer to show the intracavity dynamics rather than the output-cavity dynamics. Indeed the latter one incorporates 90%

temporal traces are depicted in Fig. 3.6(e) and in Fig. 3.6(c) by blue lines. They correspond respectively to 2D-color plot of the intra-cavity temporal signals and last two consecutive round-trip traces depicted in Fig. 3.6(e). Beyond the perfect overlap between the last two consecutive traces from numerical simulation depicted with blue lines in Fig. 3.6(e), the period pattern of 6.51 ps is in good agreement with the experimental one.

3.3.1.2 Chaotic regime

We increased the input power to move on the second instability tongue corresponding to P2 regime meanwhile the system switches to the upper-branch (P2 regime) of the bistable cycle (see Fig. 3.7(a)). We increased the input power up to the operating point identified by the black dot in Fig. 3.2 ($P = 6.44$ W). Fig. 3.7(b) depicts the recorded output cavity spectrum with an orange line. It exhibits a background surrounded by two bands of instability. These bands, located at ±264 GHz, exhibit a discrepancy of about 10% with theory (calculated from Eq. (3.1)), which predicts bands located at ±237 GHz, marked by green dotted lines in Fig. 3.7(b). The temporal traces recorded for 8 consecutive round-trips are shown in a 2D-color plot in Fig. 3.7(d). We note that the system does not follow neither a P1 nor a P2 regime. Actually, we excited a temporal chaotic regime, where temporal traces exhibit a "random" pattern changing at each round-trip. This is particularly visible in Fig. 3.7(c) that displays the last two recorded traces by orange lines. Such a behavior has been predicted in spatially extended cavities and it resides in the development of transverse MI for plane waves circulating in the resonator [126, 139]. These results are confirmed by corresponding numerical simulations. The numerical spectrum displayed in Fig. 3.7(b) (blue line) exhibits as well a background surrounded by two bands of instability. The location and amplitudes of these bands, as well as the level and width of the background are in good agreement. Fig. 3.7(e) depicts the temporal traces from numerical simulations and shows exactly the same chaotic behavior as in experiments. This is also visible in Fig. 3.7(c), which displays with blue lines the last two traces. These results from experiments and numerical simulations disagree with theory predicting a P2 regime for such configuration. The theory developed to predict the different regimes of the cavity and their respective operating domains is based on a linear stability analysis of the full map system (Eqs. (1.8-1.9)) that takes into account only weak perturbations of the system. This approach is justified close to the cavity MI threshold. However, in this case we are well above it, and the system enters a fully nonlinear regime, which is not captured by our linear analysis.

---

of the input-pump (cw wave), decreasing the visibility of the generated patterns.

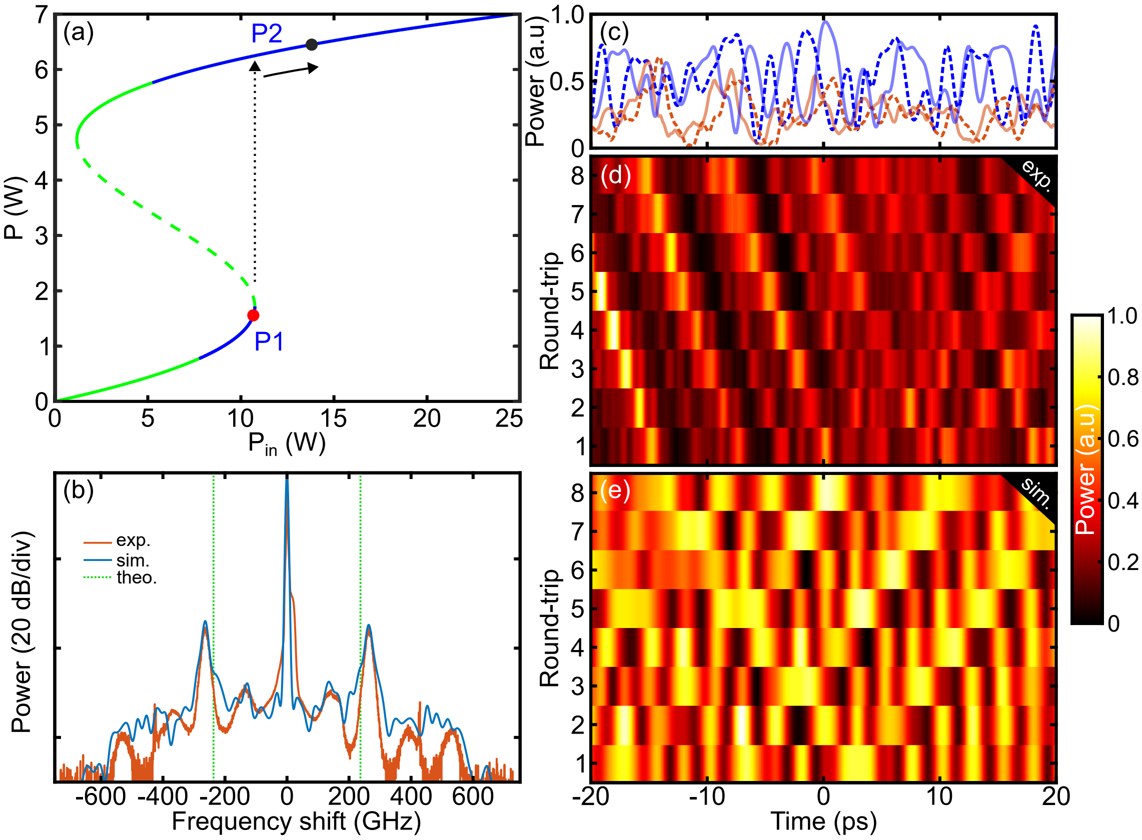

Figure 3.7: (a) Steady-state curve, blue parts: instability domains, black dot: investigated configuration. (b) Output cavity spectra from experiments and numerical simulations. 2D-color plot of 8 consecutive temporal traces from experiments (d) and numerical simulations (e). (c) Last two consecutive traces from experiments (orange lines) and simulations (blue lines), dotted and solid lines stand for round-trip 7 and 8, respectively. Parameters: see Fig. 3.2's captions.

3.3.1.3 P2 regime

We slowly decreased the input power, in order to reach the configuration marked by a cyan dot in Fig. 3.2 ($P = 5.84$ W), just above the lower limit of the upper-branch instability domain (see steady-states cycle in Fig. 3.8(a)). This is the usual technique to adiabatically reach a steady-state point close to the upper knee. The temporal patterns depicted in Fig. 3.8(d) show that the system becomes again periodic. The temporal traces prove unmistakably that the cavity operates in P2 regime, since traces alternate between two out-of-phase periodic patterns (period of 3.70 ps). It displays a characteristic chessboard pattern that is the clear signature of this regime. Corresponding numerical simulations depicted in Fig. 3.8(e) are in excellent agreement with the experiments (period of 3.63 ps). The period-doubling is perfectly visible in Fig. 3.8(c), which depicts the last two consecutive traces from experiments (orange lines), and numerical simulations (blue lines). The recorded output cavity spectrum displayed in Fig. 3.8(b) exhibits two instability bands located at ±273 GHz, whose amplitude is about 35 dB below the pump power. This is in excellent agreement with the theory predicting sidebands located at ±265 GHz, indicated by the green vertical lines, and corresponding numerical simulations depicted by a blue line. It is noteworthy that P2 stable patterns are limited both in experiments and in numerical simulations to a really restricted domain close to the upper-branch MI threshold. By moving away from this threshold, new components arise. First, they arise between the pump and bands frequencies and finally they spread on a large frequency domain leading to a spectrum identified as a chaotic spectrum (by checking the temporal domain). In the temporal domain we observed that during this transition the system switches from periodic regimes P2 to chaotic regimes. Numerical simulations of this transition to chaos show exactly the same behavior. Such features are not specific to our case and were also observed in Ref. [140].

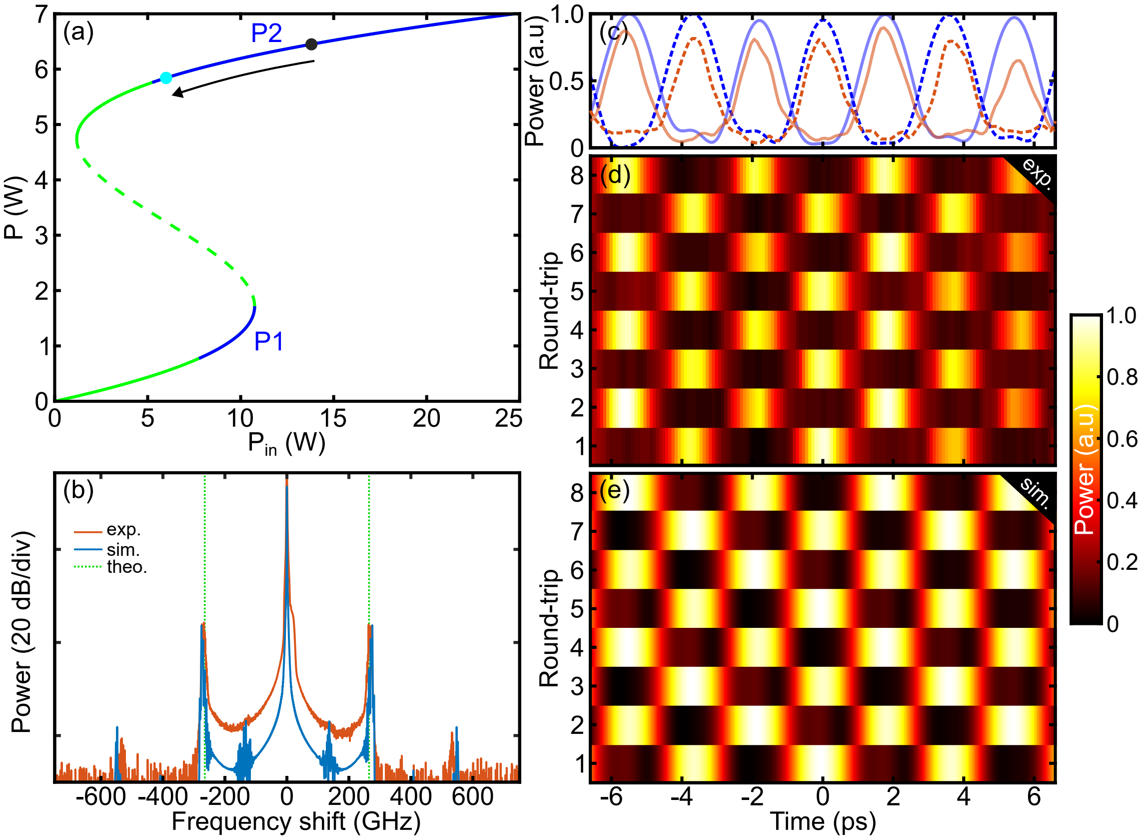

Figure 3.8: (a) Steady-state curve, blue parts: instability domains, cyan dot: investigated configuration. (b) Output cavity spectra from experiments and numerical simulations. 2D-color plot of 8 consecutive temporal traces from experiments (d) and numerical simulations (e). (c) Last two consecutive traces from experiments (orange lines) and simulations (blue lines), dotted and solid lines stand for round-trip 7 and 8, respectively. Parameters: see Fig. 3.2's captions.

3.3.2 Negative detuning

Finally, we investigated the case of negative detuning by setting $\delta_0 = -1.60$ rad ($\phi_0 = 1.60$ rad). It corresponds to the configuration identified by a red line in Fig. 3.2. P2 regime is reached by setting the pump power to $P_{in} = 16.3$ W ($P = 0.83$ W, green dot on the steady-state cycle in Fig. 3.9(b)) just above the MI threshold. The cavity output spectrum is depicted by an orange line in Fig. 3.9(b). It exhibits a pair of sidebands located at ±238 GHz in really good agreement with theory predicting sidebands located at ±221 GHz (calculated from Eq. (3.1) and marked by the green dotted lines in Fig. 3.9(b)) and with numerical simulations (blue line). The normalized temporal pattern recorded for 8 consecutive round-trips is shown in a 2D-color plot in Fig. 3.9(d). We note that traces exhibit an alternation between two π-out-of-phase periodic patterns (period of 4.23 ns) with a singular form of chessboard pattern. This behavior is also clear by looking at the last two round-

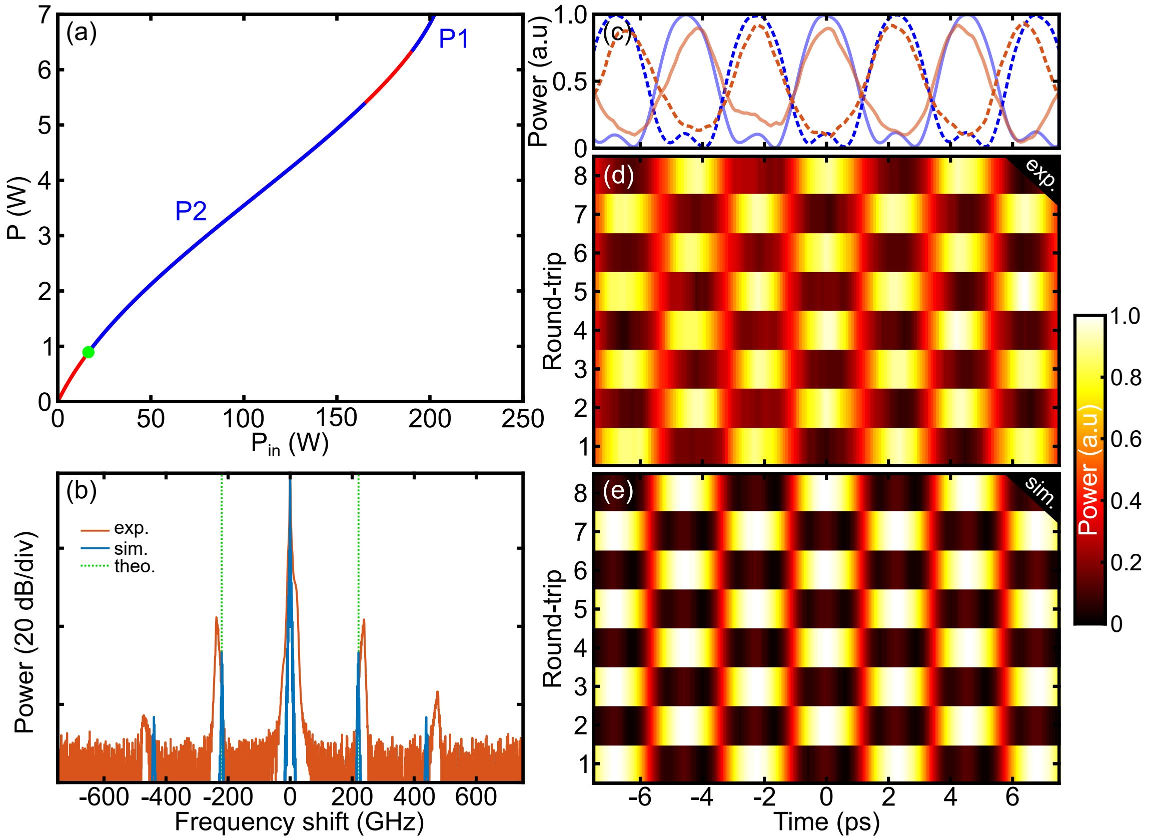

Figure 3.9: (a) Steady-state curve, blue parts: instability domains, green dot: investigated configuration. (b) Output cavity spectra from experiments and numerical simulations. 2D-color plot of 8 consecutive temporal traces from experiments (d) and numerical simulations (e). (c) Last two consecutive traces from experiments (orange lines) and simulations (blue lines), dotted and solid lines stand for round-trip 7 and 8, respectively. Parameters: see Fig. 3.2's captions.

trips whose traces are depicted in Fig. 3.9(c) (orange lines). The system undergoes a P2 regime as predicted by the theory. Experimental temporal recordings are also in excellent agreement with numerical simulations (blue lines in Fig. 3.9(c) and in Fig. 3.9(e) corresponding to the 2D-color plot from intra-cavity temporal signal). Simulations show as in experiments the peculiar alternation between temporal traces (period of 4.52 ns, see Fig. 3.9(e)). It is also clear by looking at the last two temporal traces depicted by blue lines, where they almost perfectly overlap with experimental traces (orange lines).

As in the previous positive detuning case, we could increase the power to switch on the next upper tongue, where we expect that a P1 regime settle down inside the cavity (Fig. 3.9 (a)). However, this requires a huge amount of input power to be achieved of about $P_{in} \approx 180$ W, too far from what we are able to generate with our setup.

3.3.3 Impact of the cavity synchronization mismatch on MI

To illustrate the impact of synchronization on MI we report in Fig. 3.10 an example corresponding to the configuration of P1 regime (red dot in Fig. 3.2(a)). We simultaneously recorded the temporal pattern and the cavity output spectrum for three different values of synchronization, by changing the cavity length thanks to the stretcher. Fig. 3.10(a)-(b)-(c) shows the temporal patterns in a 2D-color plot on more than thirty round-trips for synchronization mismatches of $\Delta t/L \approx -6$, 0, and 1.8 ps.km^{-1} ($\Delta L \approx -0.148, 0$ and 0.044 mm), respectively. Fig. 3.10(d) depicts the recorded spectra. The blue, red, and green curves correspond to spectra recorded simultaneously with temporal patterns of Fig 3.10(a)-(b)-(c), respectively. We observe, for cases where the cavity is not synchronized (blue and green cases), a drift of the MI temporal patterns to negative/positive temporal values for negative/positive synchronization mismatches (see Fig. 3.10(a)-(c)). These drifts are of approximately 11 % and 3% of the pattern period per round-trip for $\Delta t/L = -6$ and 1.8 ps.km^{-1}, respectively. In the case of perfect synchronization depicted in Fig. 3.10(b), the temporal pattern reproduces to itself round-trip after round-trip. Then, by looking at the corresponding output cavity spectra depicted in Fig. 3.10(d), the synchronization seems not to affect the spectral domain. However, deepening our study, we note from the zoom on the Anti-Stokes sidebands (see Fig. 3.10(e)) that the synchronization impacts the peak power of MI sidebands. Indeed, it reaches a maximum for a perfect synchronization (red curves in Fig. 3.10(e)) and decreases with an increasing synchronization mismatch. For $\Delta t/L = -6$, and 1.8 ps.km^{-1} the peak value of the sidebands power compared to the perfect case are decreased by more than 6 dB (blue curves in Fig. 3.10(d)-(e)) and 3 dB (green curves in Fig. 3.10(d)-(e)), respectively. For higher desynchronizations, we observed in experiments that the sidebands quickly vanish, while in the temporal domain, we do not any longer observe periodic patterns. This power dependence of MI sidebands was also observed in other cases investigated in this work. We have exploited this property in a straightforward manner to perfectly synchronize the cavity.

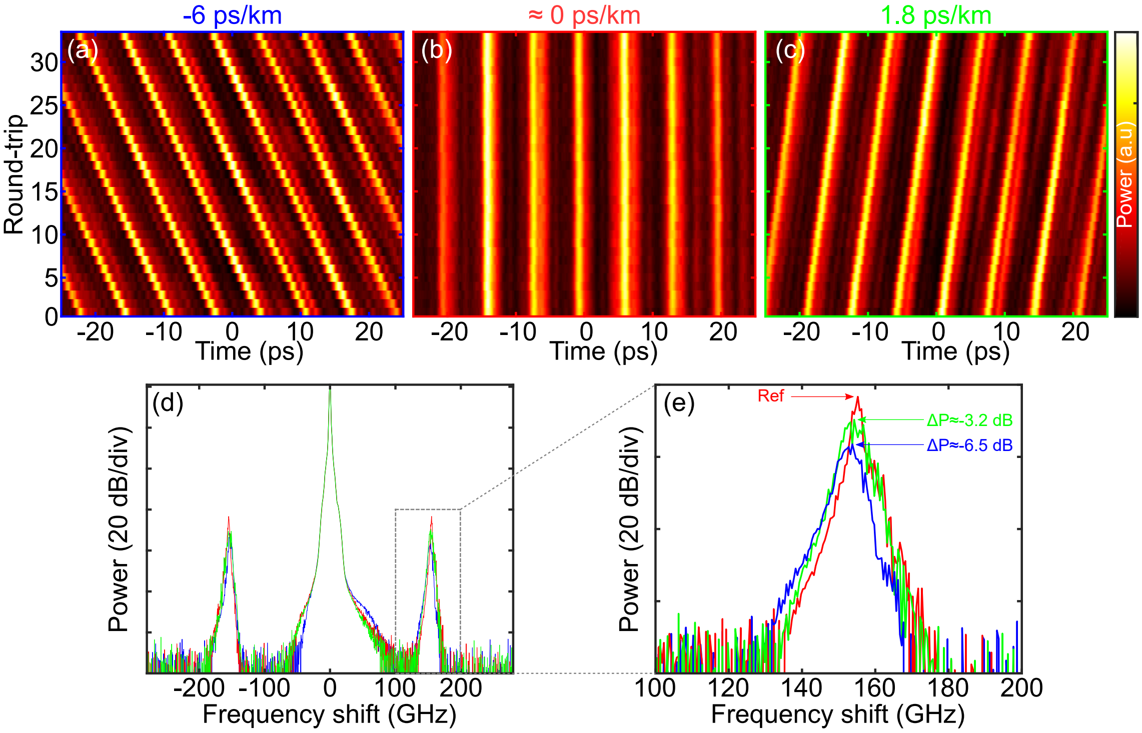

Figure 3.10: (a), (b), and (c) correspond to the 2D-color plot of 33 consecutive temporal traces recorded for synchronization mismatches of -6, ≈ 0, 1.8 ps^2.km^{-1} respectively. (c) Corresponding cavity output spectra. Blue, red, green curves stand for $\Delta t/L = -6$, 0 and 1.8 ps.km^{-1}, respectively. (b) Zoom on Anti-Stokes band.

Summary

We show that, thanks to a time-lens, the dynamics of MI in passive cavities can be recorded. We demonstrate unambiguously that two different processes of MI with period-1 and period-2 can arise in this kind of system. Moreover, our results directly show the limit of the mean-field model (LLE), which is not able to predict period-doubling behaviors coming mostly from the fact that this LLE takes into account only one resonance. Indeed, P2 regime arises for high intra-cavity power and/or large detuning, beyond the LLE domain of validity. To capture the whole dynamics, we highlighted that it is necessary to use the full Ikeda-map model. By applying a linear stability analysis and a Floquet analysis, we can predict exactly the experimental observations. We set the detuning to a positive value such as the system is bistable. As expected from the theory, we observed the P1 regime on the lower-branch of the steady-states cycle. When we increased the power to switch on the upper-branch, the system becomes chaotic, in good agreement with numerical simulations. The theory predicts P2 regime for such parameters, which is in disagreement with observations. It comes from the fact that the linear stability analysis used to describe MI dynamics works for small perturbations, which is not the case when the cavity operates far from the MI cavity threshold. By decreasing the power to reach the MI threshold on the upper-branch, we observed again a temporal periodic signal periodic, and a P2 regime as expected from theory. Finally, we set the detuning to a negative value, where the cavity operates in a monostable regime. We increased the power just above the MI threshold and observed a P2 regime as predicted by the theory.

We point out that we are not the firsts to use the high resolution provide by time-lens to characterize the complex dynamics of fast events in cavities. Indeed, time-lens have also been exploited for the characterization of cavity soliton dynamics in passive resonators [72] and mode-locking laser dynamics in phase and intensity [137]. These latter studies and our results anticipate that time-lens systems, or more recently, dual-frequency combs systems [71] providing an high resolution in real-time, will become a standard technique to characterize fast events in resonators, to improve the understanding of the complex dynamics occurring in cavities.

Chapter 4

Instability in passive fiber-ring cavities through gain-through-filtering process

Contents

Optical frequency combs (OFC), consisting of a series of phase-locked equally spaced laser frequency lines, have attracted a lot of attention in the last decades. Indeed, they are extremely precise rulers that found a lot of outlets [70, 91], ranging from metrology [60, 61] with Lidars [62], or astrophysics to calibrate the astronomical spectrometers used for Earth-like extra-solar planets [63, 64] detection, to ultra-precise spectroscopy and molecular fingerprinting [65–67]. Different techniques have been developed to generate these OFCs such as mode-locking laser [141], spontaneous four-wave mixing in quantum cascade laser [142], parametric four-wave mixing in highly nonlinear fibers [143], difference frequency generation [144] and even externally driven passive resonators either with quadratic nonlinearity [145] or Kerr nonlinearity in microresonators [146]. Microresonators provide today the most ideal platform to generate these OFC in term of compactness and low energy footprint for suitable applications in the fields listed above [58, 147, 148]. Moreover, their high quality factors ($Q = 10^6 - 10^9$) confine strongly the light inside the device [149–151], which allows to generate broadband OFCs from a weak continuous wave. These OFCs can eventually achieve an octave spanning required for specific applications [60, 148, 152–154]. Such OFCs are linked to the formation of temporal cavity solitons [56, 72, 155–157], which occurs only in anomalous dispersion. Due to practical limitation in microresonator fabrication process, such dispersion regimes are extremely challenging to achieve, in particular in the visible. Some solutions have been proposed to overcome this limitation, such as producing OFCs through Faraday instabilities [158] or with dark soliton in normal dispersion region [159, 160]. However, it requires a careful design of the device, and the comb repetition rate cannot be tuned in the latter solution since it depends on the fixed opto-geometrical parameters of the microresonator.

In this chapter, we propose a new concept based on gain-through-filtering process (GTF) to generate OFCs in normal dispersion regimes, and overcome the tunability limitation. This mechanism is a generalization of the gain-through-losses (GTL) concept, a parametric process that induces MI through unbalance losses for signal and idler waves [161, 162]. GTF generalizes the GTL mechanism by including the contribution of dispersion naturally associated to the filter dissipation profile through causality relation (Kramer-Kronig relation [163]). We demonstrate for the first time that GTF can generate MI that leads to the formation of OFCs by subsequent FWM process between the pump and the MI sidebands. Moreover, we show that OFCs repetition rate can be easily tuned, by simply modifying the detuning between the pump frequency and the central frequency of the filter.

The chapter is organized as follows. In the first section, we recall the theoretical development done by A. M. Perego and M. Conforti to describe the GTF process in resonators. In particular, we show the derivation of a phase-matching equation that predicts the repetition rate of generated OFCs. In the second section, we detail the experimental setups used to record the spectra and to record the temporal traces. In the last section, we report our experimental results. First, we show the OFCs generation through GTF, then we demonstrate the tunability and finally we show the corresponding temporal traces recorded for these combs.

4.1 Theory of gain-through-filtering in passive fiber-ring cavities

In this section we recall the theoretical development done by A. M. Perego and M. Conforti to describe the GTF process. We start from the following Ikeda map system:

$$\begin{cases} \dfrac{\partial E(z,\tau)}{\partial z} = i\left(-\dfrac{\beta_2}{2}\dfrac{\partial^2}{\partial \tau^2} + \gamma|E(z,\tau)|^2\right)E(z,\tau) & (4.1)\\ E^{(m+1)}(z=0,\tau) = \widetilde{\theta}E_{in}(\tau) + \widetilde{\rho}E^{(m)}(z=L,\tau)\exp(i\phi_0) & (4.2)\end{cases}$$

and we consider that the filter located at the position $z = z_F$ acts in the following way:

$$E^{(m)}\left(z_F^+,\tau\right) = h\left(\tau\right) * E^{(m)}\left(z_F^-,\tau\right) \tag{4.3}$$

$$\widetilde{E}^{(m)}\left(z_F^+,\Omega\right) = H\left(\Omega\right)\widetilde{E}^{(m)}\left(z_F^-,\omega\right) \tag{4.4}$$

The parameter $h(\tau)$ is the filter response, where the causality imposes $h(\tau) = 0$ if $\tau < 0$, $*$ denotes the convolution, $\widetilde{\cdot}$ the Fourier transform and $H\left(\Omega\right) = \widetilde{h}(\omega)$ is the filter transfer function. For the sake of simplicity, we assume that the filter is located just before the coupler ($z_F = L$). Consequently, the boundary conditions are modified in such way that:

$$E^{(m+1)}\left(z=0,\tau\right) = \widetilde{\theta}E_{in} + \widetilde{\rho}h\left(\tau\right) * E^{(m)}(z=L,\tau)\exp(i\phi_0) \tag{4.5}$$

$$E_{out}^{(m+1)}(z=0,\tau) = i\widetilde{\rho}e^{\frac{\alpha_f L}{2}}E_{in} - i\widetilde{\theta}e^{-\frac{\alpha_f L}{2}}E^{(m)}(z=L,\tau)\exp(i\phi_0) \tag{4.6}$$

We remind that $\tilde{\rho} = \rho\kappa\exp\left(-\alpha_f L/2\right)$ and $\tilde{\theta} = \theta\kappa$, where κ accounts for the excess loss (η) from the coupler insertion.

4.1.1 Steady-state solutions

We search the steady-state solutions of the extended Ikeda map system Eqs. (4.1-4.5). These are obtained by following the same method we used in section 1.2.2 to find the steady-state solutions of the standard Ikeda map system (Eqs. (4.1-4.2)). Through this analysis we find the following relation between the pump P and intra-cavity power P_{in}:

$$\frac{P}{P_{in}} = \frac{\widetilde{\theta}^2}{1+\widetilde{\rho}^2|H\left(0\right)|^2 - 2\widetilde{\rho}|H\left(0\right)|\cos\left(\phi + \arg\left[H\left(0\right)\right]\right)} \tag{4.7}$$

where $\phi = \phi_0 + \gamma LP$. Note that owing to the filter implemented inside the cavity the overall phase accumulated by the pump field over a round-trip is modified. The nonlinear phase is not affected and is given by $\phi_{NL} = \gamma LP$. However, the linear phase becomes $\phi_L = \phi_0 + \arg[H(0)]$, where $\arg[H(0)]$ is the phase of the filter at the pump frequency.

4.1.2 Linear stability analysis

The dynamics of the system can be analyzed by applying a Floquet analysis [138] on the extended Ikeda map system (Eqs. (4.1-4.5)). This is performed following the same method described in Ref. [120] including the filter response function $h(\tau)$. From this analysis detailed in Appendix A, we get the following eigenvalues that describe the system:

$$\lambda_\pm = (1-\alpha)\left[\Psi_{GTF} \pm \sqrt{\Psi_{GTF}^2 - W}\right] \tag{4.8}$$

with

$$\begin{aligned}\Psi_{GTF} =& \cos(\mu L)\left[H_e(\Omega)\cos(\phi) - H_o(\Omega)\sin(\phi)\right] \\ &- \zeta \operatorname{sinc}(\mu L)\left[H_o(\Omega)\cos(\phi) + H_e(\Omega)\sin(\phi)\right]\end{aligned} \tag{4.9}$$

$$W = H_e^2(\Omega) + H_o^2(\Omega) \tag{4.10}$$

The parameters $H_{e,o}(\Omega) = [H(\Omega) + H^*(-\Omega)]/2$ and $H_o(\Omega) = [H(\Omega) - H^*(-\Omega)]/(2i)$ are the even and odd part of the filter function $H(\Omega)$, $\mu = \sqrt{\beta_2^2\Omega^4/4 + \beta_2\gamma P\Omega^2}$ is the standard MI gain with Ω the pulsation of the perturbation and $\zeta = \beta_2\Omega^2 L/2 + \gamma PL$. It can be easily checked that unstable eigenvalues ($|\lambda_\pm|>1$) appear only for $|\Psi_{GTF}| > \left[W(1-\alpha)^2 + 1\right]/\left[2(1-\alpha)\right]$, where α accounts for the overall losses except the filter losses over a cavity round-trip. As a result, the perturbations grows as $\exp(g(\Omega)z)$, where the gain is:

$$g(\Omega) = \frac{1}{L}\ln\left[\max\left(|\lambda_-|, |\lambda_+|\right)\right] \tag{4.11}$$

4.1.3 Phase-matching condition

In the following we study and illustrate this theory with a super-gaussian shape filter (SGF) whose spectral response amplitude is given by:

$$|H(\Omega)| = 1 - R\exp\left[-(\Omega - \Omega_f)^4/\sigma^4\right] \tag{4.12}$$

The amplitude profile $|H(\Omega)|$ of this filter is depicted in Fig. 4.1 with a blue line. The depth, the central position, and the spectral width of the filter correspond to the parameters $R = 0.96$, $\Omega_f = 399 \times 2\pi$ rad.ns^{-1}, and $\sigma_f = 160 \times 2\pi$ rad.ns^{-1}

respectively. Note that the causality principle imposes, through Kramer-Kronig relation [163], that the spectral response function of the filter contains a phase term $\psi(\Omega)$ such as $H(\Omega) = |H(\Omega)| \exp(i\psi(\Omega))$. We shows this filter phase profile $\psi(\Omega)$ in Fig. 4.1 with a green line obtained by computing the Bode's magnitude phase relation: $\psi(\Omega) = \arg[H(\Omega)] = -\mathcal{H}[\ln(H(\Omega))]$ [164], where $\mathcal{H}[.]$ denotes the Hilbert transform [165].

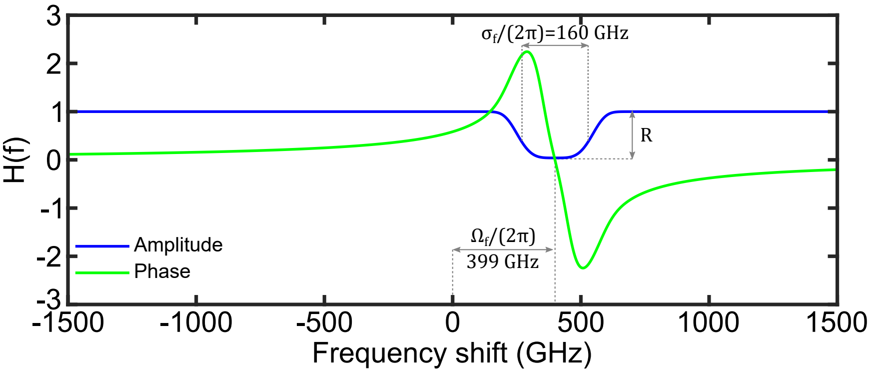

Figure 4.1: Amplitude and phase of the filter with super-gaussian shape. The blue curve stands for the amplitude profile and green curve for the phase profile.

We study the GTF process with this filter implemented in a passive fiber-ring cavity whose dispersion is normal at the pump wavelength. We set the total linear phase to $\phi_L = \phi_0 + \arg[H(0)] = 0$. The corresponding steady-state curve calculated from Eq. (4.7) is depicted in Fig. 4.2(a). The red line stands for cw stable states and blue line for modulationally unstable states. We fixed the input power to $P_{in} = 6.6$ W ($P = 2.2$ W, red dot), in order to pump the cavity above the MI cavity threshold and we plotted the corresponding parametric gain (calculated from Eqs. (4.8-4.11)) in Fig. 4.2(b) by the red curves. It predicts bands located at ±586 GHz. However, it does not allow to dissociate the relative impact of both parts of the filter (dissipation part ($|H(\Omega)|$) and dispersive part ($\arg(H(\Omega))$)) on the parametric gain and position of the band. For this purpose, in Fig. 4.2(b) we superimposed the parametric gain to the gain obtained for a purely dissipative filter and purely dispersive filter depicted with the blue line and green line, respectively. In the case of a purely dissipative filter, we observe two pairs of bands that do not exceed the threshold of GTF. The band located at $\approx$ 400 GHz mimics the shape of the filter and the other bands located at $\approx$ 1400 GHz correspond to boundary conditions induced MI [51]. In the case of a purely dispersive filter depicted with green curves in Fig. 4.2(b), we observe a pair of bands whose amplitude is slightly above that of the gain provided by the full filter (red curves in Fig. 4.2(b)). Moreover, we note that each band consists of two peaks, where the most detuned peaks from the central frequency give a reasonable prediction of the most unstable frequencies provided by the full filter (vertical black dotted lines).

From the last observations, we note that it does not require to take into account the amplitude profile of the filter to determine the position of the most unstable

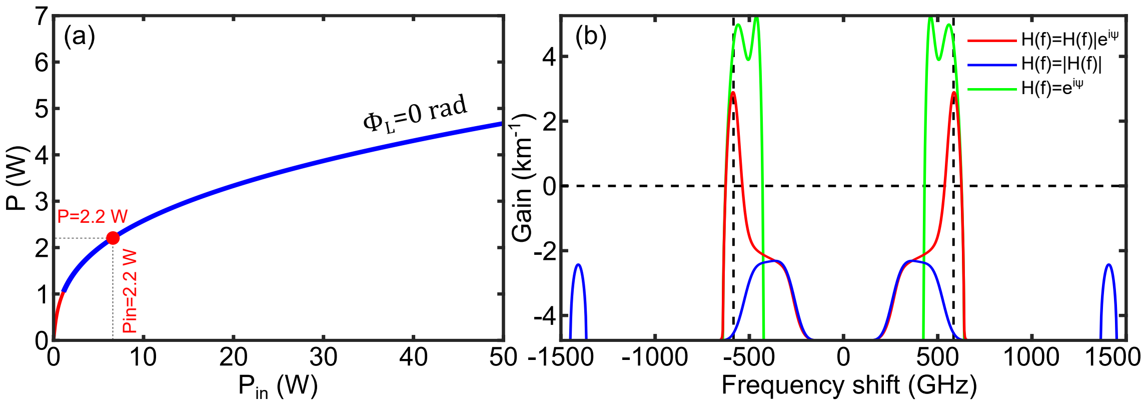

Figure 4.2: (a) Steady-state curve for $\Phi_L = 0$ rad ($\Phi_0 = -0.509$ rad). The red and blue curve depicted the cw stable states and unstable states with respect to GTF process. (b) GTF gain $2g\left(f\right)$ calculated from Eq. (4.11) versus the frequency shift. The red curve correspond to the GTF gain obtained with the filter $H\left(\Omega\right) = \left|H\left(\Omega\right)\right| \exp\left(i\psi\left(\Omega\right)\right)$. The blue and red curves show the effect of magnitude and phase of the filter transfer function on the gain, respectively. Parameters: $\beta_2 = 0.5$ ps^2.km^{-1}, $\beta_2 = 0.12$ ps^3.km^{-1}, $L = 104.2$ m, $\gamma = 2.5$ W^{-1}.km^{-1}, $\Phi_L = 0$, $\Phi_0 = -\arg\left[H\left(0\right)\right] = -0.509$ rad, and $\alpha = 0.22$.

bands. Consequently, we can find the phase-matching relation that rules the position of the sidebands by assuming that the filter response function is:

$$H\left(\Omega\right) = \exp\left(i\psi\left(\Omega\right)\right) \tag{4.13}$$

The even and odd part of the filter transfer function are given by:

$$H_e\left(\Omega\right) = e^{i\psi_o\left(\Omega\right)} \cos\left(\psi_e\left(\Omega\right)\right) \tag{4.14}$$

$$H_o\left(\Omega\right) = e^{i\psi_o\left(\Omega\right)} \sin\left(\psi_o\left(\Omega\right)\right) \tag{4.15}$$

where the $\psi_o\left(\Omega\right)$ and $\psi_e\left(\Omega\right)$ denote the odd and even part of the filter phase, respectively:

$$\psi_e\left(\Omega\right) = \frac{\psi\left(\Omega\right) + \psi\left(-\Omega\right)}{2} \tag{4.16}$$

$$\psi_o\left(\Omega\right) = \frac{\psi\left(\Omega\right) - \psi\left(-\Omega\right)}{2} \tag{4.17}$$

Consequently, Eq. (4.8) is greatly simplified as follows:

$$W = e^{2i\psi_o} \tag{4.18}$$

$$\Psi_{GTF} = e^{i\psi_o}\left[\cos\left(\mu L\right)\cos\left(\phi + \psi_e\right) - \zeta \mathrm{sinc}\left(\mu L\right)\sin\left(\phi + \psi_e\right)\right] = e^{i\psi_o}\widetilde{\Psi}_{GTF} \tag{4.19}$$

and gives the following new eigenvalues:

$$\lambda_\pm = (1-\alpha)e^{i\psi_o}\left[\widetilde{\Psi}_{GTF} \pm \sqrt{\widetilde{\Psi}_{GTF}^2 - 1}\right] \tag{4.20}$$

These eigenvalues, excepting the exponential term, are identical to those that describe the dynamics of MI in standard cavities (see Eq. (3.1) and [51, 120]). The exponential term does not change the modulus of eigenvalues and consequently it does not affect the MI gain. The dynamics of the system becomes unstable when $|\widetilde{\Psi}_{GTF}| > \left[(1-\alpha)^2+1\right] / \left[2\left(1-\alpha\right)\right]$. In the good cavity limit ($\alpha \to 0$), the threshold for instability occurs for $|\widetilde{\Psi}_{GTF}| = 1$. By assuming moderate powers such that $\mu \approx \beta_2\Omega^2/2 + \gamma P$, we find that $\widetilde{\Psi}_{GTF} \approx \cos\left(\mu L + \phi + \psi_e\right)$. Consequently, we get the following simple phase-matching relation:

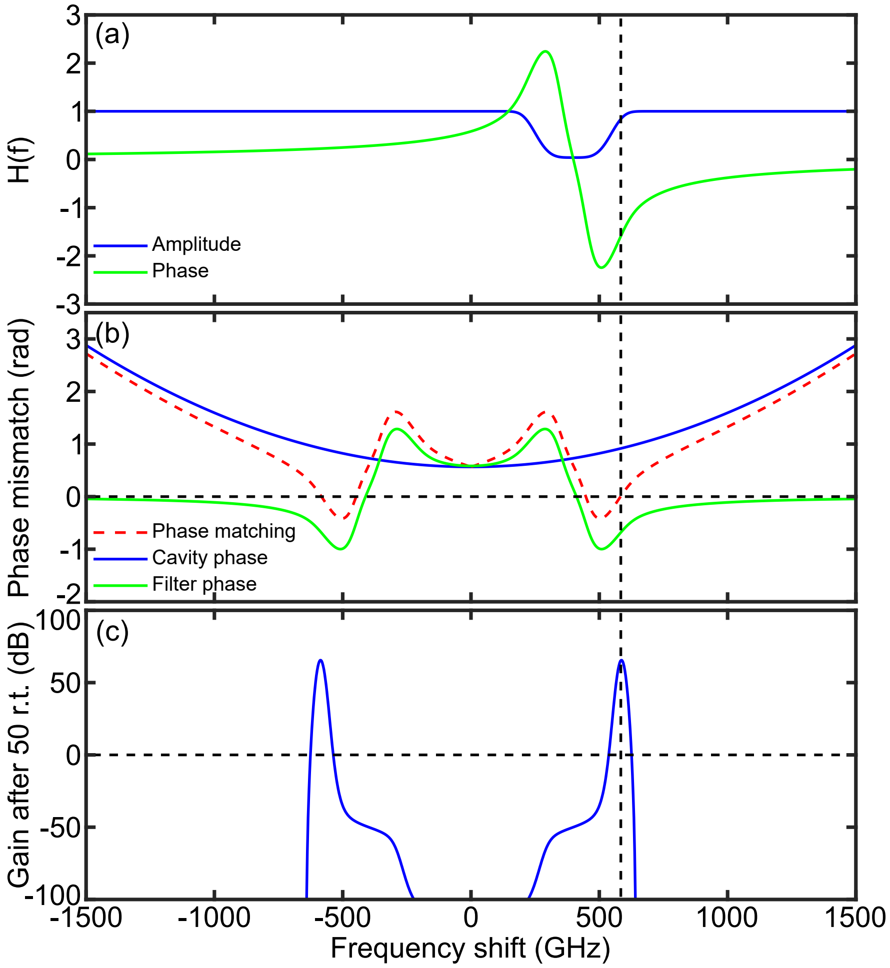

Figure 4.3: (a) Amplitude and phase profile of the SGF. (b) Phase-matching curve calculated from Eq. (4.21) (dashed red curve). The blue curve stands for the cavity induced phase and green cuve for the even part of filter phase. (c) Gain spectrum after 50 round-trip calculated from Eqs. (4.8-4.10).

$$\frac{\beta_2\Omega^2 L}{2} + 2\gamma LP + \phi_0 + \psi_e\left(\Omega\right) = m\pi \quad (m \in \mathbb{Z}) \tag{4.21}$$

The solutions of this equation for $m \neq 0$ correspond to parametric resonances (PRs) induced by the periodic injection of the pump at each round-trip (see chapter 3).

For the parameters we set in this study, these PRs appear, if they exist, at much higher frequency with respect to GTF band. That is why we focus on the $m = 0$ bands in the following. In that case, parametric amplification can be observed only if the left term of Eq. (4.21) that consists in: (i) the phase induced by the dispersion μL, (ii) the phase shift of the cavity $\phi = \phi_0 + \gamma LP$, and (iii) the even part of the phase of the filter, is equal to zero. The phase-matching curve from Eq. (4.21) is depicted in Fig. 4.3(b) with dashed red curve. To clearly identify the relative impact of each term composing the phase-matching equation, we plotted the cavity induced phase with a blue curve and even part of the phase of the filter with a green curve. We note that phase-matching curve cross the x axis in ±448 GHz and ±583 GHz. By looking at the gain spectrum in Fig. 4.3(b), we can see that Eq. (4.21) gives a very good approximation of the most unstable frequencies ±586 GHz. Moreover, we can note from Fig. 4.3(a) showing the phase and amplitude of the filter that the phase-matching frequency is significantly different from the center of the filter, as it is the case for gain-through-losses, where only the dissipative part of the filter is taken into account [161].

4.2 Experimental setup

In order to validate the theoretical predictions, we built a passive fiber cavity that consists of 102 m long of a specially designed dispersion shifted fiber (DSF, $\beta_2 = 0.5$ ps^2.km^{-1} at the pump wavelength, $\gamma = 2.5$ W^{-1}.km^{-1} and $\beta_3 = 0.12$ ps^3.km^{-1}), an isolator, a fiber Bragg grating (FBG1) used in transmission and a 90/10 coupler made of the same DSF. The total cavity length is about 104.2 m (102 m account for the DSF and 2.2 m for the FGB and isolator). The light reflected in the clockwise direction inside the cavity is blocked by the isolator in order to avoid detrimental interactions with the pump field, which propagates in the anti-clockwise direction. The FBG1 implemented inside the cavity has been designed in such way that its phase and amplitude profile match with the SGF studied theoretically. We checked this by recording the loss profile of FBG1 $|H(\Omega)|$ thanks to an optical spectrum analyzer (OSA). This profile of the filter is shown in Fig. 4.4(a) with the solid blue line and it reproduces accurately the amplitude profile of the SGF depicted with the dotted blue line. Then we retrieved the phase profile of FBG1 depicted by a solid green line in Fig. 4.4(a) from the measured filter attenuation profile by computing the Bode's magnitude phase relation. Once again, the FBG1 phase profile reproduces accurately the phase profile of the SGF depicted with dotted green line except at $\Omega \approx 500$ GHz, where we observe a small discrepancy.

In order to stabilize and analyze the dynamics of the system, the operating principle is similar to the one presented in chapter 3. We drove the cavity with a train of square shaped pulses of 1.5 ns, which are generated from a cw laser at 1545 nm chopped by an electro-optical modulator (EOM1). The repetition rate, thanks to an arbitrary waveform generator driving the EOM1, is set to match with the repetition rate of the cavity (1.96 MHz), in order to drive synchronously the system and get one pulse per round-trip. These pulses are then amplified by an erbium-dope fiber amplifier (see EDFA1 on the blue line in Fig. 4.5) and filtered through a thin filter (BPF1, 100 GHz) to remove the spontaneous emission (ASE) in excess.

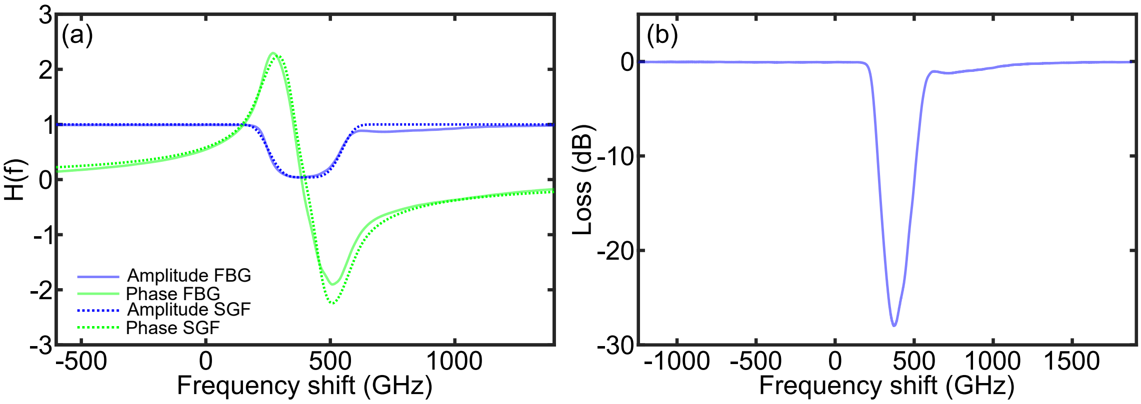

Figure 4.4: (a) Amplitude and phase of the FBG filter (solid lines) and of the filter with the super-gaussian shape (dotted lines). (b) Loss profile of the FBG filter depicted with a logarithmic scale.

We emphasize that in such cavity configuration, we cannot stabilize the system with a reference field that propagates inside the cavity in the opposite direction of the pump signal (clockwise direction). Indeed, this reference field would be blocked by the isolator implemented in the cavity. To prevent this, we implemented the cavity in the experimental setup depicted in Fig. 4.5 that use a reference pulse train propagating in the same direction of the pump pulse train. This is performed by sampling a weak part of the EOM1 output signal thanks to a 80/20 coupler. Then, this weak field is slightly amplified by an EDFA (EDFA2 on the red line in Fig. 4.5) and then combined with the powerful pump pulse train by using a 50/50 polarization maintaining coupler. The reference and pump pulse trains are cross-polarized thanks to polarization controllers added on each path ($PC1-2$, on the red and blue line in Fig. 4.5, respectively) and interleaved in the time domain in order to not interact. Finally, both pulse trains are injected into the cavity through the right input port of the cavity and propagate in the anti-clockwise direction inside the cavity (blue arrow in Fig. 4.5). Note that we added a 99/1 coupler on the pump line just before the 50/50 coupler in order to measure the power of the pump input pulses thanks to a powermeter (PWM).

At the cavity output we added a 90/10 coupler. The signal from the 10% output port of the coupler is used to record the output cavity spectrum with an OSA while the signal from the 90% output port of the coupler has been used to supply two different configurations. The first configuration described in section 4.2.1 has been used to record the output cavity spectra. This configuration provides an accurate measurement of the cavity detuning (δ_0) and allows easy comparisons with theoretical predictions and numerical simulations. In the following, we will call this configuration *setup "A"*. We also planed to record the temporal pattern from the cavity output. However, this first setup does not provide a sufficient stabilization for such recording. Consequently, we built a second setup by modifying slightly the fist setup to improve the cavity stabilization at the expense of a precise detuning measurement. In the following, we call this setup *setup "B"* that is described in section 4.2.2.

4.2.1 Setup for the measurement of the detuning: *setup "A"*

Let's first describe the *setup "A"*, which is depicted in Fig 4.5. In this configu-

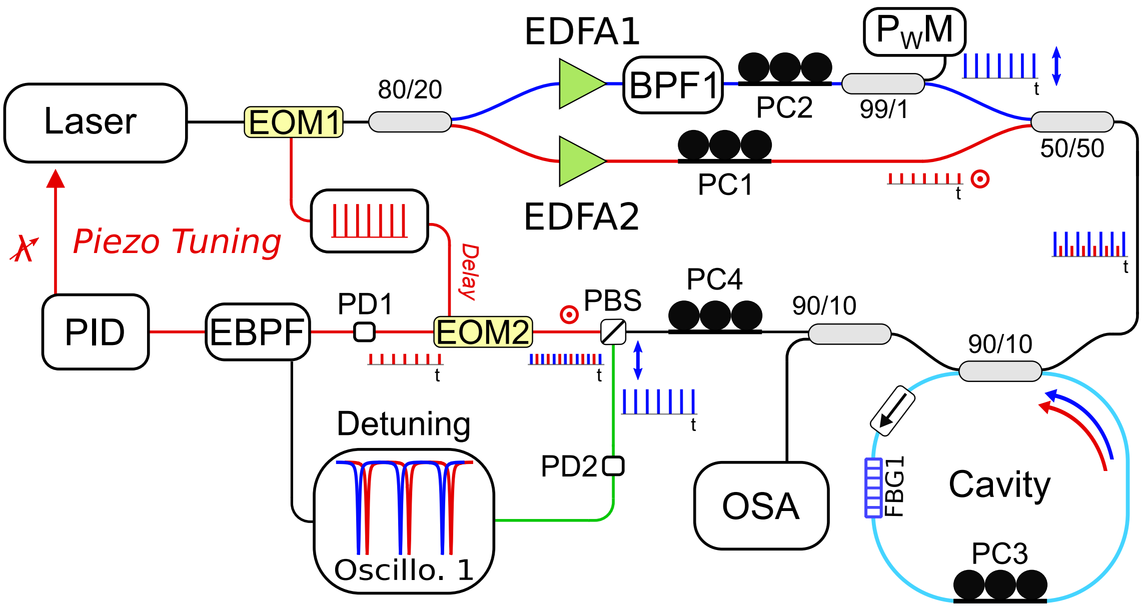

Figure 4.5: Experimental setup, *"Setup A"*. EOM$_1$, electro-optical modulator; PC$_{1-4}$, polarization controller; PD$_{1-2}$, photodetector; OSA, optical spectrum analyzer; EDFA$_{1-2}$, erbium-doped fiber amplifier; BPF$_1$, band-pass filter; EBPF, electronic band-pass filter; Oscillo. $_1$, oscilloscope; PID, proportional-integrate-derivate controller; FBG$_1$, fiber Bragg grating; P$_W$M, powermeter; PBS, polarization beam splitter; ⊙ ↕, polarization states.

ration the weak reference signal from the 90% output port of the coupler is isolated from the strong one in two steps. First, by using a polarization beam splitter (PBS), and then with an EOM (EOM2) that is synchronized with EOM1. Note that we added a polarization controller just before the PBS (PC4) to ensure that the reference and strong fields match the polarization axes labeled ⊙ and ↕ in Fig. 4.5, respectively. Finally, the reference field experiences an isolation of more than 60 dB from the strong one. This signal is then detected by a photodetector (PD1) and filtered through an electronic band-pass filter (EBPF) to sample its envelope, which is used as a reference signal by a PID to stabilize the system (by finely tuning the pump wavelength). This configuration has been used to record all the spectra shown in the following and particularly to determinate the comb repetition rate.

4.2.2 Setup for temporal recording with improved stability: *setup "B"*

We recall that an optical frequency comb consists of a series of phase-locked equally spaced laser frequency lines. The previous configuration allows to determine

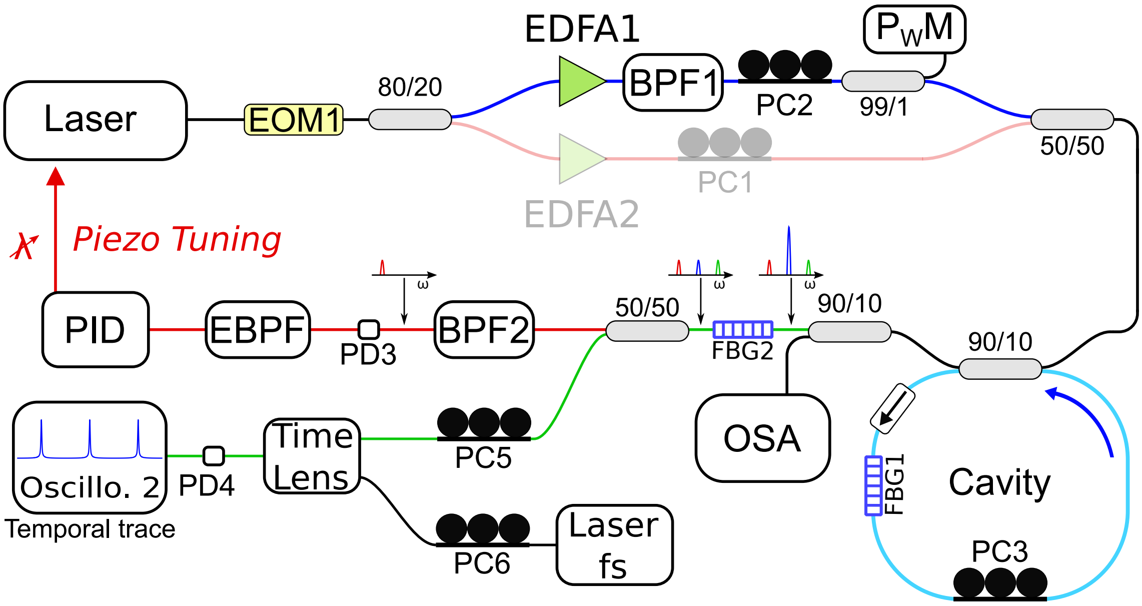

Figure 4.6: Experimental setup, *"Setup B"*. EOM$_1$, electro-optical modulator; PC$_{1-2,5-6}$, polarization controller; PD$_{3-4}$, photodetector; OSA, optical spectrum analyzer; EDFA$_{1-2}$, erbium-doped fiber amplifier; BPF$_{1-2}$, band-pass filter; EBPF, electronic band-pass filter; Laser fs, femtosecond laser; Oscillo. $_2$, oscilloscope; PID, proportional-integrate-derivate controller; FBG$_{1-2}$, fiber Bragg grating; P$_W$M, powermeter.

the repetition rate (teeth spacing) of the comb, but it gives no information about the phase locking between the lines. Different complex experimental measurements can be performed to characterize this phase locking [166], however for the sake of simplicity we focused on the temporal traces, which provide a very good insight into the spectral lines' coherence. From the theory and the parameters of our cavity, we expected to generate frequency comb whose repetition rate lies on the ps scale, well above the bandpass of our detection system (Oscillo. 1 and PD2 in Fig.

4.5). In order to solve this problem, we modified our experimental setup to implement at the cavity output a time-lens system (Picoluz ultrafast temporal magnifier, Thorlabs [102]) connected to a fast photodiode (PD4) and a high band-pass oscilloscope (Oscillo. 2, 70 GHz bandpass each). This new configuration (*setup "B"*), depicted in Fig. 4.6, allows to magnify the bandpass of our detection system about 57 times, providing a temporal resolution of 300 fs over 50 ps. The time-lens effect is obtained via FWM process between the signal to analyze and a (linearly chirped) pump provided by an ultra-fast laser (Laser fs, repetition rate: 100 MHz). We added polarization controllers on the pump and signal path (PC5-6), since FWM process is very sensitive to the relative polarization between these two beams. The fiber Bragg grating (FBG2) added before the time-lens on the signal path and used in transmission allows to diminish the power of the central component. Given the importance of the cw component with respect to the harmonics, this filtering is necessary, in order to record the temporal pattern. Note that, it does not require to synchronize the time-lens pump with the repetition rate of the cavity like in the previous chapter since we do not aim to performing round-trip to round-trip measurements. We analyze cavity output traces when the system achieves a stationary regime by recording a large set of data and by selecting those for which time-lens pump pulses and signal pulses temporally overlaps. In order to record clean temporal traces from the time-lens, an excellent stabilization is required. The stabilization provided by the *"setup A"* is not good enough for such recording. That is why in the *"setup B"* we developed a more efficient stabilization system. Rather than using a reference signal co-propagating with the pump inside the cavity for the feedback loop system, we maximized the power of one of the parametric bands generated as in Ref. [55]. For this purpose we sampled a part of the FBG2 (filter the central component) output signal thanks to 50/50 coupler, then filtered (BPF2, 1 nm bandpass at FWHM) to isolate a parametric sideband. This field is then detected by a photodetector (PD3) and used as a power error signal by a feedback loop system (PID) to stabilize the cavity. Note that we obtained a better stabilization from this new system but it does not provide a detuning measure.

4.3 Experimental results

We investigated experimentally the regime identified by the red dot in Fig. 4.2(a) by using the *"setup A"*. We set the total cavity detuning measured in experiments to zero ($\delta = \delta_0 - \arg\left[H\left(0\right)\right] = 0$) and we increased the input power until $P_{in} = 6.6$ W ($P = 2.2$ W) above the instability threshold. We observe, from the experimental output cavity spectrum displayed by red line in Fig. 4.7(a), that a pair of sidebands located at ±588 GHz arises with amplitudes of approximately 26 dB below the pump power. Moreover, an harmonic frequency comb that consists of more that 10 lines is generated through subsequent FWM process between the pump and these sidebands triggered by GTF process. Note that the maximum efficiency of GTF process does not arise at the position of the maximum loss of the filter (see blue curve in Fig. 4.7 that depicts the modulus squared of the FBG transfer function) as expected from a purely dissipative filter ($H(\Omega) = |H(\Omega)|$). Indeed, as we mentioned the causality imposes through Kramer-Kronig relation, that the spectral response function of the filter contains a phase term $\psi(\Omega)$. It modifies the position of the perfect phase-matching. Consequently, this sidebands, rather than being located at the frequency most attenuated by the filter (399 GHz), they arise on the high frequency edge of the filter at 588 GHz. These results are in excellent agreement with theoretical predictions from Eq. (4.21) that predicts bands located at ±580 GHz. We compared this recording to the cavity output spectrum obtained from numerical integration of the full Ikeda map equations (Eq. (4.1) and Eqs. (4.5-4.6)) by using the SGF. This spectrum is depicted in Fig. 4.7(b) with a red line. Green dotted line stands for the square modulus of the SGF transfer function. We obtain a good agreement between both spectra where sidebands of the numerical spectrum are located really close to the experimental one at ±590 GHz. It even reproduces the spectrum asymmetry coming from the dispersion slope (contribution of third-order dispersion from both fiber and filter) that has already been reported in [113,114]. We underline that in the peculiar case we have investigated (monostable regime, normal dispersion region) without the filter inside the cavity, the cw solutions are modulationally stable (see Fig. 1.6(a) in chapter 1) and consequently, the observed GTF sidebands cannot be confused with standard MI sidebands.

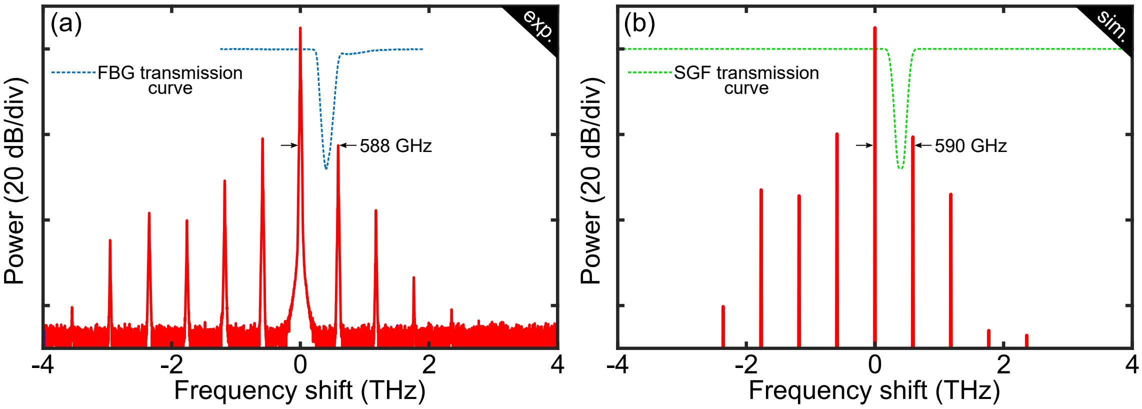

Figure 4.7: Cavity output spectrum for $\lambda_{pump} = 1544.66$ nm from (a) experiments an (b) numerical simulations. The blue dashed line in (a) and green dashed line in (b) correspond to the square modulus of the FBG transfer function and the square modulus of the SGF transfer function ($|H(\Omega)|^2$), respectively.

Then, we investigated the tunability of the GTF process. For this purpose we kept the central frequency of the filter unchanged and we tuned the pump wavelength from $\lambda_{pump} = 1544.06$ nm to 1545.18 nm. This leads to a frequency shift between the pump and the position of the maximum loss of the filter from 323 GHz to 464 GHz. The recorded cavity output spectra are depicted in Fig. 4.8(a), where the central components correspond to the pump. We note that the position of the first anti-Stokes sidebands triggered by the GTF process remains located at the same position $\lambda_{A-S} = 1539.93$ nm ($f_{A-S} = 194.679$ THz), set by the filter position (see blue dotted curve in Fig. 4.8, $\lambda_{FBG} = 1541.50$ nm, $f_{FBG} = 194.482$ THz). Through FWM process between the pump and this first anti-Stokes sideband, a Stokes sideband is symmetrically generated on the other side of the pump. For the sake of clarity, we do not show other bands of the combs since it is not required to determine the comb repetition rate. However, we stress that all spectra, whose three main components are depicted in Fig. 4.8(a), are really similar to the one shown in Fig. 4.7(a) corresponding to $\lambda_{pump} = 1544.06$ nm (bold red curve in Fig. 4.8(a)). In Fig. 4.8(b) we show the measured repetition rate versus the frequency shift between the pump and the filter with colored dots. These results are in excellent agreement with theoretical predictions from the linear stability analysis (Eq. (4.11)), from which the position of the most unstable band is depicted by a blue line. Note that the comb repetition rate is different from the frequency shift between the pump and filter since the maximum of GTF process occurs at a frequency shifted from the maximum loss frequency of the filter on the anti-Stokes side. Consequently, by tuning the frequency shift between the pump and the filter from 323 GHz to 464 GHz, we can tune the comb repetition rate quite linearly from 533 GHz to 653 GHz in this peculiar case. The comb repetition rate could eventually be tuned over a wider range however the tunability of the laser used in experiments to pump the cavity was limited to the range investigated here preventing us to observe such combs.

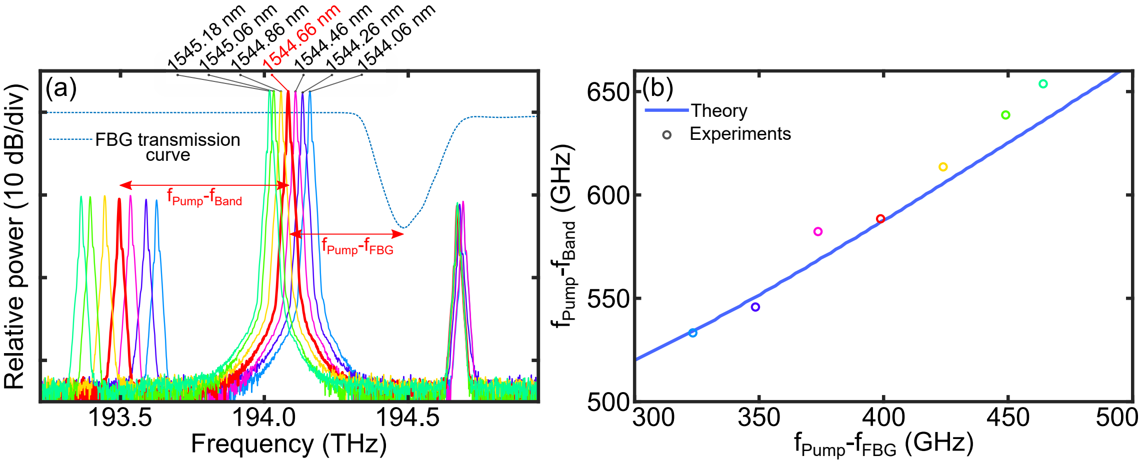

Figure 4.8: (a) Cavity output spectrum recorded for different pump wavelengths (from 1544.06 nm to 1545.18 nm). The blue dashed line corresponds to the square modulus of the FBG transfer function. (b) Measured repetition rate as a function of the pump to FBG frequency shift (dots). The red dot stands for the cavity output spectrum depicted in red in (a) and in Fig. 4.7(a). The blue line corresponds to the position of the most unstable frequency calculated from Eq. (4.11).

Finally, we investigated the phase locking of the comb lines. This has been performed by using the *"setup B"* to record the temporal traces thanks to a time-lens system when the system achieves a stationary regime. Fig. 4.9(a) shows an example of recorded temporal traces. For the sake of simplicity, we normalized the trace such as its maximum and its minimum correspond to 1 and 0, respectively. We observe temporal periodic structures with a period of ≈ 1.7 ps that corresponds almost to 1/(588 GHz). These results are in good agreement with the corresponding numerical simulation depicted on Fig. 4.9(b), which shows temporal structures whose period is also equal to 1.7 ps. The localized temporal periodic structures we observe in the time domain confirm that the comb lines are indeed locked. To go further, we recorded the temporal trace several times with a time lapse of several seconds between two recordings. We obtained every time the same periodic pattern with the same periodicity of 1.7 ps, which demonstrated the stability of the generated structures.

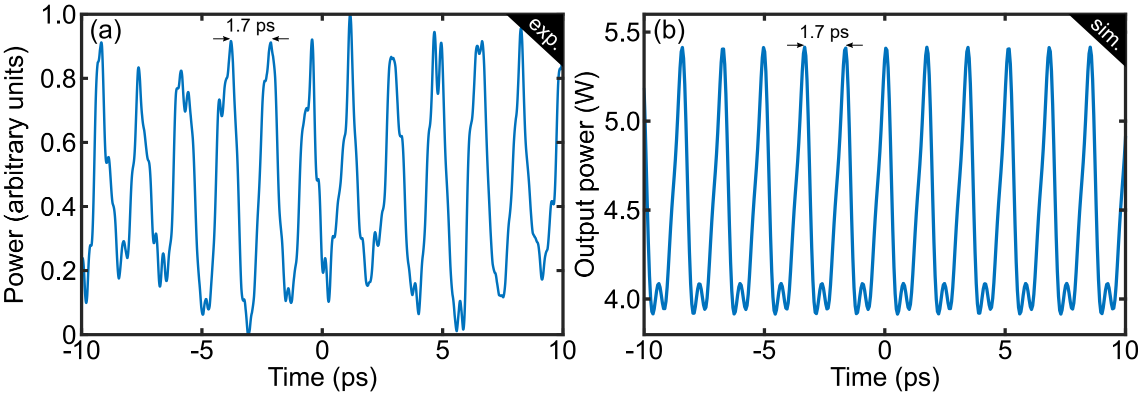

Figure 4.9: (a) Temporal trace recorded from the cavity output signal. (b) Temporal trace from the corresponding numerical simulation. Note that in experiments we used a filter to attenuate the pump component before sending to the time-lens, this explain the arbitrary units on the y-axis of Fig. (a).

Summary

By implementing a FBG whose amplitude profile was a quasi super-gaussian shape in a passive fiber cavity that operates in normal dispersion regimes, we were able to generate an OFC that consists of more than 10 thin lines through GTF mechanism. Moreover, we demonstrated that the repetition rate can be tuned quasi linearly between 323 GHz and 424 GHz by simply adjusting the pump-filter frequency detuning without requiring additional devices [167, 168]. The small number of comb lines observed in experiments is due to the low finesse of the cavity ($\mathcal{F} = 12$). However, such process in microresonators where the cavity confinement is really high would improve strongly the efficiency of GTF process and consequently, would provide broader OFCs. Our fundamental results give a proof of concept of OFC generation through GTF process and highlight the flexibility of this process. Indeed, it does not require any dispersion management contrary to other tunable

OFCs in Kerr resonators [58, 158] and can even arise in normal dispersion regimes. In addition, at variance with OFCs generated through dark and bright cavity solitons, which require the cavity to operate in bistable regimes, GTF process can arise in monostable regimes requiring less input power. These results open the way for really promising future applications in particular for OFC generation in the visible part of the spectrum, where the material dispersion is normal.

Chapter 5

Phase-sensitivity of seeded modulation instability in passive resonators: phase and power real-time characterization

Contents

Modulation instability in passive cavities has been mostly studied in the case of a monochromatic pumping (cw or quasi-cw pump), where the MI process is initiated from noise [51–53]. Few studies investigate MI in passive cavities for a polychromatic driving of the system. We note a theoretical study of the nonlinear stage of MI for dual pumping in Ref. [169] and experimental studies of primary parametric seeding of Kerr OFC in microresonators [170–172], dual pumping of Kerr OFC [173] and seeded MI [174]. However, none of these studies focus on the sensitivity of the intra-cavity field dynamics to the phase of the input components, which is expected, due to the parametric nature of the MI process. We found only one study that investigated in the case of a tri-chromatic pump (same amplitude of the three spectral components) the phase-sensitivity of the parametric process, but it focuses on the first harmonics and on FWM and not on MI [175]. In this chapter, we investigate the phase-sensitivity of MI in passive cavities driven by a pump weakly modulated which, to our knowledge, has never be done. Thus, in the spectral domain, the electrical field consists in three components: a strong central one that corresponds to the carrier frequency, and two weak symmetric sidebands that we used to seed the MI process at the most unstable frequencies. In this work, we investigate the phase-sensitivity of the sidebands. For this purpose, we first led in section 5.1, theoretical investigations based on an extension of the LLE and an appropriate three wave truncation. We highlight that the gain of the sidebands vanishes for peculiar phases of the input components. In a second step, we built an experimental setup in collaboration with Corentin Naveau, in order to observe and validate our theoretical predictions. This setup implements an heterodyne measurement technique inspired from Ref. [176], which allows to record the power dynamics round-trip to round-trip of the intra-cavity pump and sidebands components. Experimental results are reported in section 5.3. Note that the heterodyne technique implemented in our setup allows to record the phase dynamics of each components. However, at the time of writing, the numerical process to record the phase is still under development. Nevertheless, we present preliminary results of this phase recordings, that provide first physical insights of the sidebands and pump phase dynamics.

5.1 Modeling of seeded MI process

5.1.1 Lugiato-Lefever Equation with a modulated pump

To model passive cavities driven by a modulated pump, we follow the procedure described in Refs. [169, 177] by applying a mean field approximation of the finite-dimensional map Eqs. (1.8-1.9). This leads to the following extended version of the LLE:

$$\frac{\partial E(z,t)}{\partial z} = \left(-\frac{\alpha}{L} - i\frac{\delta_0}{L} - \beta_1\frac{\partial}{\partial t} - i\frac{\beta_2}{2}\frac{\partial^2}{\partial t^2} + i\gamma|E(z,t)|\right) E(z,t) + \frac{\tilde{\theta}}{L}E_{in}(t) \quad (5.1)$$

where t is the time in the laboratory reference frame and β_1 the first order dispersion term. The modulated input field is time-dependent and is given by:

$$E_{in} = E_{in,0} + \left(\sigma_i e^{i\Omega t} + \sigma_s e^{-i\Omega t}\right) \tag{5.2}$$

where $E_{in,0} = \sqrt{P_{in}} e^{i\phi_{0,in}}$ is the electric field of the carrier wave and $\sigma_i = \sqrt{S_i} e^{i\phi_{i,in}}$ and $\sigma_s = \sqrt{S_s} e^{i\phi_{s,in}}$ are the electric fields of the sidebands (seeds) at respectively the angular frequencies $^+/_-\Omega$. P_{in}, $P_{i,in}$,$P_{s,in}$ and $\phi_{0,in}$, $\phi_{i,in}$, $\phi_{s,in}$ denote the pump, idler, and signal input power and input phase, respectively. We point out that we do not use a reference frame moving at the group velocity of the pump by making the transformation $\tau = t - \beta_1 z$ as it is done to obtain standard LLE (to remove the β_1 term). Indeed, this transformation is not relevant because the pump is time dependent, which consequently, does not allow to eliminate the β_1 term from the equation.

5.1.2 Three wave model

In the following, we analyze seeded MI in the case of weak seeds relative to the pump ($P_{in} \gg P_{i/s,in}$). For this purpose, we expand the electric field circulating within the cavity ($E\left(z,t\right)$ in Eq. (5.1)) in Fourier modes $E_n \exp\left(in\Omega t\right)$ where n is the number of the considered mode. Then, we assume that the dynamics of the system is contained in the three main modes ($n = 0, \pm 1$) of the electric field, the pump and its first contiguous sidebands such as:

$$E(z,\Omega) = E_0(z,\Omega) + E_i(z,\Omega)e^{i\Omega t} + E_s(z,\Omega)e^{-i\Omega t} \tag{5.3}$$

The parameters $E_0 = \sqrt{P_0(z,\Omega)} e^{i\varphi_0(z,\Omega)}$, $E_i = \sqrt{P_i(z,\Omega)} e^{i\varphi_i(z,\Omega)}$, and $E_s = \sqrt{P_s(z,\Omega)} e^{i\varphi_s(z,\Omega)}$ are the pump, idler, and signal components of the intra-cavity field, respectively. $P_{0,i,s}$ denote the pump, idler and signal power and $\phi_{0,i,s}$ their phase, respectively. Then, by introducing this Ansatz (Eq. (5.3)) into the extended LLE (Eq. (5.1)) and by equating terms oscillating at the same frequency, we obtain the following three wave model (TWM):

$$\frac{\partial E_0}{\partial z} = \left(-\frac{\alpha}{L} - i\frac{\delta_0}{L}\right) E_0 + i\gamma\left(|E_0|^2 + 2|E_i|^2 + 2|E_s|^2\right) E_0 + 2i\gamma E_i E_s E_0^* + \frac{\tilde{\theta}}{L} E_{in,0} \tag{5.4}$$

$$\frac{\partial E_i}{\partial z} = \left(-\frac{\alpha}{L} - \frac{i}{L}\delta_i + i\frac{\beta_2}{2}\Omega^2\right) E_i + i\gamma\left[\left(2|E_0|^2 + |E_i|^2 + |E_s|^2\right) E_i + E_0^2 E_s^*\right] + \frac{\tilde{\theta}}{L}\sigma_i \tag{5.5}$$

$$\frac{\partial E_s}{\partial z} = \left(-\frac{\alpha}{L} - \frac{i}{L}\delta_s + i\frac{\beta_2}{2}\Omega^2\right) E_s + i\gamma\left[\left(2|E_0|^2 + 2|E_i|^2 + |E_s|^2\right) E_s + E_0^2 E_i^*\right] + \frac{\tilde{\theta}}{L}\sigma_s \tag{5.6}$$

The parameters $\delta_i = \delta_0 - 2l\pi + \beta_1\Omega L$ and $\delta_s = \delta_0 + 2l\pi - \beta_1\Omega L$ with $l = \arg\left[\min_l |\delta_0 + 2l\pi - \beta_1\Omega L|\right]$ define the cavity detuning of the idler and signal components from their closest resonances which implies $\delta_{i/s} \in [-\pi, \pi]$.

In order to justify the exactness of our treatment and the accuracy of Eqs. (5.4-5.6), we report an example in Fig. 5.1(a)-(b). We seed the MI at the most unstable frequencies $\Omega_T = \pm\sqrt{2\left(\delta_0/L - 2\gamma P\right)/\beta_2}$ ($P = \tilde{\theta}^2 P_{in}/\left[\left(\delta_0 - \gamma LP\right)^2 + (\alpha)^2\right]$, see chapter 1), just above the MI cavity threshold $P_{th} > \alpha/\left(\gamma L\right)$, from an initially empty (only noise) cavity. From an experimental point of view, this is the easiest way to generate seeded MI. For the sake of simplicity, we seed the system such as the cavity detunings $\delta_0 = \delta_s = \delta_i$ ($\beta_1\Omega_T L = 2k\pi$, $k \in \mathbb{Z}$). We show the signal, pump and idler power and phase evolutions calculated from the TWM (by using an ordinary differential equation (ODE) solver) in Fig. 5.1(a)-(b), respectively, for an arbitrarily set value of $\phi_{i,in} - \phi_{0,in} = \pi/3$ and $\phi_{s,in} - \phi_{0,in} = -\pi/2$. The dashed red, green and blue curves in Fig. 5.1(a) account for the idler (P_i), signal (P_s) and pump (P_0) power evolutions, respectively, whereas in Fig. 5.1(b) they account for the idler (φ_i), signal (φ_s), and pump (φ_0) phase evolutions, respectively. We observe that the power of the pump increases quickly and reaches a stationary regime after 25 round-trips, while the power of the idler and signal increases slowly and reaches a stationary regime after more than 150 round-trips. In the same way, the pump phase evolves quickly and reaches the stationary state 0.2π, whereas idler and signal phase reach the stationary states -0.1π and -0.9π, respectively, after more than 150 round-trips. We compared these results to corresponding numerical simulations of the extended LLE (Eq. (5.1)). The dotted red, green and blue curves in Fig. 5.1(a) account for the idler, signal and pump power evolutions, respectively, and in Fig. 5.1(b) they account for the idler, signal, and pump phase evolutions, respectively. We can see that the TWM accurately reproduces the power and phase evolutions predicted by the extended LLE. Note that we just observe small discrepancies for the final idler and signal stationary regime powers(< 1 dB). The reason for this, is that the TWM (Eq. (5.4-5.6)) only takes into account the contribution of the three main modes ($n = 0, \pm1$, pump and sidebands, respectively) and neglects the weak contribution of other modes (in numerical simulations of the extended LLE, amplitudes of modes $n = \pm2, \pm3, ...$ (harmonics) are more than 16 dB below that of modes $n = \pm1$). We numerically checked that we obtain similar agreement with other input phase values, which confirms that the truncated TWM (Eqs. (5.4-5.6)) can be used to accurately study the dynamics of seeded MI.

In Fig. 5.1(c)-(d), we report a second example obtained for the same parameters as the first example, except that we modified the phase of the input components such as $\phi_{i,in} - \phi_{0,in} = -\pi/6$ and $\phi_{s,in} - \phi_{0,in} = -\pi$. In this second example, the idler and signal components reach a stationary regime after only 25 round-trips. Moreover, their final stationary regime is modified. In particular, their power reaches a higher level compared to the first example ($\approx +5$ dB). These observations suggest that the energy-transfer between the pump and sidebands is sensitive to the relative phase between the input components. In the following, we investigate the phase-sensitivity

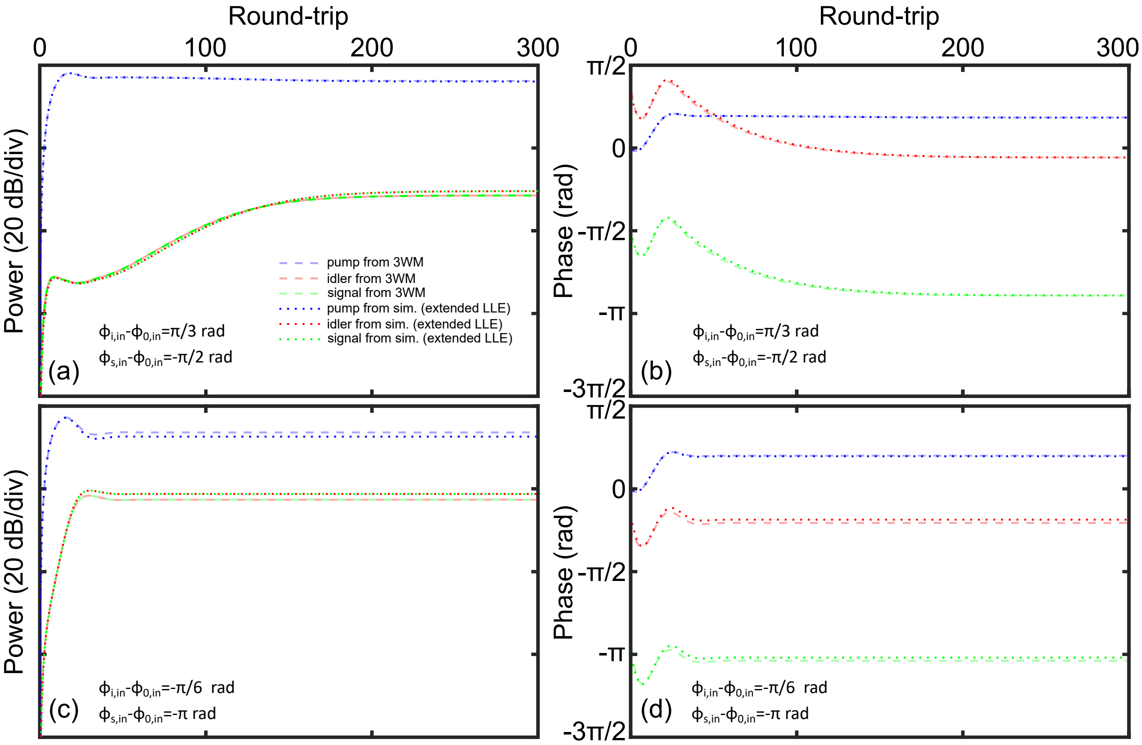

Figure 5.1: (a) Power and (b) phase evolutions of idler, signal and pump fields versus the round-trip number. Dotted lines stand for numerical simulations of the extended LLE (Eq. (5.1)) and dashed lines for solutions of the TWM (Eqs. (5.4-5.6)). Parameters: $\delta_0 = \delta_i = \delta_s = 0.05$ rad, $\alpha = 0.14$, $L = 169$ m, $\gamma = 1.2$ $\mathrm{W}^{-1}.\mathrm{km}^{-1}$, $P_{in} = 0.2$ W, (a)-(b) ((c)-(d)) $\phi_{i,in} - \phi_{0,in} = \pi/3$ $(-\pi/6)$ rad and $\phi_{s,in} - \phi_{0,in} = -\pi/2$ $(-\pi)$ rad, $\beta_2 = -20$ $\mathrm{ps}^2.\mathrm{km}^{-1}$, $S_{i/s} = 1.10^{-2} \times P_{in}$ (20 dB), $\theta = \sqrt{0.1}$, $f_T = \pm 59$ GHz.

of the transient and stationary regimes of seeded MI, regarding the relative phase of the input components. The stationary regime is investigated in the following section, while the transient regime is investigated in section 5.1.2.2.

5.1.2.1 Phase-sensitivity of the stationary regimes of seeded MI

The stationary regimes correspond to stable steady-states of the extended LLE (Eq. (5.1)). In general, Eq. (5.1) does not have simple analytical solutions, and one has to resort to numerical simulations. However, under certain conditions, approximate solutions providing a good physical insight can be easily found from the truncated TWM (Eqs. (5.4-5.6)). These solutions are calculated in two steps, following the method used to find the stationary regimes of standard MI in the chapter 7 of Ref. [178]. This development can be summarized as follows. First, we assume that the sidebands and seeds amplitudes are equal. Consequently, the model (Eq. (5.4-5.6)) becomes a system of two coupled ordinary differential equations.

Then, we solve these equations when $\partial_z = 0$ and we express the solutions (steady-states) and input field components by their polar form $E_0 = \sqrt{Q}e^{i\varphi'_0}$, $E_s = E_i = \sqrt{U}e^{i\varphi'_s}$[1], $E_{in,0} = \sqrt{P_{in}}e^{i\phi_{0,in}}$, $\sigma_s = \sigma_i = \sqrt{S}e^{i\phi_{s,in}}$ $(S = S_i = S_s)$. We then obtained the following set of four equations at the most unstable frequency Ω_T:

$$\gamma\left(2U\cos\left(\Delta\psi\right) + Q + 4U\right) - \frac{\delta}{L} = -\frac{\sqrt{Pin}\sin\left(\Delta\psi_0\right)\widetilde{\theta}}{L\sqrt{Q}} \tag{5.7}$$

$$2\gamma U\sin\left(\Delta\psi\right) + \frac{\alpha}{L} = \frac{\sqrt{Pin}\cos\left(\Delta\psi_0\right)\widetilde{\theta}}{L\sqrt{Q}} \tag{5.8}$$

$$\gamma\left(Q\cos\left(\Delta\psi\right) + 2Q + 3U\right) = -\frac{\sqrt{S}\sin\left(\Delta\psi_s\right)\widetilde{\theta}}{\sqrt{U}L} + \frac{\delta_0}{L} - \frac{\beta_2}{2}\Omega_T^2 \tag{5.9}$$

$$-\gamma Q\sin\left(\Delta\psi\right) + \frac{\alpha}{L} = \frac{\sqrt{S}\cos\left(\Delta\psi_s\right)\widetilde{\theta}}{\sqrt{U}L} \tag{5.10}$$

We here introduced $\Delta\psi = 2\left(\varphi'_s - \varphi'_0\right)$, that measures the phase difference between the intra-cavity sidebands and pump. In the same way, we define $\Delta\psi_0 = \phi_{0,in} - \varphi'_0$ that characterizes the phase difference between the input and the intra-cavity pump, and $\Delta\psi_s = \phi_{s,in} - \varphi'_s$, which is the phase difference between the input seeds and the intra-cavity sidebands. We can calculate Q, U, φ'_0 and φ'_s by solving the above equations by using a numerical approach (e.g. nonlinear system solver), and consequently express the steady-state solutions E_0 and $E_{s/i}$. Finally, the linear stability of these solutions is obtained by calculating the eigenvalues of the Jacobian matrix of Eqs. (5.7-5.10) and of their complex conjugates. Thus, stable steady-states solutions E_0 and E_s correspond to the stationary regimes of the pump and signal fields. In order to give a physical insight of the phase-sensitivity of the stationary regimes, we solve the system of Eqs. (5.7-5.10) for different values of relative input phases $\phi_{i,in} - \phi_{0,in} = \phi_{s,in} - \phi_{0,in} = \Delta\xi$, by finding the stable and unstable steady-states. We depicted in Fig. 5.2(a) the calculated solutions in the polar coordinate system $(P_{i/s},\ \varphi_{s/i} - \varphi_0)$. The solid colored lines correspond to the the stable steady-state points (stationary regimes), and dashed colored lines to the unstable steady-state points [2] . Each case of $\Delta\xi$ can be identified by a color indexed in the legend of Fig. 5.2. We observe that by changing $\Delta\xi$ the steady-states form an “aircraft propeller” in the phase plane. Steady-states that belong to the “blades” are stable (stationary regimes, solid lines) and the others close to the “rotor” are unstable (see the zoom on the initial stage in Fig. 5.2(b), dashed lines). We superimposed some examples of trajectories calculated from the TWM (by using an ODE solver) for $\Delta\xi$ ranging from 0 to 2π and depicted with colored dotted lines. We note that their final states marked with colored dots match perfectly with the predicted stable steady-states. Finally, we compared these results to corresponding numerical simulations of the extended LLE (Eq. (5.1)). They are depicted in Fig. 5.2(c) through their trajectories in the phase plane $(P_{i/s},\ \varphi_{s/i} - \varphi_0)$. As predicted by our analysis, the

---

[1] φ'_0, φ'_i, and φ'_0 correspond to steady-states of φ_0, φ_i, and φ_0 calculated from the TWM

[2] These lines have been obtained by fitting the solutions Eqs. (5.7-5.10) calculated for 16000 different values of $\Delta\xi$ ranging from 0 to 2π

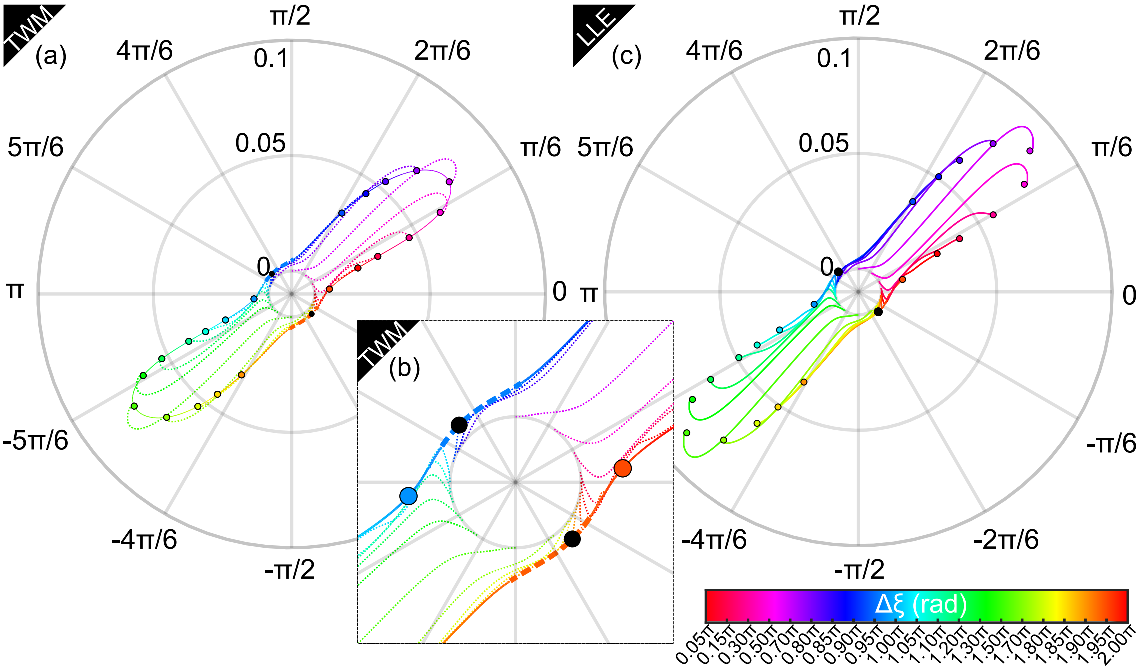

Figure 5.2: (a) Position of the steady-states predicted from numerical analysis of the truncated TWM Eqs. (5.4-5.6) in the phase plane ($P_{i/s}$, $\varphi_{s/i} - \varphi_0$). Solid colored lines stand for the stable states and dashed lines for unstable states. Dotted curves correspond to some examples of trajectories for $\Delta\xi$ ranging from 0 to 2π. (b) Zoom on the initial stage of Fig. 5.2(a). (c) Example of trajectories calculated from numerical simulations of the extended LLE (Eq. (5.1)). In all cases, colored dots stand for the final states of the calculated trajectories and black dots to the predicted saddle points (Eqs. (5.21-5.22)).

system converges toward attractors (marked by colored dots), whose position is in good qualitative agreement with theoretical predictions depicted in Fig. 5.2(a) by the solid lines. Note that both numerical simulations of the extended LLE and TWM show that the trajectories bifurcate either to one blade or to the other "blade" of the "propeller" in the transient regime, depending on the phase of the input component. The change in the bifurcation happened close to two points that we identify by black dots in Fig. 5.2(a-c). In the following section, we investigate this phase-sensitivity of the transient regime. In particular, we identify the origin and the nature of these observed bifurcations.

5.1.2.2 Phase-sensitivity of the transient regime of seeded MI

In this section, we focus on the transient dynamics of seeded MI and identify the origin of its phase-sensitivity to input conditions. In order to give an analytical description of this regime, we derived a simplified version of the TWM. This derivation is obtained by noting that in the transient regime $P_0 \gg P_{i/s}$ (see Fig. 5.1(a)-(c)).

Consequently, we can derive the following simplified version of the truncated TWM Eqs. (5.4-5.6), by linearizing in signal and sidebands fields:

$$\frac{\partial E_0}{\partial z} = \left(-\frac{\alpha}{L} - i\frac{\delta_0}{L}\right) E_0 + i\gamma |E_0|^2 E_0 + \frac{\tilde{\theta}}{L} E_{in,0} \tag{5.11}$$

$$\frac{\partial E_i}{\partial z} = \left(-\frac{\alpha}{L} - \frac{i}{L}\delta_i + i\frac{\beta_2}{2}\Omega^2\right) E_i + i\gamma \left[2|E_0|^2 E_i + E_0^2 E_s^*\right] + \frac{\tilde{\theta}}{L}\sigma_i \tag{5.12}$$

$$\frac{\partial E_s}{\partial z} = \left(-\frac{\alpha}{L} - \frac{i}{L}\delta_s + i\frac{\beta_2}{2}\Omega^2\right) E_s + i\gamma \left[2|E_0|^2 E_s + E_0^2 E_i^*\right] + \frac{\tilde{\theta}}{L}\sigma_s \tag{5.13}$$

We justify the exactness of our treatment and the validity of Eqs. (5.11-5.13), by reporting the same two examples used to validate the TWM. In these examples, depicted in Fig. 5.3, we compared the pump and idler power and phase evolutions predicted by this simplified model to numerical simulations of the extended LLE. The signal and pump power and phase evolutions of the first (second) example are

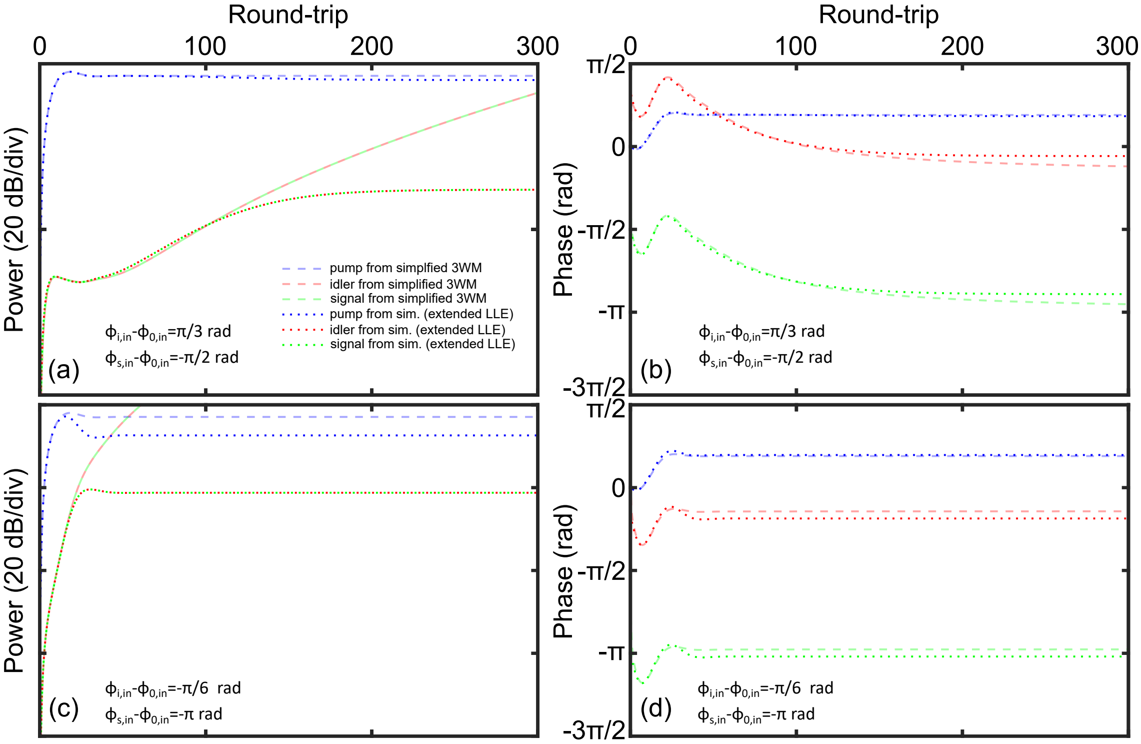

Figure 5.3: (a) and (b) Power and phase evolutions of idler, signal and pump fields versus the round-trip number, respectively. Dotted lines stand for numerical simulations of the extended LLE (Eq. (5.1)) and dashed lines for solutions of Eqs. (5.11-5.13). Blue, red, and green correspond to the pump, signal and idler, respectively. Parameters: $\delta_0 = \delta_i = \delta_s = 0.05$ rad, $\alpha = 0.14$, $L = 169$ m, $\gamma = 1.2$ $\mathrm{W}^{-1}.\mathrm{km}^{-1}$, $P_{in} = 0.2$ W, (a)-(b) ((c)-(d)) $\phi_{i,in} - \phi_{0,in} = \pi/3$ $(-\pi/6)$ rad and $\phi_{s,in} - \phi_{0,in} = -\pi/2$ $(-\pi)$ rad, $\beta_2 = -20$ $\mathrm{ps}^2.\mathrm{km}^{-1}$, $S_{i/s} = 1.10^{-2} \times P_{in}$ (20 dB), $\theta = \sqrt{0.1}$, $f_T = \pm 59$ GHz.

depicted in Fig. 5.3(a) and (b) (Fig. 5.3(c) and (d)), respectively. The red, green and blue curves in Fig. 5.3(a) and (c) account for the idler, signal and pump power evolutions, respectively, and in Fig. 5.3(b) and (d) to the idler, signal, and pump phase evolutions, respectively. Dotted lines corresponds to numerical simulations of the extended LLE and dashed lines to solutions of the simplified TWM calculated with an ODE solver. We observe that the solutions of the simplified TWM when $P_{i/s}$ are 20 dB below P_0, accurately reproduce the transient dynamics of seeded MI predicted by numerical simulations of the extended LLE (Eq. (5.1)). Thus, it confirms that the simplified TWM (Eqs. (5.11-5.13)) can be used to describe the transient regime of seeded MI. By using this model, we can determine the input phase conditions for which the gain is minimum. This is performed by finding the analytical solutions of the simplified TWM (Eqs. (5.11-5.13)). For this purpose, we assume that the intra-cavity pump is initially in a steady-state ($E_0 = \overline{E}_0$). It allows to simplify the system of three coupled differential equations (5.11-5.13) into an algebraic equation ($\partial_z \overline{E}_0 = 0$ for Eq. (5.11)) and two coupled differential equations (Eqs. (5.12-5.13)). Then, as we did in our analysis of the stationary regimes, we focus our investigation on (i) the most unstable frequencies (Ω_T), (ii) cases where $\delta_0 = \delta_i = \delta_s$ ($\beta_1 \Omega_T L = 0 \quad [2\pi]$), and additionally (iii) monostable regimes ($\delta_0/\alpha < \sqrt{3}$). Consequently, we find from Eq. (5.11) ($\partial_z = 0$) that:

$$\overline{E}_0 = \sqrt{P} e^{i\phi_0} = \frac{i\widetilde{\theta}\sqrt{P_{in}} e^{i\phi_{0,in}}}{\gamma L P - \delta_0 + i\alpha} \tag{5.14}$$

where P and ϕ_0 are the power and the phase of the steady-state pump, and from Eqs. (5.12-5.13) that:

$$\begin{bmatrix} E_i(z,\Omega_T) \\ E_s^*(z,\Omega_T) \end{bmatrix} = C_1 \exp(\lambda_+ z) \overbrace{\begin{bmatrix} 1 \\ \frac{-iP}{\overline{E}_0^2} \end{bmatrix}}^{v_{\lambda_+}} + C_2 \exp(\lambda_- z) \overbrace{\begin{bmatrix} 1 \\ \frac{+iP}{\overline{E}_0^2} \end{bmatrix}}^{v_{\lambda_-}} + \begin{bmatrix} \overline{E}_i \\ \overline{E}_s^* \end{bmatrix} \tag{5.15}$$

$$\lambda_\pm = -\frac{\alpha}{L} \pm \gamma P \tag{5.16}$$

where $\lambda_\pm$ and $v_{\lambda\pm}$ correspond to the eigenvalues and eigenvectors of the system of the coupled differential equations (Eqs. (5.12-5.13)), respectively. The last term in Eq. (5.15) correspond to the steady-state solutions of Eqs. (5.12-5.13) ($\partial_z = 0$), and are defined by:

$$\overline{E}_{i/s} = \sqrt{F} e^{i\phi_{i/s}} = \frac{\widetilde{\theta}\sqrt{S} e^{i\phi_{i,in/s,in}} \left[\alpha + i\gamma L P e^{-i\Delta\eta}\right]}{\alpha^2 - \gamma^2 L^2 P^2} \tag{5.17}$$

where $\Delta\eta = \phi_{s,in} + \phi_{i,in} - 2\phi_0$. The parameters F and $\phi_{i/s}$ denote the power and the phase of the steady-state idler and signal, respectively. C_1 and C_2 are constants that can be determinated from the initial conditions (at $z = 0$). For an initially empty cavity $E_{i/s}(z = 0, \Omega_T) = \widetilde{\theta}\sigma_{i/s} = \widetilde{\theta}\sqrt{S} e^{i\phi_{i/s,in}}$. Substituting the left term of

Eq. (5.15) by these initial condition and by solving this system we find that:

$$C_1 = \frac{-i}{2}\left[\theta\sqrt{S}e^{i(2\phi_0-\phi_{s,in})}\left(e^{i\left(\frac{\pi}{2}+\Delta\eta\right)}-1\right)-\sqrt{F}e^{i(2\phi_0-\phi_s)}\left(e^{i\left(\frac{\pi}{2}+\phi_s+\phi_i-2\phi_0\right)}-1\right)\right] \tag{5.18}$$

$$C_2 = \frac{-i}{2}\left[\theta\sqrt{S}e^{i(2\phi_0-\phi_{s,in})}\left(e^{i\left(\frac{\pi}{2}+\Delta\eta\right)}+1\right)-\sqrt{F}e^{i(2\phi_0-\phi_s)}\left(e^{i\left(\frac{\pi}{2}+\phi_s+\phi_i-2\phi_0\right)}+1\right)\right] \tag{5.19}$$

By analyzing these solutions, we note that above the MI cavity threshold $P > \alpha/(\gamma L)$, the eigenvalues $\lambda_\pm$ of the system (Eq. (5.15)) are always real and of opposite signs. Thus, the solutions $E_{i/s}$ grow exponentially and decay exponentially following the direction v_{λ_+} and v_{λ_-}, respectively. The crossing of these two lines that satisfy $C_1 = C_2 = 0$ correspond to a saddle point [179]. To get a deeper physical insight of the dynamics of the system, we provide a schematic example in Fig. 5.4 of the idler and signal field evolutions in the coordinate system defined by the axes (v_{λ_+};v_{λ_-}) (green and red axis, respectively). For the sake of simplicity, we consider that C_1 and C_2 are real, such as we can plot the evolution of the system in two-dimensions. In this representation, we describe the evolution of the system for different initial conditions depicted by black dots, whose coordinates correspond to C_1 (on v_{λ_+} axis) and C_2 (on v_{λ_-} axis). These evolutions are represented by black curves in Fig. 5.4. The positive exponential term is dominant in Eq. (5.15) for large value of z. Consequently, all solutions that are depicted by black curves in Fig. 5.4 tends asymptotically to the line defines by the eigenvector v_{λ_+}. Depending on the sign of C_1 (v_{λ_+} coordinate of the initial condition), they tend either to positive coordinates or to negative coordinates along the v_{λ_+} axis. In the peculiar case where the initial state belongs to the v_{λ_-} axis ($C_2 = 0$), for example the green dot in Fig. 5.4, the system evolves asymptotically toward a saddle point identified by a red dot in Fig. 5.4. Note that in this case, the system does not experiment gain since the term that contains the "positive" exponential is equal to zero.

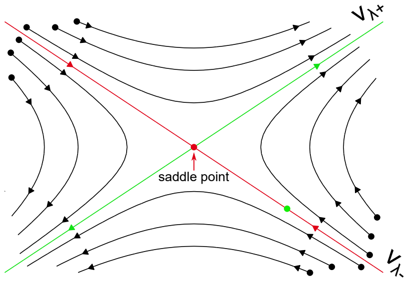

Figure 5.4: Saddle point. Black and red dots stand for the initial states and the saddle point respectively. $v_{\lambda_\pm}$ correspond to the eigenvectors of the system and the red and green axes define their direction, respectively.

By looking again at Fig. 5.2 that depicts the dynamics of MI in the phase plane ($P_{i/s}$, $\varphi_{s/i} - \varphi_0$), we observe the same kind of behavior of the different trajectories, and the black dots we previously identified should correspond at first sight to saddle points. In the following, we check this hypothesis by calculating the coordinates of these saddle points from Eq. (5.15) for which the system does not experiment gain. This can be performed by analyzing the constants C_1(Eq. (5.18)) and C_2 (Eq. (5.19)) that define the <u>initial</u> coordinates in the $\left(v_{\lambda_+}; v_{\lambda_-}\right)$ base. For $C_1 = 0$ (term with the positive exponential in Eq. (5.15)), for instance the green dot in Fig. 5.4 the system converge toward the saddle point. Thus, the solutions $E_{i/s}$ of Eq. (5.15) that corresponds to a saddle point are obtained for $C_1 = 0$ and $z \to +\infty$. The latter condition (C_1=0) implies in the case where $S \neq 0$ that on the saddle point the following relation are satisfied (see Appendix B):

$$\Delta\eta = \phi_{s,in} + \phi_{i,in} - 2\phi_0 = -\frac{\pi}{2}\ [2\pi] \tag{5.20}$$

$$\boxed{\phi_s + \phi_i - 2\phi_0 = -\frac{\pi}{2}\ [2\pi]} \tag{5.21}$$

Equation (5.21) provides the phase coordinates of the saddle points. The power of the saddle points are found by substituting in the square modulus of Eq. (5.17) the parameter $\Delta\eta$ by Eq. (5.20) such as:

$$\boxed{F_{saddle\,point} = \frac{\theta^2 S}{L^2\left(\dfrac{\alpha}{L} + \gamma P\right)^2}} \tag{5.22}$$

In the case depicted in Fig. 5.2, where we assume that the idler and signal field were equal ($\phi_s = \phi_i$), we find from Eqs. (5.21-5.22) that the coordinates of the saddle points in the phase plane ($P_{i/s}$, $\varphi_{s/i} - \varphi_0$) are ($2.2 \times 10^{-3}$ W,$-\pi/4$ rad) and (2.2×10^{-3} W,$3\pi/4$ rad). These coordinates correspond exactly to the black dots identified in Fig. 5.2 and confirm that the observed bifurcations derive from saddle points. Finally, from Eq. (5.20) ($\Delta\eta$) and Eq. (5.14) (steady-state of the pump $\overline{E}_0$), we can express, the relation between the phase of the input components for which the system tend asymptotically towards a saddle point and does not experiment gain (see Appendix B):

$$\boxed{\phi_{i,in} + \phi_{s,in} - 2\phi_{0,in} = 2\arctan\left(\frac{-\alpha}{\gamma LP - \delta_0}\right) + \frac{\pi}{2}\ [2\pi]} \tag{5.23}$$

This condition depends on the overall losses over a cavity round-trip, which are fixed by the cavity design, on the detuning (δ_0), and on the intra-cavity pump power (P) that can be tuned in experiments. In order to check that a minimum of gain is observed for the phase condition Eq. (5.23), we plot the signal (or idler) power as a function of $\Delta\xi = \phi_{s,in} - \phi_{0,in} = \phi_{i,in} - \phi_{0,in}$, for different propagation lengths. Indeed, the signal (idler) power $|E_s|^2$ ($|E_i|^2$) diverges except in the case where $C_1 = 0$,

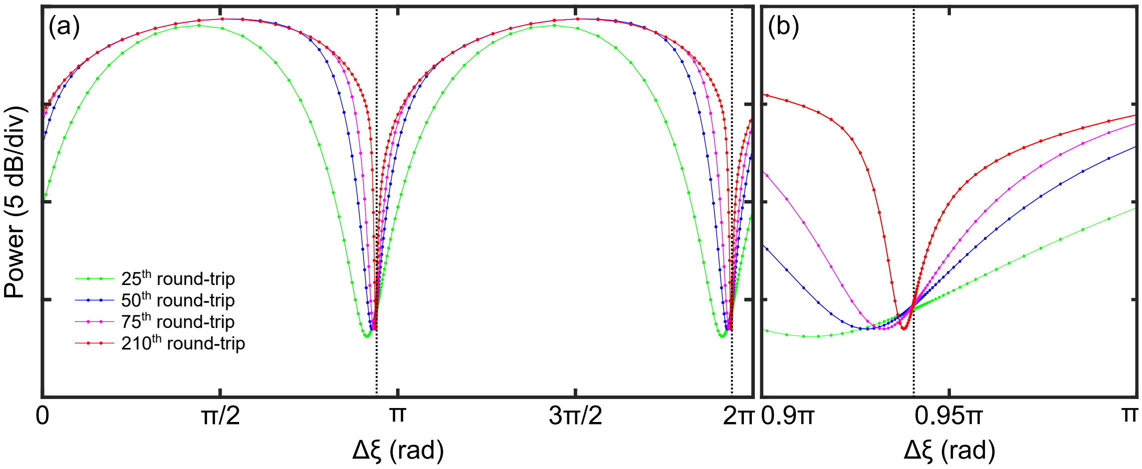

Figure 5.5: (a) Signal power at $n = 25, 50, 75$ and 210 round-trips versus $\Delta\xi = \phi_{s,in} - \phi_{0,in} = \phi_{i,in} - \phi_{0,in}$ obtained of numerical simulations from the extended LLE, Eq. (5.1) (green,blue, magenta and red curves, respectively). Each dot corresponds to a numerical simulation and the black dotted lines stand for the theoretical predictions from Eq. (5.23). (b) Zoom on the first minima. Parameters: $\delta_0 = 0.05$ rad, $\alpha = 0.14$, $L = 169$ m, $\gamma = 1.2$ W^{-1}.km^{-1}, $P_{in} = 0.2$ W, $\beta_2 = -20$ ps^2.km^{-1}, $S_{i/s} = 1.10^{-2} \times P_{in}$, $\theta = \sqrt{0.1}$, $f_T = \pm 59$ GHz.

where the system evolves toward a saddle point. Thus, the signal (idler) power versus $\Delta\xi$ corresponds to a function with two minima that according to Eq. (5.23) are located at $\Delta\xi = \arctan\left(-\alpha/\left(\gamma LP - \delta_0\right)\right) + \pi/4\ [\pi]$. To plot this function, we performed numerical simulations of the extended LLE (Eq. (5.1)) from an initially empty cavity. We set $\Delta\xi = \phi_{s,in} - \phi_{0,in} = \phi_{i,in} - \phi_{0,in}$ such as the left term of Eq. (5.23) is equal to $2\Delta\xi$ and we performed numerical simulations for 200 values of $\Delta\xi$ ranging from 0 to 2π. When $2\Delta\xi$ comes close to the value of the right term of Eq. (5.23) (saddle point) we expect that the transient regime of idler/signal components becomes longer (lower gain). Consequently, by recording the idler/signal power at a given round-trip n versus $\Delta\xi$, the minima of the obtained function should correspond to the input phase condition required to “reach” the saddle point. Fig. 5.5(a) illustrates this function for $n =$ 25, 50, 75 and 210 round-trips, with green, blue, magenta and red curves, respectively (each dot corresponds to a numerical simulation). We observe that these functions are π-periodic with two minima as expected from Eq. (5.23). The position of these minima are in really good agreement with theoretical predictions from Eq. (5.23) marked by black dotted lines in Fig. 5.5(a)-(b). Note that by looking at the zoom on the first minima (see Fig. 5.5(b)), we observe that when n increases: (i) the width of the function decreases and (ii) the position of the minima tends towards the theoretical predictions. The disagreement of the minima positions of the function obtained for $n =$ 25, 50, 75 and 210 round-trips with theoretical predictions is about 0.092, 0.039, 0.025 and 0.008 rad, respectively. These small discrepancies originate from two facts. First, in numerical simulations we assume an empty cavity as initial condition, whereas analytically it was necessary to assume that it is filled by the pump value corresponding to the stationary regime ($E_0 = \overline{E}_0$, Eq. (5.14)). Second, the minima calculated from the theory (Eq. (5.23)) are obtained for $z \to +\infty$.

5.2 Experimental setup: cavity implementation in a heterodyne measurement setup

To investigate the dynamics of seeded MI in passive fiber cavities, we built in collaboration with Corentin Naveau, the experimental setup depicted in Fig. 5.6. The studied cavity is made of a standard single mode fiber ($\beta_2^{SMF} = -20$ ps^2.km^{-1}

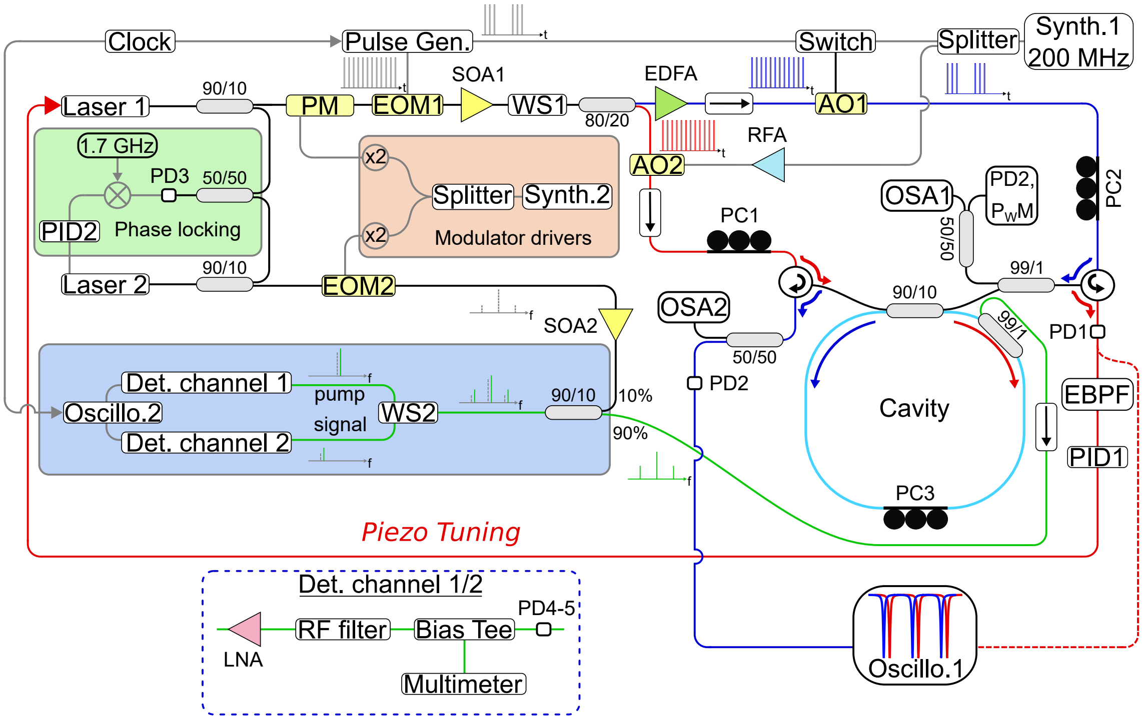

Figure 5.6: Experimental setup. Laser 1, cw laser implied in the to stabilize and pump the cavity. Laser 2, cw laser implied to produce the local oscillators. EOM$_{1-2}$, electro-optical modulator; PM, phase modulator. AO$_{1-2}$, acousto-optic modulator; WS$_{1-2}$, Waveshaper; P$_W$M, powermeter; PC$_{1-4}$, polarization controller; PD$_{1-5}$, photodetector; OSA$_{1-2}$, optical spectrum analyzer; EDFA, erbium-doped fiber amplifier; SOA$_{1-2}$, semiconductor optical amplifier; LNA, low noise radio-frequency amplifier; RF filter, radio-frequency filter; EBPF: electronic band-pass filter; Oscillo.$_{1-2}$, oscilloscope; PID$_{1-2}$, proportional-integrate-derivative controller; Pulse Gen., pulse generator; Synth.$_{1-2}$, synthesizer; RFA, radio-frequency amplifier.

at 1554 nm, and $\gamma^{SMF} = 1.2$ W^{-1}.km^{-1}) closed by a 90/10 coupler that allows to pump the system. We added a 99/1 coupler placed just before the 90/10 coupler to extract and analyze directly a small fraction of the intra-cavity field. To avoid parametric instabilities that might arise in dispersion managed cavities [96,98], both couplers are made of the same fiber that constitutes the cavity, in order to get a perfectly uniform cavity with a total length of 169.8 m.

5.2.1 Input field generation and cavity detuning stabilization

In order to pump and stabilize the cavity, we use a continuous wave from laser 1 (Fig. 5.6) centered at 1554 nm and passing through a phase modulator (PM) to generate two symmetric sidebands around the central wave. Then, an electro-optical modulator (EOM1) supplied by a pulse generator chops the wave to produce a train of 10 ns square shaped pulses (to avoid SBS as in previous experiments), whose repetition rate matches that of the cavity. Finally, this field is amplified by a semiconductor optical amplifier (SOA1) and tailored by a programmable optical filter (Waveshaper, WS1), providing a fine control of the relative phase ($\phi_{s,in} - \phi_{0,in}$ and $\phi_{i,in} - \phi_{0,in}$) and intensity of the sidebands with respect to the carrier wave (pump). A 80/20 coupler placed just after the WS1 allows to divide the signal in two lines.

The first line identified by blue color allows to produce the pump field by amplifying the WS1 output signal with an EDFA then chopped by an acousto-optic modulator (AO1). This AO1 is supplied by a radio frequency (RF) signal of $f_{AO} = 200$ MHz that can be switched on/off thanks to an RF switch. This AO1 has two main functions. First, it can produce bursts of 210 pulses to trigger the MI process. Each burst is separated by the equivalent in time of 120 pulses from the next (see Fig. 5.7(a)). This ratio of 210/120 pulses between these two-levels pump patterns both ensures to observe the birth of MI until a stationary state is reached, and to perfectly empty the cavity before the next burst. Second, it increases the extinction ratio of pulses up to 50 dB such as the power of the weak continuous background does no trigger the SBS effect (see Fig. 5.7(b)). These bursts are injected through the right port of the cavity and propagate in the anti-clockwise direction. We assume that the phase variation between the input field components induced by the dispersion during the propagation between the WS1 and the cavity input ($L_p \approx 10$ m of SMF-28 mainly) is not significant. We checked it, for frequency spacing between pump and seeds of the order of $f_T = 60$ GHz (typical value in our following experiments), this phase variation ($\Delta\phi = 2\pi^2\beta_2^{SMF} f_T^2 L_p$) is less than 1.2×10^{-2} rad. Note that we also added a 99/1 coupler just before the input port of the cavity in order to check the input field characteristics: spectrum, temporal profile, and power thanks to an OSA, a photodetector, and a powermeter, respectively.

The second line identified by red lines produces the reference field used to stabilize the cavity against external perturbations. As in previous chapters, thanks

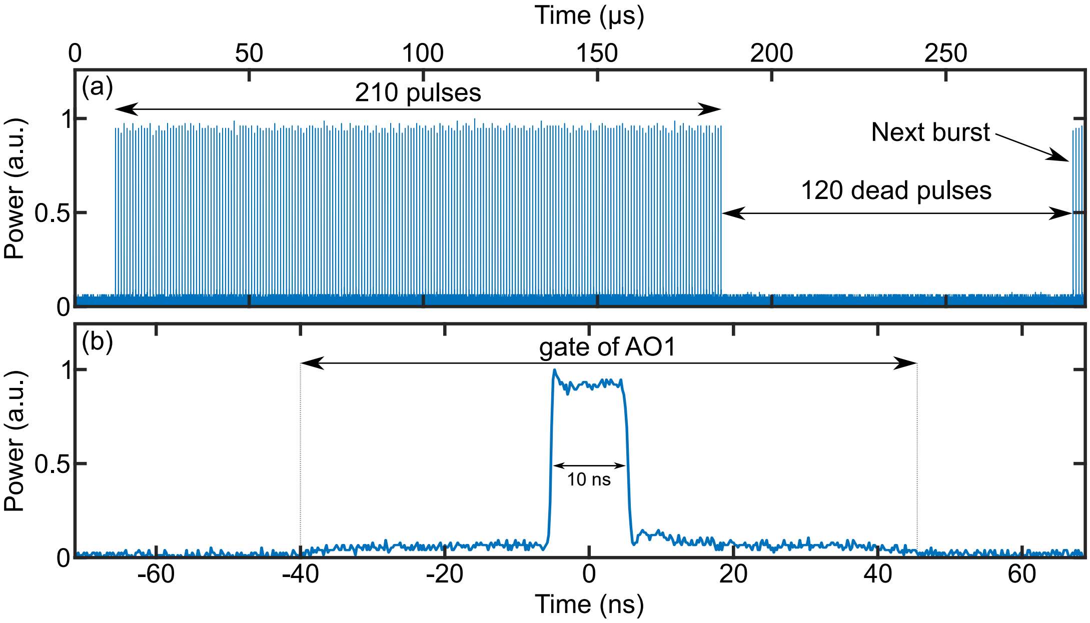

Figure 5.7: (a) Experimental cavity input burst of 210 pulses and 120 dead pulses. (b) Zoom on a pulse.

to two circulators placed at each output of the cavity and polarization controllers (PC_{1-3}), we can use independently both propagation directions of the cavity. As usual, while the pump field propagates in the anti-clockwise direction on a polarization eigenstate, the reference field propagates in the clockwise direction, on the other polarization eigenstate. The latter one is then detected from the right cavity output with a photodetector (PD1), and filtered by the electronic band pass filter (EBPF) to obtain the pulse train envelope. The feedback loop system is ensured by the PID1 by using this field envelope as a reference to finely tune the wavelength of laser 1 and to stabilize the linear phase of the system. Note that, even if this reference field contains sidebands (idler and signal) in addition to the pump wave, these ones are really weak relatively to the pump ($\approx$ 20 dB below the pump power). They are not detected and thus do not affect the cavity stabilization. The detuning is measured thanks to an oscilloscope (Oscillo. 1) by recording both cavity outputs, when the cavity operates in the linear regime and by disabling the burst mode on the pump field. Note that the pump beam suffers a frequency shift induced by AO1 of $f_{AO} = 200$ MHz implying an additional linear phase difference between the pump field and reference field when we stabilize the cavity. That means that the measured detuning δ_0 from experiments by using the same method explained in section 1.5.2 does not correspond to the real detuning. Indeed, it incorporates a second term depending on f_{AO}. For the sake of simplicity and set easily the detuning to the right expected value, we added a second acousto-optic modulator (AO2) on the reference beam line, supplied by the same carrier wave than AO1. In this way, the pump and reference fields suffer now the same frequency shift of 200 MHz, removing this inconvenient additional linear phase difference.

5.2.2 Recording system, detection line

The detection line identified by green fibers allows to analyze a small fraction of the intra-cavity field, extracted thanks to a 99/1 coupler placed just before the coupler that closed the cavity. This one is then mixed via a 90/10 coupler with a local oscillator (heterodyne signal) phase locked on laser 1 and detuned from its frequency by $\Delta f = 1.7$ GHz to perform a coherent heterodyne detection. Note that because of the 200 MHz shift induced later by the AO1 on laser 1, the beating frequency between the local oscillator and the extracted intra-cavity signal is at 1.5 GHz and not at 1.7 GHz. Thus, it provides about 15 periods of heterodyne beating over one pulse of 10 ns.

The phase locking of the local oscillator provided by the cw laser 2 (see Fig. 5.6) with respect to laser 1 is ensured following the procedure described in Ref. [180]. A part of laser 1 and 2 emissions (extracted with 90/10 couplers) are combined with a 50/50 coupler, and their beating is detected with a photodiode (PD3). This detected signal is used as a reference signal for a feedback loop system by mixing it with a stable RF signal at 1.7 GHz. As soon as this beating deviates from this setpoint (1.7 GHz), the retro-action loop system based on a PID (PID2) adjusts the wavelength of the slave laser 2. Consequently, the slave laser 2 follows the wavelength fluctuations of the master laser 1. Obviously, this stabilization requires a fast control of the master laser 2 wavelength, which is performed by a high bandwidth PID (100 MHz). As we plan to perform heterodyne measurements not only on the pump components but also on the signal and idler components, the phase-locked field from laser 2 is modulated by an EOM (EOM2) to generate sidebands spaced by 54 GHz. Thus, it provides for each components of interest its own local oscillator. Note that the RF signal driving the EOM2 is delivered by the same source (Synth. 1) than the PM. signal. This ensures a fixed phase relation between them.

The beating between the components of interest (pump and signal waves) and their respective local oscillator (see small spectra in Fig. 5.6) are selected thanks to a highly selective programmable filter (WS2). They are then sent to the photodetectors of detection channels 1 and 2 (details on the inset in Fig. 5.6), respectively. The intensities at the output of the photodetector include a DC (direct current) signal that is filtered out by using a bias-tees and RF filters. Time-dependant signals are then amplified by passing through a low noise amplifier (LNA), recorded by an oscilloscope (Oscillo. 2) and demodulated with a short time Fast-Fourier Transform (FFT). Finally, further numerical treatments of the recorded data following a similar method that the one used in Ref. [176] allow to retrieve the power and phase evolutions. These numerical treatments were performed by Corentin Naveau. Note that because of the optical path length difference between the two detection lines, the relative phase between pump and sidebands we measure corresponds to $\varphi_s - \varphi_0$ up to an additive constant. This constant can be determined indirectly as we will show it in section 5.3.2.

5.3 Experimental results

In order to observe the phase-sensitivity properties of seeded MI and in particular, to observe saddle points, we set the system in the same configuration investigated in sections 5.1.2.1-5.1.2.2 (see caption of Fig. 5.5). We set the detuning to $\delta_0 = 0.05$ rad, we increased the input power until $P_{in} = 0.2$ W just above the MI cavity threshold and we switched off the seeds via the WS1. Consequently, the MI is triggered by the noise and we can determine the position of the most unstable frequencies from the cavity output spectrum (see Fig. 5.8(a)). In our case, we find that $f_T = \Omega_T/(2\pi) = \pm 54$ GHz, which is in good agreement with theoretical predictions (see section 5.1.2, $f_T = \pm 59$ GHz). Then, we set the frequency of the seeds at these values and we switched on their power such as the seeds power is 20 dB below the input pump power. Additionally, for the sake of simplicity, we set the detuning of the seeds such as $\delta_i = \delta_s = \delta_0$ (following the method described in Appendix C), and the relative phase between signal/idler and pump input fields to $\phi_{i,in} - \phi_{0,in} = \phi_{s,in} - \phi_{0,in} = \Delta\xi$. An example of intra-cavity spectrum in the case of seeded MI is depicted in Fig. 5.8(b). We observe two narrow symmetrical sidebands located at $f_T = \pm 54$ GHz, whose peaks power is about 7 dB below the pump power. Thus, it confirms that the system perfectly triggers the MI at the most unstable frequencies since sidebands experience a gain of approximately 13 dB. Note that when we switch from MI triggered by noise to seeded MI, we observe strong amplification of the harmonics located at ±108 GHz (see Fig. 5.8(a)-(b)).

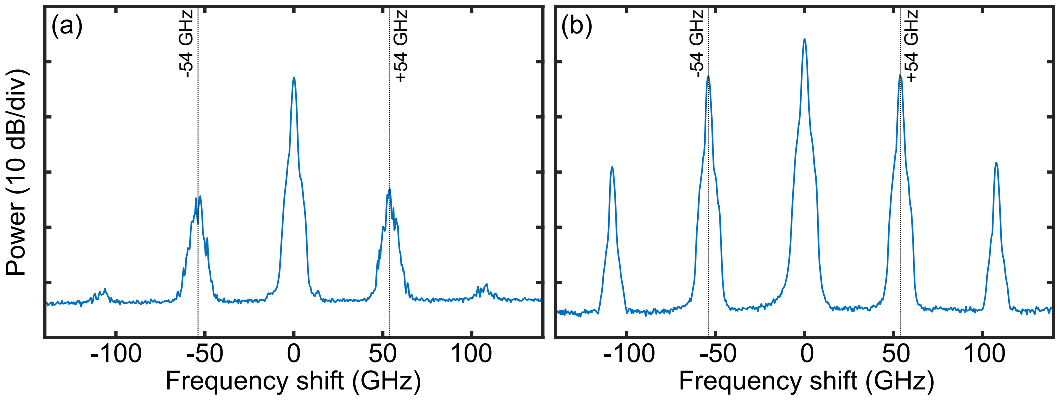

Figure 5.8: (a) Output cavity spectrum from seeded noise MI. Sidebands are located at ±54 GHz. (b) Example of intra-cavity spectrum from seeded MI at ±54 GHz.

Next, we recorded the signal/pump power and signal/pump phase over 16 consecutive bursts for a given value of $\Delta\xi$. We report an example of such recordings in Fig. 5.9 for $\Delta\xi = 0.7\pi$ rad. Fig. 5.9(a-c) depicts raw data obtained for each burst (gray curves) for the pump and signal power and for the relative phase evolution, respectively. From these results, we observe that in the transient regime, the measures have very weak fluctuations, whereas in the stationary regime they become larger. In order to reduce this measurement uncertainty, we performed an averaging of the raw data of the 16 consecutive recorded bursts. These averages are depicted in Fig. 5.9(a-c) by solid purple curves, whereas the additional dashed purple curves delimit the confidence intervals of the average curves for a confidence level of 95%. In this example, the maximum width of the confidence intervals is 0.11 W, and 0.032 W (±10% and ±12% of the mean value of the stationary regime) for the pump and seed power, respectively, and is 0.06π for the relative phase.[3].

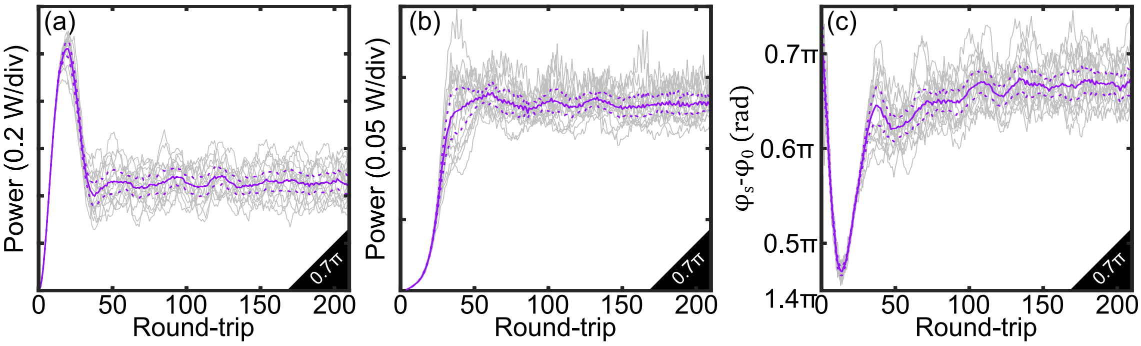

Figure 5.9: (a)-(b) Evolution of the pump and signal power, respectively for $\Delta\xi = 0.7\pi$ rad. (c) Evolution of the relative phase between signal and pump. The gray curves stand for raw data. The solid violet curves correspond to the average of raw data and the dashed violet curves delimit the confidence interval of the averages (confidence level of 95%).

Finally, we performed the same recordings for 20 other different initial phase values ($\Delta\xi$) from 0 to 2π. The power evolutions are depicted in Fig. 5.10(a) and in Fig. 5.16 (Appendix C) and their relative phase in Fig. 5.11(a). Each case of $\Delta\xi$ investigated is associated to a color identified in the legend of Fig. 5.10 and Fig. 5.11.

5.3.1 Power evolution

We looked at the pump and signal power evolutions in Fig. 5.10(a) for $\Delta\xi \in [0;\pi]$. In almost all cases, we observe that the pump power increases quickly and reaches a maximum at about 20 round-trips. Then, it decreases to reach a stationary regime after a certain round-trip number depending of $\Delta\xi$. By looking at the signal power evolutions in Fig. 5.10(a), we observe that whatever the input phases, the

---

[3] The confidence intervals are determined from the experimental standard deviation of the mean that is defined at the round-trip n by $s\left(n\right) = \sqrt{\frac{1}{N(N-1)}\sum_{j=1}^{N}\left(x_j(n) - \bar{x}(n)\right)}$. $\{x_1\left(n\right), ..., x_N\left(n\right)\}$ and $\bar{x}(n)$ are the observed values and the mean value of these observations at the round-trip n, respectively, whereas $N = 16$ is the number of observations. The confidence interval by using t-Student distribution is defined by $[\bar{x}(n) - ts\left(n\right); \bar{x}(n) + ts\left(n\right)]$ at the round-trip n. The factor t is obtained by using t-Student distribution table. In our case $t = 2.131$ for an confidence level of 95% and $N = 16$.

signal power follows always the same evolution during the first fifteen round-trips. Beyond, the signal power evolves toward a stationary regime with a growth rate that depends on the input phases. For some cases, we even observe that the signal power first decreases of a few decibel (< 4 dB) beyond the 15^{th} round-trip and finally increases before the 30^{th} round-trip. Thus, the transient regime is phase-sensitive. For the extreme cases, the signal power for $\Delta\xi = 0.95\pi$ rad reaches a stationary regime after about 100 round-trips (see curves labeled *"slow critical case"*), whereas for $\Delta\xi = 0.7\pi$ the stationary regime is achieved after only 40 round-trips (see curves labeled *"fast critical case"*). We compared these results with the corresponding

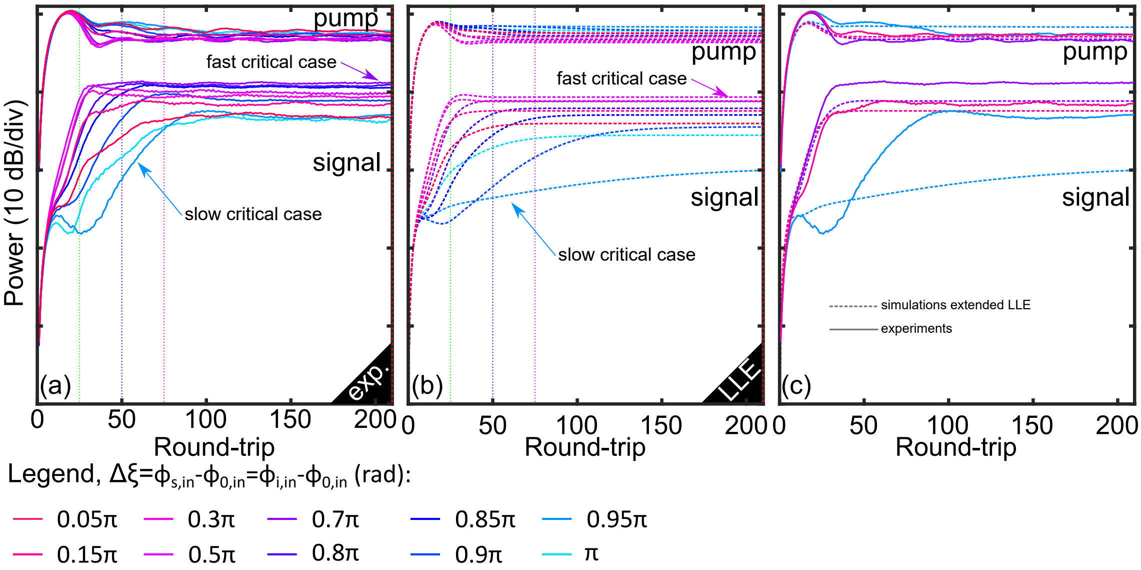

Figure 5.10: Signal and intra-cavity pump power versus round-trip number for different values of $\Delta\xi$ between 0 and π. (a) stand for experimental results, (b) for numerical simulations of the extended LLE (Eq. (5.1)). (c) Comparison of the pump and signal evolutions from experiments and numerical simulations for $\Delta\xi = 0.15\pi$, 0.7π, 0.95π rad in (c).

numerical simulations of the extended LLE (Eq. (5.6), see Fig. 5.10 (b)). We observe that the MI dynamics is qualitatively similar to the one observed in experiments. Nevertheless, we note discrepancies. For the sake of clarity and highlight them, we superimpose in Fig. 5.10(c) experimental recordings and numerical simulations for the three following cases: $\Delta\xi = 0.15$, 0.7π and 0.95π rad (the pink, violet and blue curves, respectively). The solid curves stand for the experiments and the dashed curved for the numerical simulations. From this figure, we first discern that the amplitude variation of the pump power seems to be less important in numerical simulations than in experiments. Second, the signal power of the stationary regime observe in experiments is shifted down of approximately 4 dB relative to stationary regimes of numerical simulations. The reason for such shift should results from small imperfections during the calibration between the detection channels 1 and 2 (see Fig. 5.6) to determine the relative power level between the pump and signal. We also note some differences for cases with long transient regimes (curves labeled *"slow critical cases"*). The transient regime in numerical analysis is significantly longer than in experiments. The reason for this behavior is that for these cases, the system is pumped near the v_{λ_-} axis, which leads the system to converge toward a saddle point. In numerical simulations, at this perfect value, we should stay "indefinitely" in the transient regime, but in experiments this cannot be observed since random noise, external perturbations, etc., quickly force the system to jump from this saddle point which is an unstable equilibrium to a stationary regime. Note that for the sake of clarity, we did not show the pump and signal power evolution for $\Delta\xi \in [\pi; 2\pi]$ since their behavior is $\pi-$periodic. This has been verified experimentally and recordings are depicted in (Appendix C).

5.3.2 Physical insight of the phase evolution: preliminary results

We looked at the relative phase between the pump and signal, that provides a first physical insight of the phase dynamics. These experimental measurements correspond to $\varphi_s - \varphi_0$ up to an additive constant as mentioned in section 5.2.2. In order to determine this constant, we assume that the phase variation between signal and pump components after the first cavity round-trip is not significant. We checked it from numerical simulations of the extended LLE (Eq. (5.1)), and we note that this phase variation is always below 0.13 rad. Thus, we find that the relative phase between pump and signal at the first round-trip corresponds to the relative phase between input components ($\varphi_s - \varphi_0 \approx \phi_{s,in} - \phi_{0,in}$). These measurements with this phase correction are depicted in Fig. 5.11(a). As previously observed for the power evolution, the transient regime of the phase depends on $\Delta\xi$. For the cases labeled "slow critical cases", the system reaches a stationary regime after about 100 round-trips, while the stationary regimes is achieved after only 40 round-trips in cases labeled "fast critical cases". Before we complete our investigation, we would like to draw attention on the phase recordings of the "slow critical cases". They are depicted in Fig. 5.12 for $\Delta\xi = 0.95\pi$ (blue dotted curve in Fig. 5.11(a)) in a similar way that Fig. 5.9(c). Fig. 5.12 depicts in gray curves raw data of the relative phase evolution obtained for each burst. The averages of the data are represented by solid blue curves in these figures, whereas the additional dashed purple curves delimite the confidence intervals of the average curves for a confidence level of 95%. In this "slow critical cases", we can see that the first round-trips are well described by the averaging (maximum width of the interval of confidence is 0.1π rad). However, beyond the 25^{th} round-trip, the phase tends toward two different stationary regimes ($\varphi_s - \varphi_0 = 0.5\pi$ or $\varphi_s - \varphi_0 = 2.5\pi$). Consequently, performing an averaging of the data is not really relevant. We observe that most of the cases recorded follow a similar trajectory and tends toward the stationary regime $\varphi_s - \varphi_0 = 0.5\pi$, while three cases tend toward the stationary regime $\varphi_s - \varphi_0 = 2.5\pi$. The fact that there is exactly a phase shift of 2π between the two final stationary regimes suggests that the

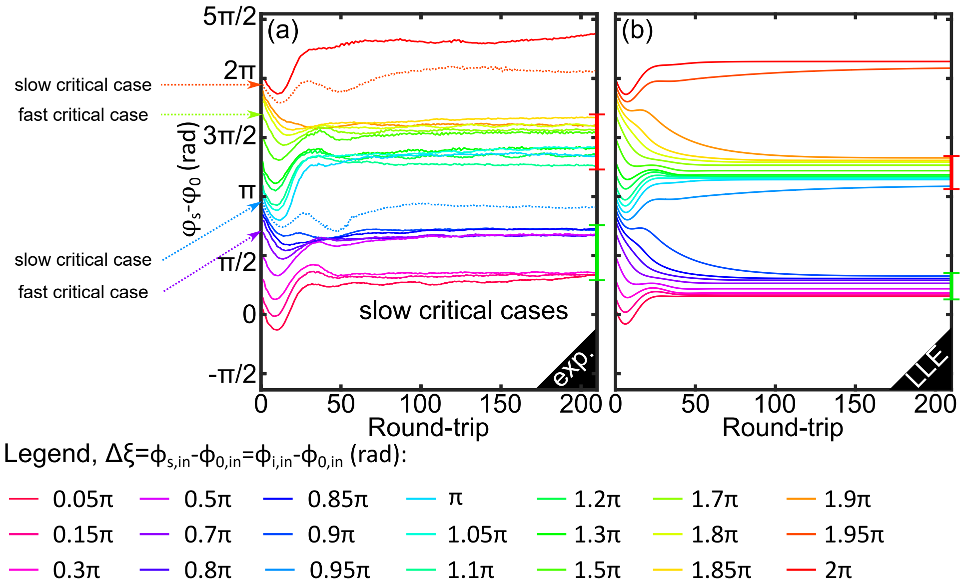

Figure 5.11: Relative phase between idler and intra-cavity pump versus round-trip number for different values of $\Delta\xi$. (a) stands for experimental results, and (c) for numerical simulations from the extended LLE (Eq. (5.1)).

reason for this behavior is not a physical phenomenon. At the time of writing, we are analyzing our numerical treatments, that we remind is still in progress, that could be probably responsible of this jump of 2π. We point out that the same behavior was observed for the case ”slow critical cases” $\Delta\xi = 1.95\pi$ (orange dotted curve in Fig. 5.11(a)) but was never observe for other cases. Thus, by omitting in Fig. 5.11(a)

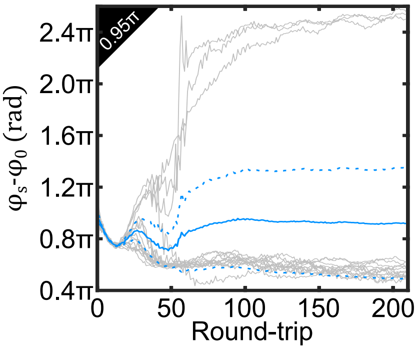

Figure 5.12: Evolution of the relative phase between signal and pump. The gray curves stand for raw data. The solid blue curves corresponds to the average of raw data and the dashed blue curves delimit the confidence interval of the averages (confidence level of 95%).

and in the following, the average curves of the ”slow critical cases”, we observe that the relative phase between the signal and pump reaches stationary regimes that always belongs on the approximated intervals $[2\pi/6; 3\pi/4]$ and $[5\pi/4; 10\pi/6]$ (green and red segments on the right y-axis in Fig. 5.11(a), respectively). We compared these results with the corresponding numerical simulations of the extended LLE (Eq. (5.6) that are depicted in Fig. 5.11(b). We observe that the dynamics between the numerical simulations and experiments is qualitative. As in experiments, the relative phase between signal and pump converges toward phase intervals. These intervals $[\pi/6; 2\pi/6]$ and $[7\pi/6; 8\pi/6]$ are depicted in Fig. 5.11(b) by the green and red segments on the right y-axis, respectively. We note that these intervals are narrower compared to those obtained in experiments (factor 2.5 between intervals in experiments and in numerical simulations) and shifted of approximately $\pi/4$. To conclude, these phase recordings give a first insight of the phase dynamics, that should be confirmed by further investigations, in particular concerning the numerical treatments.

5.3.3 Observation of the phase-sensitivity of the gain

In a first step, we checked from these measurements the conditions set by Eq. (5.23) to “reach” a saddle point. For this purpose, we plotted in Fig. 5.13 (a-d) the signal and pump power versus $\Delta\xi$ at the 25^{th}, 50^{th}, 75^{th} and 210^{th} round-trip, respectively (green, blue, magenta, and red dotted lines in Fig. 5.10, respectively). The square colored markers stand for the pump power and colored dots for the signal power recorded in experiments. In all cases, we observe that the signal power and pump power are π-periodic relative to $\Delta\xi$ and evolve in an opposite way due to the energy transfer between pump and sidebands. The minimum energy-transfer from pump to signal is always observed at about $\Delta\xi = 0.95\pi$ rad and $\Delta\xi = 1.95\pi$ rad. It corresponds to minima for the signal power and maxima for the pump. The positions of these minima are in quite good agreement with the phase-matching relation Eq. (5.23) that predicts the minimum energy-transfer at $\Delta\xi = 0.94\pi$ rad and $\Delta\xi = 1.94\pi$ rad (black dotted lines in Fig. 5.13 (a-d)). Then, we compared the experimental recordings to numerical simulations of the extended LLE (Eq. (5.1)). They are depicted in Fig. 5.13(a-d) by the blue curves and the red curves for the pump and signal power, respectively. We can see that, in all cases the pump power calculated from numerical simulations follows the same evolution than in experiments with an amplitude variation of approximately 4 dB. Concerning the signal power evolution, we observe that by increasing the round-trip number, the width of the two “hole” formed by the function obtained from numerical simulations decreases. In experiments, this behavior is not as clear. We observe that between Fig. 5.13(a) and (b), ($25^{th}$and 50^{th} round-trip) the width of the function decreases as in numerical simulations, but at the same time, the minima of the signal power increases. The reason for this behavior is that the minima we measure in experiments might not correspond exactly to the perfect minima. Thus, this small shift of this measure induces an overestimation of the signal power of the minima that increases with the round-trip number. Note that, as we show previously in section 5.1.2.2, the minima of the signal power function calculated from numerical simulations tend to the value predicted by the perfect phase-matching relation Eq. (5.23) for an increasing number of round-trips. This behavior is not highlighted by the experiments because the $\Delta\xi$ resolution (0.05π close to the minima)) of our measurement is too weak to see this small shift, which is of the order of 0.025π at the 25^{th} round-trip. To conclude, we report the first observation of phase-sensitivity of seeded MI with the striking feature representation of two saddle points.

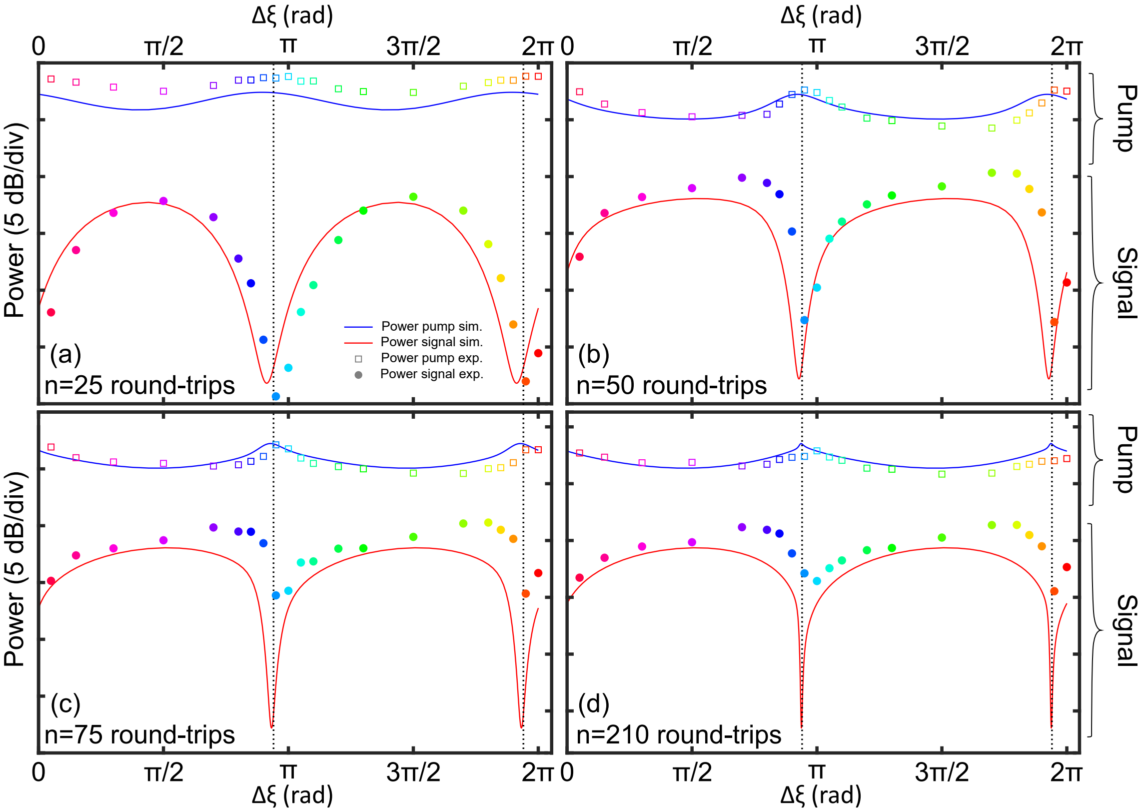

Figure 5.13: (a), (b), (c) and (d) Signal and intra-cavity pump power at the 25^{th},50^{th},75^{th} and 210^{th} round-trip versus $\Delta\xi$, respectively. The colored dots and square markers stands for the signal and pump power from experiments, respectively. The solid red lines and solid blue lines correspond to numerical simulations of the extended LLE (Eq. (5.1)). The black dotted lines marks the theoretical predictions of Eq. (5.23).

5.3.4 Physical insight of the attractors formation: preliminary results

In a second step, we studied the formation of attractors as a function of the relative phase between input components. For this purpose we depicted the acquired data in the polar phase plane (P_s, $\varphi_s - \varphi_0$) in Fig. 5.14(a) which is an other way to show the previous results (both the power and the phase evolution). We remind that the following outcome are only preliminary results that provide nonetheless first physical insights and a proof that in near future, our setup could be used for further investigations concerning the phase recording. By looking at Fig. 5.14(a) again, each colored curve corresponds to an investigated case of $\Delta\xi$ (see legend in Fig. 5.14), and the dots that compose them correspond to the performed measurements by our system at each round-trip. The black circular markers at the zero level stand for the initial states and the other black circular markers for the final states. We observe that the system converges to attractors whose phase belongs to the intervals we previously found in section 5.3.2 ($[2\pi/6; 3\pi/4]$ and $[5\pi/4; 10\pi/6]$). These attractors exhibit a "aircraft propeller" shape in really good agreement with theoretical predictions (see section 5.1.2.1). We compared these results to corresponding numerical simulations of the extended LLE (Eq. (5.1)). It is depicted in the polar phase plane (P_s, $\varphi_s - \varphi_0$) in Fig. 5.14(b). As in experiments, the system converges to attractors whose the phase can only reach certain intervals that we previously find in section 5.3.2 ($[\pi/6; 2\pi/6]$ and $[-5\pi/6; -4\pi/6]$). These attractors exhibit also a shape of "aircraft propeller", however the blades of the propeller are thinner and shifted of approximately $\pi/4$ in the phase plane. Such disagreement could originate from the fact that numerical simulations and theoretical development in this work are performed with modulated cw pump, whereas in experiments we use pulses of 10 ns. The second explanation to this disagreement, which is more relevant is that the cavity is not pumped perfectly synchronously (cavity round-trip time slightly different from the pulse repetition rate). In this case, the delay between the input pulse and the recirculating pulse induces an additional phase shift [181].

Finally, we focus on the initial stage of the seeded MI process in experiments by looking at the zoom on Fig. 5.14(a) depicted in Fig. 5.14(c). We see that the trajectories bifurcate close to two areas identified by gray color in Fig. 5.14(b). These regions correspond to the estimated positions of two saddle points. Their location at approximately $-\pi/4$ $[\pi]$ is in perfect agreement with theoretical predictions from Eq. (5.21) and numerical simulations (see zoom on Fig. 5.14(d)) that predicts saddle points located at $-\pi/4$ $[\pi]$ (black dots in Fig. 5.14(d), calculated from Eqs. (5.21-5.22)). Note also that we obtained a quite good agreement between the normalized power of the saddle points from theoretical predictions (Eq. (5.22), see black dots in Fig. 5.14(d)) and the estimated normalized power of the saddle points from experiments (gray area in Fig. 5.14(c)). To conclude, the experimental results are in qualitative agreement with numerical simulations of the extended LLE (Eq. (5.1)), and give a first insight of the formation of attractors. However, further numerical investigations should be necessary to fully unveil the phase dynamics of MI and the trajectory in the phase plane, in particular concerning the numerical treatments.

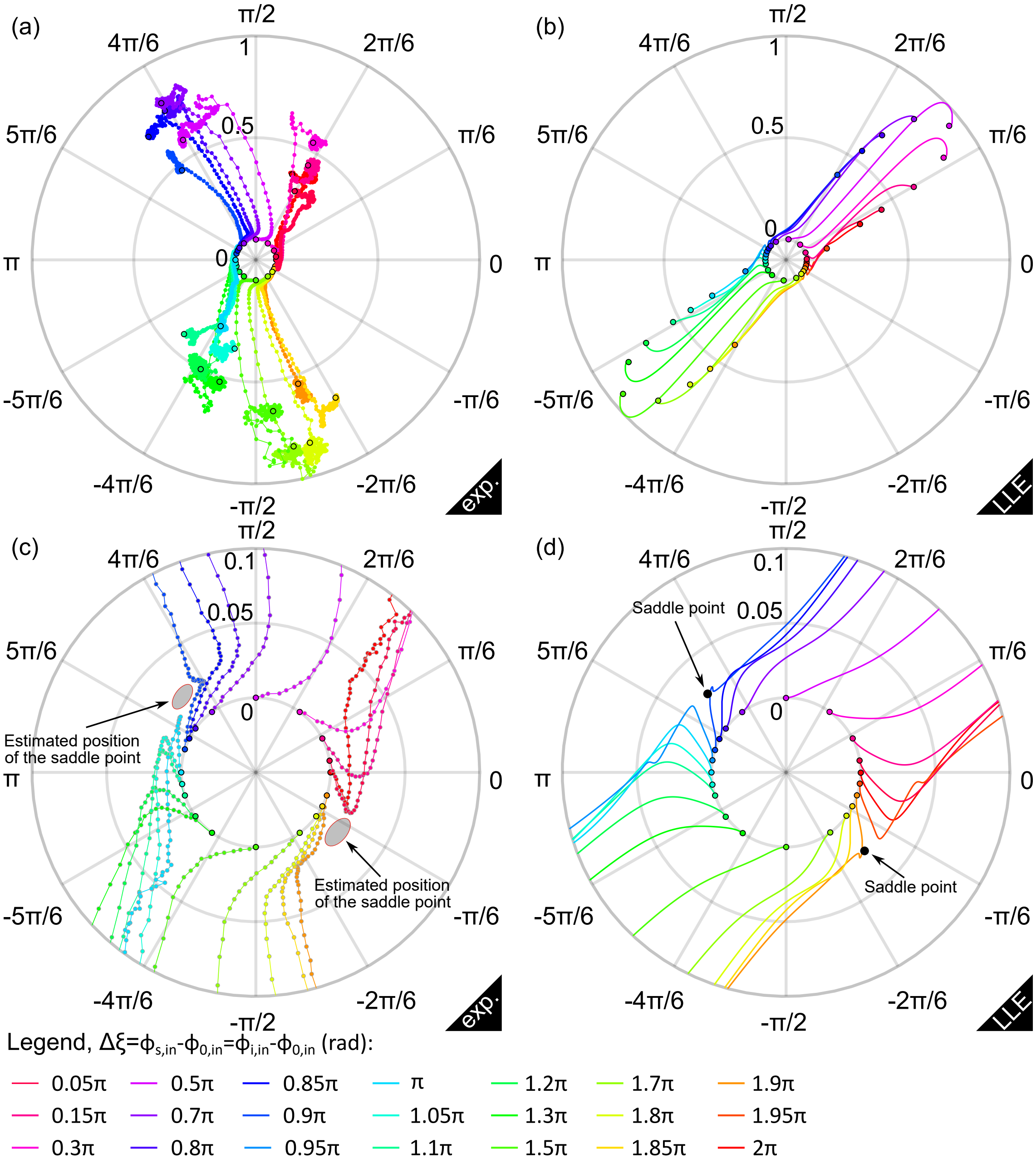

Figure 5.14: Normalized attractors for different input values of $\Delta\xi$ from experimental recordings (a), and numerical simulations of the extended LLE (Eq. (5.1)). (b)-(c), zooms on the initial stage of (a) and (b), respectively. Dots surrounded by black circles show the first dot (close to zero level) and the last dot for each of the recordings. Gray areas stand for the estimated position of the saddle points in experiments.

Summary

We investigated the dynamics of seeded modulation instability theoretically, numerically and finally in experiments. We predicted that both the transient regime and the stationary regime (attractors) of seeded MI are sensitive to the phase of the input components. This behavior has been observed in experiments in good agreement with theoretical predictions and numerical simulations of the extended LLE. In particular, we highlighted the existence of two saddle points that can be "reached" only for specific phase of the input components. These phase conditions have been checked in experiments by recording the sidebands power as a function of the relative phase between input seeds and pump for different propagation lengths. We also showed from theoretical development that for peculiar input phases, the trajectory of the system in the phase plane comes close to these saddle point, leading to a longer transient regime. Moreover, we predicted that the phase of stationary regime is always within two specific intervals in phase opposition. These behaviors were also observed in experiments from our preliminary results with a qualitative agreement with the theoretical predictions. However, further investigations are required to fully unveil the phase evolution, in particular concerning the numerical treatment of the phase recordings.

Conclusion

In this thesis, we investigated the generation of modulation instability in passive optical fiber-ring cavities. In particular, we focused on its experimental dynamics in unexplored regimes. The mains results we obtained can be summarized as follows:

- We demonstrated that higher order dispersion terms must be considered to accurately describe the dynamics of modulation instability operating in the weak normal dispersion regime. In particular, we showed that the FOD term is responsible for extending the MI process to the normal dispersion region: (i) in monostable regimes and (ii) on the upper-branch of bistable regimes compared to the basic configuration for which $\beta_4 = 0$. We also highlighted that for bistable regimes for which $\Delta > 4.25$, two pairs of MI sidebands can be generated above a certain pump wavelength threshold.
- We reported the first real-time observation of modulation instability in passive cavities thanks to a time-lens system. We demonstrated unambiguously that two different temporal behaviors of modulation instability can be observed in uniform cavities: the period-one and the period-two regimes. More precisely, the periodic temporal pattern generated at the cavity output can be in phase from round-trip to round-trip (period-one), or out-of-phase (period-two). Experimental observations are in good agreement with theoretical predictions and numerical simulations.
- We reported the first observation of gain-through-filtering process. We demonstrated theoretically and observed experimentally that the inclusion of unbalanced spectral losses compared to the pump wave lead to the generation of unstable modulation instability sidebands. We showed that an accurate description of the modulation instability dynamics requires to include the contribution of the dispersion of the filter, not only the absorption. Indeed, the dispersion of the filter is naturally associated to its dissipation profile through the causality principle (Kramer-Kronig relation [163]), and consequently cannot be neglected. We showed that this process can be used to generate OFCs whose repetition rate can be easily tuned by simply adjusting the pump-filter frequency detuning without requiring additional devices. This property is of high interest for applications, for instance in spectroscopy.

- We demonstrated both theoretically and experimentally, that coherent seeded MI in passive fiber cavities is sensitive to the phase of the components of the driving field. In particular, we showed that the parametric gain in this dissipative systems is phase sensitive ans has a minimum value. In order to understand this behavior, we derived a truncated three wave model based on the LLE equation describing the intra-cavity field dynamics. We demonstrated from this model that two saddle points exist in this system and are at the origin of this gain lowering for a specific phase value. An experimental setup had been designed and build to confirm these theoretical predictions. It consists in real-time recordings of the phase and intensity of the waves thanks to a multi-heterodyne detection scheme. We obtained preliminary results which confirm our theoretical findings but which must be improved to get a better quantitative agreement with theoretical predictions, in particular concerning the numerical treatment of the phase recordings.

The work described in this thesis paved the way for new fundamental observations:

- An interesting topic that could be investigated experimentally is the study of real-time dynamics, both in the spectral and temporal domain, of noise sedded MI . In particular, in the normal dispersion region of passive fiber cavities that operate in the bistable regime. Indeed, for $\Delta > 4.25$, we could observed the real-time dynamics of the transition between P1 MI regime on the lower-branch and P2 MI regime on the upper-branch. It could be performed with some upgrades of our experimental setup developed in chapter 3 that can record the temporal dynamics of MI, thanks to a time-lens. Indeed, by using a time-stretch dispersive Fourier transform [99] of the cavity output signal we could access simultaneously to the temporal dynamics and the spectral dynamics of MI. It could be performed by implementing a specially designed highly dispersive fiber that would operates a frequency-to-time mapping. Note that by both recording the temporal and spectral real-time dynamics we should be able to retrieved the phase dynamics, by using post-processing [182].
- We should also mentioned one of our studies which appears in Appendix D, where we investigate numerically the nonlinear stage of coherent seeded MI in passive fiber cavities. In particular we focus on the Lorenz chaos that is known to arise in cavities that operate in anomalous dispersion region, in particular for bistable regime. We show that our experimental setup developed in chapter 5, that implements an heterodyne measurement technique, should be a suitable platform in near future to report the first observation of this highly nonlinear regime in passive cavities. However, further theoretical investigations should be required to clearly characterize the phase-sensitivity to the components of the input field of such specific chaos.

In addition, this work is also of interest for the development of suitable applications:

- Our fundamental results reported in chapter 4 give a proof of concept of OFC generation through GTF mechanism. It could be interesting to study this process in resonators with higher field confinements. Indeed, it would improved strongly the efficiency of GTF process, and consequently would provide broader tunable OFCs that could be used for applications. As a first step, GTF could be studied in short Fabry-Perots made of FBG. The short length of such system (few centimeters) does not require active stabilization of the linear phase and consequently, we don't have to add an isolator inside the cavity that decreases strongly the cavity confinement. Generation of OFCs through GTF mechanism could be eventually developed for microresonator that should increase drastically the number of comb lines due to the high quality factor of such devices.

Appendices

Appendix A: Ikeda map model, Floquet analysis

Uniform cavity

The starting point of this analysis is the following Ikeda map system [39]:

$$\begin{cases} \dfrac{\partial E(z,\tau)}{\partial z} = \left(-i\dfrac{\beta_2}{2}\dfrac{\partial^2}{\partial \tau^2} + i\gamma|E(z,\tau)|^2\right)E(z,\tau) & (5.24) \\ E^{(m+1)}(z=0,\tau) = \widetilde{\theta}E_{in}(\tau) + \widetilde{\rho}E^{(m)}(z=L,\tau)\exp(i\phi_0) & (5.25) \end{cases}$$

Following the method described in [51, 120, 126], we then consider a steady-state continuous wave, solution of Eq. (5.24) $E_n(z,t) = \sqrt{P}\exp(i\gamma Pz)$ where P is related to the input power P_{in} through the steady-state cavity response $\widetilde{\theta}^2 P_{in} = [P(1+\widetilde{\rho}^2 - 2\widetilde{\rho}\cos(\phi))]$ (see Eq. (1.12)). The stability of this solution is analyzed by introducing the Antsatz: $E_n(z,t) = (\sqrt{P} + a_n(z,\tau) + b_n(z,\tau))\exp(i\gamma Pz)$ in Eq. (5.24), where $a_n(z)$, and $b_n(z)$ are small perturbations. After linearization around the stationary solution at the first order of $a_n(z)$, and $b_n(z)$, the Fourier transform of $[a_n, b_n]^T$ satisfies the linear system $d/dz[\widetilde{a}_n(\Omega), \widetilde{b}_n(\Omega)]^T = M[\widetilde{a}_n(\Omega), \widetilde{b}_n(\Omega)]^T$ ($\widetilde{\ }$denotes the Fourier transform) which describes the evolution of the perturbations over one round-trip where:

$$M = \begin{bmatrix} i\frac{\beta_2}{2}\Omega^2 + i\gamma P & i\gamma P \\ -i\gamma P & -i\frac{\beta_2}{2}\Omega^2 - i\gamma P \end{bmatrix} \tag{5.26}$$

The eigenvalues of this matrix give the standard MI gain such as $\mu = \sqrt{\frac{\beta_2^2\Omega^4}{4} + \beta_2\gamma P\Omega^2}$. Then we can express the solutions of this system over one cavity round-trip by $[\widetilde{a}_n(\Omega, L), \widetilde{b}_n(\Omega, L)]^T = \Phi[\widetilde{a}_n(\Omega, 0), \widetilde{b}_n(\Omega, 0)]^T$ where the fundamental matrix Φ is:

$$\begin{bmatrix} (\cos(\mu L) + i\kappa\sin(\mu L)) & -\frac{\gamma P}{\mu}\cos(\mu L) \\ \frac{\gamma P}{\mu}\cos(\mu L) & (\cos(\mu L) - i\kappa\sin(\mu L)) \end{bmatrix} \tag{5.27}$$

with $\zeta = \frac{\beta_2}{2}L\Omega^2 + \gamma PL$. The relation between the initial perturbations and perturbations at n-th round-trip can be found by applying boundary conditions Γ:

$$\widetilde{\rho}\begin{bmatrix} e^{i\phi} & 0 \\ 0 & e^{-i\phi} \end{bmatrix} \tag{5.28}$$

with $\phi = \gamma LP + \phi_0$, on solutions of this system such as $[\widetilde{a}_n(\Omega, 0), \widetilde{b}_n(\Omega, 0)]^T = \Theta^n[\widetilde{a}_0(\Omega, 0), \widetilde{b}_0(\Omega, 0)]^T$. As a result, the stability of this system depends on eigenvalues of $\Theta = \Phi\Gamma$. For modulus of eigenvalues larger than unit, the steady-state cw solution is unstable and perturbations grow exponentially. By assuming fiber propagation losses are negligible relative to the output coupling, cavity losses are defined by $\alpha = \pi/\mathcal{F} = 1 - \widetilde{\rho}$ and consequently these eigenvalues are expressed as:

$$\lambda_{\pm} = (1-\alpha)[\Psi \pm \sqrt{\Psi^2 - 1}] \tag{5.29}$$

where

$$\Psi = \cos(\mu L)\cos(\phi) - \zeta \sinh(\mu L)\sin(\phi) \tag{5.30}$$

The parameter $\phi = \phi_0 + \gamma LP$ corresponds to the total phase accumulated over a cavity round-trip and:

$$\mu = \sqrt{\beta_2^2\Omega^4/4 + \beta_2\gamma P\Omega^2} \tag{5.31}$$

is the standard MI gain with Ω the pulsation of the perturbation and $\zeta = \beta_2\Omega^2 L/2 + \gamma PL$. It can be easily checked that unstable eigenvalues ($|\lambda_{\pm}|>1$) appear only for $|\Psi| > (1-\alpha+1/(1-\alpha))/2$ and are always real such as these eigenvalues can be expressed as $\lambda = |\lambda|e^{im\pi}$ with m integer.

Cavity including a filter

When passive resonator includes a spectral filter, the stability of the steady-state can be analyzed following the same method detailed in the previous section. However, the action of the filter must be take into account. This is performed by including the action of the filter in the boundary conditions such as Eq. (5.28) becomes:

$$\underbrace{\widetilde{\rho}\begin{bmatrix} e^{i\phi} & 0 \\ 0 & e^{-i\phi}\end{bmatrix}}_{coupler}\underbrace{\begin{bmatrix} H(\Omega) & 0 \\ 0 & H^*(-\Omega)\end{bmatrix}}_{filter} \tag{5.32}$$

where $H(\omega)$ is the filter transfer function of the filter in the spectral domain. Note that the filter and coupler matrices commutes. Consequently, for the stability analysis it does not matter if we place the filter just before or just after the coupler. By using these new boundary conditions in the linear stability analysis developed in the previous section, we get the following eigenvalues that describe the dynamics of the system:

$$\lambda_{,\pm} = (1-\alpha)\left[\Psi_{GTF} \pm \sqrt{\Psi_{GTF}^2 - W}\right] \tag{5.33}$$

with

$$\begin{aligned}\Psi_{GTF} = &\cos(\mu L)\left[H_e(\Omega)\cos(\phi) - H_0(\Omega)\sin(\phi)\right] \\ &- \zeta \operatorname{sinc}(\mu L)\left[H_o(\Omega)\cos(\phi) + H_e(\Omega)\sin(\phi)\right]\end{aligned} \tag{5.34}$$

$$W = H_e^2(\Omega) + H_o^2(\Omega) \tag{5.35}$$

The parameters $H_{e,o}(\Omega) = [H(\Omega) + H^*(-\Omega)]/2$ and $H_o(\Omega) = [H(\Omega) - H^*(-\Omega)]/(2i)$ are the even and odd part of the filter function $H(\Omega)$, $\mu = \sqrt{\beta_2^2\Omega^4/4 + \beta_2\gamma P\Omega^2}$ is the standard MI gain with Ω the pulsation of the perturbation and $\zeta = \beta_2\Omega^2 L/2 + \gamma PL$.

Stability of the cw states

Note that these analysis does not only provide the stability of perturbed solutions but also provides the stability of the homogeneous states (uniform cavity: Eq. (1.12), GTF: Eq. (4.7)). Indeed, the stability analysis of these states follows the same theoretical development except that we initially consider that $\partial/\partial\tau = 0$ (steady-state condition). This is equivalent in the previous development to consider $\beta_2 = 0$, $\Omega = 0$, and thus $\mu = 0$, $\Psi = \cos(\phi) - \gamma LP\sin(\phi)$ in the case of uniform cavities and $\Psi_{GTF} = \left[H_e\left(0\right)\cos\left(\phi\right) - H_o\left(0\right)\sin\left(\phi\right)\right] - \gamma LP\left[H_o\left(0\right)\cos\left(\phi\right) + H_e\left(0\right)\sin\left(\phi\right)\right]$ in the case of GTF. As a result, cw states become unstable when $|\lambda(\beta_2 = 0)| > 1$. This appears when $|\Psi| > \left[\left(1-\alpha\right)^2 + 1\right] / \left[2\left(1-\alpha\right)\right]$ (uniform cavities) and $|\Psi_{GTF}| > \left[|H\left(0\right)|^2\left(1-\alpha\right)^2 + 1\right] / \left[2|H\left(0\right)|\left(1-\alpha\right)\right]$ (GTF) and it corresponds exactly to the negative slopes of the steady-state curve (Eq. (1.12) and Eq. (4.7), respectively) whose the knees ($P_{m,\pm}$) are defined by the relation:

$$\phi_0 = \pm\arccos\left(\frac{1+\left(1-\alpha\right)^2}{2\left(1-\alpha\right)\sqrt{1+\left(\gamma LP_{m,\pm}\right)^2}}\right) - \gamma LP_{m,\pm} \tag{5.36}$$

$$-\arctan\left(\gamma LP_{m,\pm}\right) + 2m\pi \quad \left(m \in \mathbb{Z}\right) \tag{5.37}$$

in the case of uniform cavities and by:

$$\phi_0 + \arg\left[H\left(0\right)\right] = \pm\arccos\left(\frac{1+\left(1-\alpha\right)^2|H\left(0\right)|^2}{2\left(1-\alpha\right)|H\left(0\right)|\sqrt{1+\left(\gamma LP_{m,\pm}\right)^2}}\right) - \gamma LP_{m,\pm} \tag{5.38}$$

$$-\arctan\left(\gamma LP_{m,\pm}\right) + 2m\pi \quad \left(m \in \mathbb{Z}\right) \tag{5.39}$$

in the case of cavities that include a spectral filter.

Appendix B: determination of the saddle point conditions

We look for the conditions for which:

$$C_1 = \frac{-i}{2}\left[\theta\sqrt{S}e^{i\left(2\phi_0-\phi_{s,in}\right)}\left(e^{i\left(\frac{\pi}{2}+\Delta\eta\right)} - 1\right) - \sqrt{F}e^{i\left(2\phi_0-\phi_s\right)}\left(e^{i\left(\frac{\pi}{2}+\phi_s+\phi_i-2\phi_0\right)} - 1\right)\right] \tag{5.40}$$

where $\Delta\eta = \phi_{s,in} + \phi_{i,in} - 2\phi_0$, is equal to zero. In the following, we will demonstrate that these conditions are given by the phase-matching relation:

$$\boxed{\phi_s + \phi_i - 2\phi_0 = -\frac{\pi}{2}\ \left[2\pi\right]} \tag{5.41}$$

In Eq. (5.40) that defines the coefficient C_1, the above relation means that the left term proportional to $\sqrt{F}$ is equal to zero. Thus, the right term of Eq. (5.18) that is proportional to $\sqrt{S}$ must also be equal to zero to satisfy $C_1 = 0$. To check this, we need to express $\Delta\eta = \phi_{s,in} + \phi_{i,in} - 2\phi_0$ as a function of ϕ_0, ϕ_s, and ϕ_i. For this purpose we remind that:

$$\bar{E}_{i/s} = \sqrt{F}e^{i\phi_{i/s}} = \frac{\widetilde{\theta}\sqrt{S}e^{i\phi_{i,in/s,in}}\left[\alpha + i\gamma LPe^{-i\Delta\eta}\right]}{\alpha^2 - \gamma^2L^2P^2} \tag{5.42}$$

This equation can be used to express $\phi_{s,in}$ and $\phi_{i,in}$ as a function of ϕ_s and ϕ_i. We find that:

$$\phi_{i,in/s,in} = -\arctan\left(\frac{\gamma P\cos(\Delta\eta)}{\gamma P\sin(\Delta\eta) + \dfrac{\alpha}{L}}\right) + \phi_{i/s} - p\pi \;\; [2\pi] \tag{5.43}$$

$$\begin{cases} p = 0 & \text{if } \Delta\eta \in \left]-\arcsin\left(\dfrac{P_{th}}{P}\right); \arcsin\left(\dfrac{P_{th}}{P}\right) + \pi\right[\;\; [2\pi] \vee \Delta\eta = -\dfrac{\pi}{2} \;\; [2\pi] \\ p = 1 & \text{if } \Delta\eta \in \left]-\arcsin\left(\dfrac{P_{th}}{P}\right); -\dfrac{\pi}{2}\right[\;\; [2\pi] \\ p = -1 & \text{if } \Delta\eta \in \left]-\dfrac{\pi}{2}; \arcsin\left(\dfrac{P_{th}}{P}\right) - \pi\right] \;\; [2\pi] \end{cases} \tag{5.44}$$

Consequently by substituting $\phi_{i,in/s,in}$ by Eq. (5.43) in $\Delta\eta$ we obtain:

$$\Delta\eta = \underbrace{\phi_s + \phi_i - 2\phi_0}_{-\frac{\pi}{2}\text{ Eq.5.41}} - 2\arctan\left(\frac{\gamma P\cos(\Delta\eta)}{\gamma P\sin(\Delta\eta) + \dfrac{\alpha}{L}}\right) \;\; [2\pi] \tag{5.45}$$

The only solutions that satisfy this equation are $\Delta\eta = \phi_{s,in} + \phi_{i,in} - 2\phi_0 = -\pi/2$ $[2\pi]$ for which the arc tangent term is equal to zero. Thus, the left term of C_1 in Eq. (5.17) is also equal to zero, hence $C_1 = 0$ for $\phi_s + \phi_i - 2\phi_0 = -\pi/2$ $[2\pi]$ (QED). We have just determinated the phase relation satisfied by the saddle points, in the following we want to determinate their power coordinate. This is performed by looking for the steady-states define by Eq. (5.42) that satisfy the phase-matching relation Eq. (5.41) (for which $\Delta\eta = -\pi/2$ $[2\pi]$) and correspond to saddle points. We find taking the square modulus of Eq. (5.42) that this power coordinate is given by:

$$\boxed{F_{saddle\,point} = \frac{\theta^2 S}{L^2\left(\dfrac{\alpha}{L} + \gamma P\right)^2}} \tag{5.46}$$

Finally, we can calculate a phase-matching relation that must satisfy the phase of the input components to reach asymptotically a saddle point and for which there is no gain. For this purpose, we use the relation $\Delta\eta = \phi_{s,in} + \phi_{i,in} - 2\phi_0 = -\pi/2\ [2\pi]$ and we express ϕ_0 as a function of $\phi_{0,in}$. By reminding that:

$$\bar{E}_0 = \sqrt{P}e^{i\phi_0} = \frac{i\widetilde{\theta}\sqrt{P_{in}}e^{i\phi_{0,in}}}{\gamma LP - \delta_0 + i\alpha} \tag{5.47}$$

We find that:

$$\phi_0 = \arctan(\frac{-\alpha}{\gamma LP - \delta_0}) + \phi_{0,in} + r\frac{\pi}{2}\ [2\pi] \tag{5.48}$$

$$\Big\{ r = 1 \quad \text{if}\, P \geq \delta_0/(\gamma L)\, \text{else}\, r = -1 \tag{5.49}$$

Thus, by substituting ϕ_0 by Eq. (5.48) in $\Delta\eta = \phi_{s,in} + \phi_{i,in} - 2\phi_0 = -\pi/2\ [2\pi]$ we obtain the following relation:

$$\boxed{\phi_{i,in} + \phi_{s,in} - 2\phi_{0,in} = 2\arctan\left(\frac{-\alpha}{\gamma LP - \delta_0}\right) + \frac{\pi}{2}\ [2\pi]} \tag{5.50}$$

that must be satisfied by the phase of the input components to “reach” asymptotically a saddle point.

Appendix C

detuning adjustement

The detuning of idler and signal components are defined by $\delta_i = \delta_0 - 2l\pi + \beta_1\Omega L$ and $\delta_s = \delta_0 + 2l\pi - \beta_1\Omega L$ with $l = \arg\left[\min_l |\delta_0 + 2l\pi - \beta_1\Omega L|\right]$ as mentioned in section 5.1.2. Thus, the detuning of the pump, idler and signal are equal if $\beta_1\Omega L = 2k\pi$ $(k \in \mathbb{Z})$. This condition is satisfied for specific frequencies that are equally spaced. So, in order to set the detunings such as $\delta_0 = \delta_s = \delta_i$, we must determinate the seeds frequencies that satisfy the relation $\beta_1\Omega L = 2k\pi$ $(k \in \mathbb{Z})$. For this purpose, we record the evolution of the relative phase between signal (idler) and pump. By reminding that the linear phase shift accumulated by a component of frequency $\Omega = \pm\omega - \omega_0$ (ω_0 stands for the angular frequency of the pump) along a cavity round-trip is given by:

$$\phi_L = \beta_0 L + \beta_1\Omega L + \frac{\beta_2}{2}\Omega^2 L + \text{HOT} \tag{5.51}$$

where HOT stand for High-order terms. We find that the total phase shift accumulated between signal (idler) and pump along the propagation are given by:

$$\varphi_s - \varphi_0 = \phi_{s,L} - \phi_{0,L} + \phi_{NL}\left(z = nL\right) = \phi_{NL}\left(z = nL\right) - \beta_1\Omega L + 2n\pi + \text{HOT} \tag{5.52}$$

$$\varphi_i - \varphi_0 = \phi_{i,L} - \phi_{0,L} + \phi_{NL}\left(z = nL\right) = \phi_{NL}\left(z = nL\right) + \beta_1\Omega L - 2n\pi + \text{HOT} \tag{5.53}$$

where $\phi_{NL}\left(z = nL\right)$ corresponds to the nonlinear phase shift between signal (idler) and pump accumulated along the n^{th} round-trip. The parameters $\phi_{s/i,L}$ and $\phi_{0,L}$ denote the linear phases accumulated along a cavity round-trip by the signal/idler and pump, respectively. Based on the theoretical and the numerical observations we made in section 5.1, we can assume that just above the MI cavity threshold, $\phi_{NL}\left(z = nL\right)$ converges toward a stationary regime. Moreover, the high-order terms in Eqs. (5.52-5.53) are weak relative to other terms. Hence, for $z \to +\infty$, the terms $\pm\beta_1\Omega L \mp 2n\pi$ in Eqs. (5.52-5.53) become dominant and $\varphi_s - \varphi_0$ and $\varphi_i - \varphi_0$ tends asymptotically to a linear function with a slope of $^-/_+\beta_1\Omega L\ [2\pi]$, respectively. Thus,

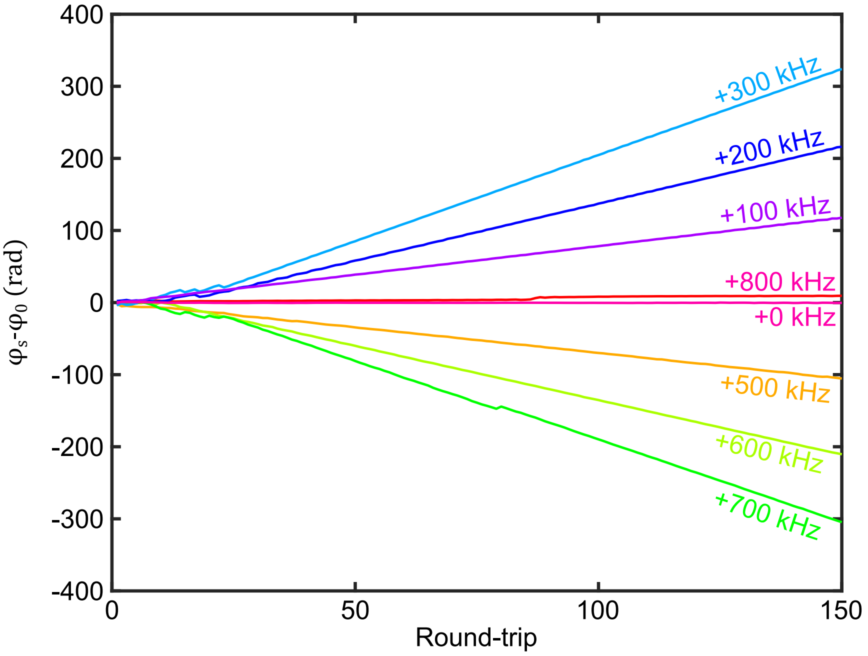

Figure 5.15: Relative phase between the signal and pump field versus the round-trip number for different seed frequencies.

by tuning the seeds frequencies, we should observe for specific frequency that the slope of $\varphi_s - \varphi_0$ is equal to zero, meaning that our system satisfies the condition $\delta_0 = \delta_s = \delta_i$. Note that, we also should observe that this specific frequencies are equally spaced, and by reminding that β_1 is the inverse of the group velocity ($\beta_1 = c/n_g$ where n_g is the group index), this frequency spacing is given by:

$$f_{\beta_1} = \frac{c}{n_g L} \tag{5.54}$$

In our case, our cavity is made of standard silica SMF where $n_g \approx n$ (refractive index). Thus, for a seed frequency that satisfies the condition $\beta_1\Omega L = 2k\pi$ ($k \in \mathbb{Z}$), by tuning the seed frequency of the free spectral range ($c/\left(nL\right)$), the new seed frequency should satisfies also this condition.

We checked experimentally this behavior during a preliminary work to the investigations led in chapter 5. For this purpose, we recorded in a cavity made of 257 m of SMF the evolution of the relative phase between signal and pump for different frequencies. This recordings depicted in Fig. 5.15 have been performed in a range corresponding approximately to the FSR of this cavity (791, 68 kHz). We first set the seeds frequencies such as the slope of $\varphi_s - \varphi_0$ is equal to zero. This recording is depicted by the curve labeled *+0 kHz*. Then, we increased the seeds frequency by step of 100 kHz until $\Delta f = +800$ kHz. We observe that the slope of $\varphi_s - \varphi_0$ increases until $\Delta f = +400$ kHz. Finally, by increasing again Δf the slope of $\varphi_s - \varphi_0$ becomes negative, increases and becomes quasi-equal to zero for approximately $\Delta f = +800$ kHz. Indeed, in this case, $\Delta f = +800$ kHz is close to the FSR (791, 68 kHz), and the condition $\beta_1 \Omega L = 2k\pi$ ($k \in \mathbb{Z}$) is almost satisfied.

Pump and seeds power evolutions for $\Delta\xi \in [\pi; 2\pi]$

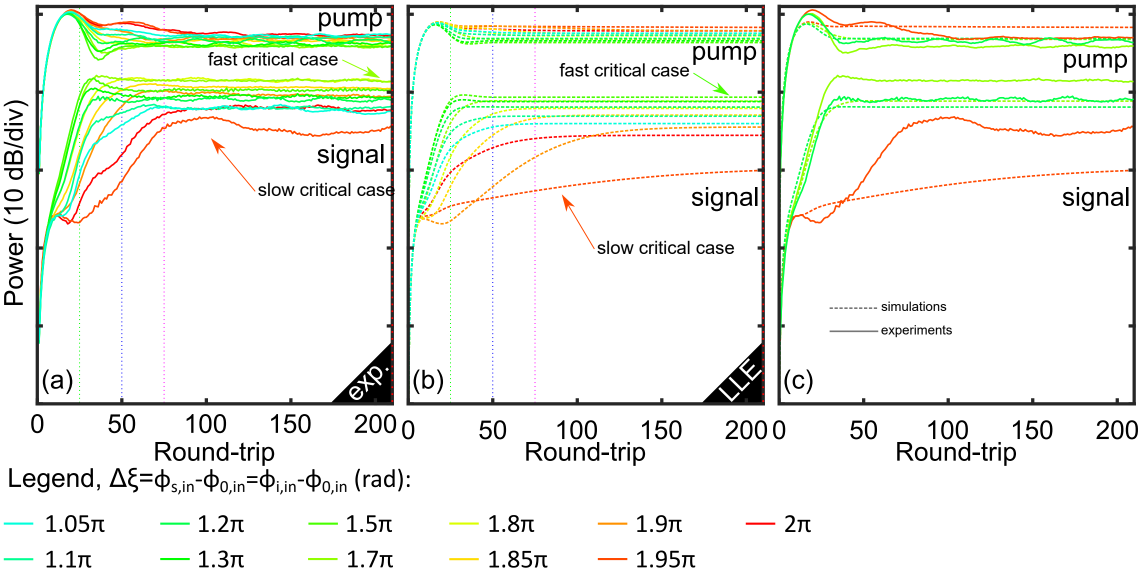

Figure 5.16: Signal and intra-cavity pump power versus round-trip number for different value of $\Delta\xi$ between π and 2π. (a) stand for experimental results, (b) for numerical simulations of the extended LLE (Eq. (5.1)). (c) Comparison of the pump and signal evolutions from experiments and numerical simulations for $\Delta\xi = 1.2\pi,\ 1.7\pi,\ 1.95\pi$ rad in (c).

Appendix D: toward a precise observation of spatially coherent chaos in passive resonators, the Lorenz chaos

Short state of the art

In 1963, Lorenz derived a simplified model of three coupled differential equations to describe the dynamics of the coupling between the atmosphere and ocean (convection). He discovered from his numerical investigations that, beyond to be sensitive to the initial conditions (characteristic of chaos), the system follows in the phase plane (described by the three degrees of freedom of the system: three main modes, pump, signal and idler fields) unpredictable non-periodic trajectories that oscillate from an attractor to another, and form a so-called *"butterfly"* [183]. Such peculiar chaotic regimes was also predicted in optics through the direct analogy between the equations that describe fluid and light dynamics [184]. It was even experimentally highlighted in laser through heterodyne measurements [185] and in diode laser [186] by using specific chaos identification techniques (Grassberger-Procaccia algorithm). These regimes were also predicted in passive resonators by Haelterman *et al.* [187], showing that the system can be modeled by a similar TWM to the one described by Lorenz. These authors highlighted the route to this chaos, where by increasing the power the trajectory in the phase plane describing the dynamics of the system spirals toward an attractor, then towards a second attractor and finally oscillates in a non-periodic way between these two attractors that is the clear signature of Lorenz chaos. We point out that the TWM we develop in chapter 5 to describe coherent seeded MI was derived using the same method than Haelterman *et al.*, except that our pump consist in three components. Hence, we expect to observe in a similar way to seeded noise MI the Lorenz chaos for seeded MI.

Numerical investigations of the Lorenz chaos

In this section, we investigate the Lorenz chaos in seeded passive resonators, as a preliminary step for an experimental observation. In particular, we look for configurations that should allow experimental observations of such chaotic regime in the experimental setup developed in chapter 5. As observed by Haelterman *et al.* in Ref. [187], numerical simulations of the extended LLE (Eq. (5.1)), performed with experimental parameters of our setup, show that the Lorenz chaos can only be observed above a certain detuning threshold where the system is bistable, on the upper-branch of the bistable cycle. In experiments, we are limited to observe the regimes of the upper-branch for an input power higher than the input power of the lower-knee of the bistable cycle. Indeed, in experiments, the cavity is initially empty, meaning that if we want to observe a peculiar regime, for example the Lorenz chaos on the upper-branch close to the upper-knee of the bistable cycle, we must pump the cavity following the scheme of Fig. 5.17(a). First, we must pump the cavity above the input power of the lower-knee to switch the system on the upper-branch (green vertical arrow, green dot in Fig. 5.17(a)), and then decrease the power adiabatically until we reach the configuration we want to investigate (black dot in Fig. 5.17(a)). This is really tricky to do in experiments and requires to manage the input power. Consequently, if we want to observe the Lorenz chaos, we must find a configuration where it appears for an input power higher than the input power of the lower-knee of the bistable cycle. We observed such a behavior in numerical simulations of the extended LLE (Eq. (5.1)), by seeding the system at the most unstable frequencies (Ω_T, calculated from Eq. (5.1)) for $\Delta = 3$ and $P_{in} = 0.7$ W(see red dot in Fig. 5.17(a)). We depicted the dynamics of the system in the phase plane $(P_{s/i}, \varphi_s - \varphi_0)$ in Fig. 5.17(b). The trajectory follows an unpredictable non-periodic trajectory in the phase that oscillates from an attractor to another. This trajectory looks-like a *"butterfly"*, the clear signature of Lorenz chaos. The main difference we observed with Ref. [187] in numerical simulations of the extended LLE is that the position of these attractors depends on the phase of the input components, resulting in a rotation of their position in the phase plane. Obviously, further investigations are required to understand the impact of the initial input phases on the Lorenz chaos. However, numerical and primary experimental results of chapter 5 demonstrate that our setup is the suitable platform to investigate in near future this Lorenz chaos by recording the phase and intensity evolution of the waves.

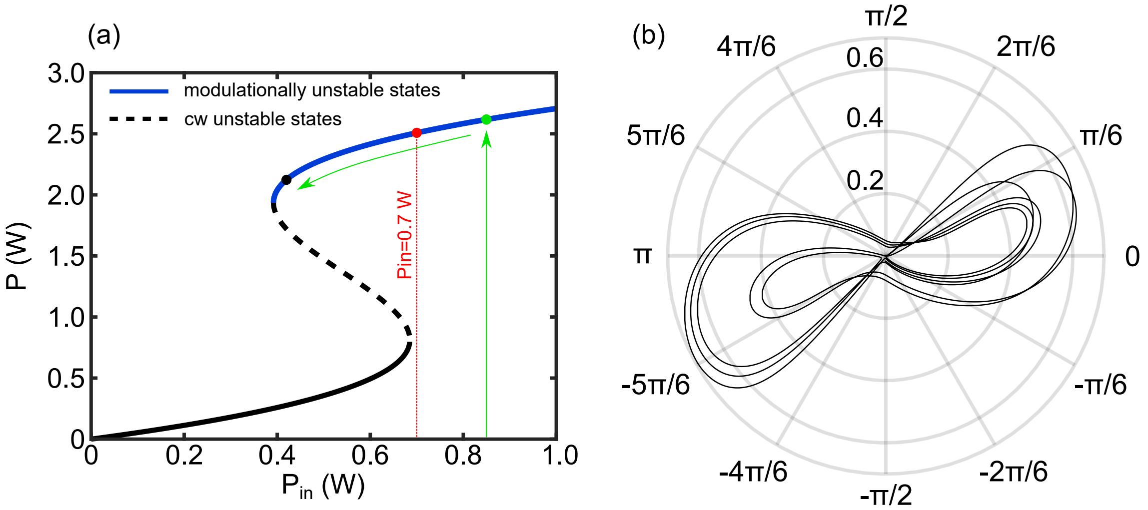

Figure 5.17: (a) Steady-state curve for $\Delta = 3$. Dashed black, solid black, and solid blue curves stand for the cw unstable, stable states and modulationally unstable states, respectively. (b) Trajectory of the dynamics of the system in the phase plane $(P_{s/i}, \varphi_s - \varphi_0)$ in the case of $\Delta\xi = 0$ rad, corresponding to the configuration marked by the red dot in (a).

APPENDICES

Bibliography

[1] M. Göppert-Mayer, “Elementary processes with two quantum transitions,” *Annalen der Physik*, vol. 18, no. 7-8, pp. 466–479, 2009. English translation of M. Göppert-Mayer, “Über Elementarakte mit zwei Quantensprüngen,” Annalen der Physik, vol. 401, no. 3, pp. 273–294, 1931, by Daniel C. Koepke, Montana State University, Department of Physics, Bozeman, MT 59717-3840, USA.

[2] A. Smekal, “Zur Quantentheorie der Dispersion,” *Naturwissenschaften*, vol. 11, pp. 873–875, Oct. 1923.

[3] C. V. Raman and K. S. Krishnan, “A New Type of Secondary Radiation,” *Nature*, vol. 121, pp. 501–502, Mar. 1928.

[4] G. N. Lewis, D. Lipkin, and T. T. Magel, “Reversible Photochemical Processes in Rigid Media. A Study of the Phosphorescent State,” *Journal of the American Chemical Society*, vol. 63, pp. 3005–3018, Nov. 1941.

[5] T. H. Maiman, “Optical and Microwave-Optical Experiments in Ruby,” *Physical Review Letters*, vol. 4, pp. 564–566, June 1960.

[6] P. A. Franken, A. E. Hill, C. W. Peters, and G. Weinreich, “Generation of Optical Harmonics,” *Physical Review Letters*, vol. 7, pp. 118–119, Aug. 1961.

[7] W. Kaiser and C. G. B. Garrett, “Two-Photon Excitation in CaF_2:Eu^{2+},” *Physical Review Letters*, vol. 7, pp. 229–231, Sept. 1961.

[8] E. J. Woodbury and W. K. NG, “Ruby laser operation in the near ir,” *Proc. IRE*, vol. 50, p. 2367, 1962.

[9] P. D. Maker, R. W. Terhune, and C. M. Savage, “Intensity-Dependent Changes in the Refractive Index of Liquids,” *Physical Review Letters*, vol. 12, pp. 507–509, May 1964.

[10] R. Y. Chiao, C. H. Townes, and B. P. Stoicheff, “Stimulated Brillouin Scattering and Coherent Generation of Intense Hypersonic Waves,” *Physical Review Letters*, vol. 12, pp. 592–595, May 1964.

[11] R. L. Carman, R. Y. Chiao, and P. L. Kelley, “Observation of Degenerate Stimulated Four-Photon Interaction and Four-Wave Parametric Amplification,” *Physical Review Letters*, vol. 17, pp. 1281–1283, Dec. 1966.

[12] E. Snitzer, “Optical Maser Action of Nd^{+3} in a Barium Crown Glass,” *Physical Review Letters*, vol. 7, pp. 444–446, Dec. 1961.

[13] C. J. Koester and E. Snitzer, “Amplification in a Fiber Laser,” *Applied Optics*, vol. 3, pp. 1182–1186, Oct. 1964.

[14] E. Snitzer, “Cylindrical Dielectric Waveguide Modes,” *JOSA*, vol. 51, pp. 491–498, May 1961.

[15] K. C. Kao and G. A. Hockham, “Dielectric-fibre surface waveguides for optical frequencies,” *Proceedings of the Institution of Electrical Engineers*, vol. 113, pp. 1151–1158, July 1966.

[16] F. P. Kapron, D. B. Keck, and R. D. Maurer, “Radiation losses in glass optical waveguides,” *Applied Physics Letters*, vol. 17, pp. 423–425, Nov. 1970.

[17] E. Ippen and R. Stolen, “Stimulated Brillouin scattering in optical fibers,” *Applied Physics Letters*, vol. 21, pp. 539–541, Dec. 1972.

[18] R. H. Stolen, E. P. Ippen, and A. R. Tynes, “Raman Oscillation in Glass Optical Waveguide,” *Applied Physics Letters*, vol. 20, pp. 62–64, Jan. 1972.

[19] R. H. Stolen and C. Lin, “Self-phase-modulation in silica optical fibers,” *Physical Review A*, vol. 17, pp. 1448–1453, Apr. 1978.

[20] R. Stolen and A. Ashkin, “Optical Kerr effect in glass waveguide,” *Applied Physics Letters*, vol. 22, pp. 294–296, Mar. 1973.

[21] R. H. Stolen, J. E. Bjorkholm, and A. Ashkin, “Phase-matched three-wave mixing in silica fiber optical waveguides,” *Applied Physics Letters*, vol. 24, pp. 308–310, Apr. 1974.

[22] R. Stolen, “Phase-matched-stimulated four-photon mixing in silica-fiber waveguides,” *IEEE Journal of Quantum Electronics*, vol. 11, pp. 100–103, Mar. 1975.

[23] A. Hasegawa and F. Tappert, “Transmission of stationary nonlinear optical pulses in dispersive dielectric fibers. I. Anomalous dispersion,” *Applied Physics Letters*, vol. 23, pp. 142–144, Aug. 1973.

[24] L. F. Mollenauer, R. H. Stolen, and J. P. Gordon, “Experimental Observation of Picosecond Pulse Narrowing and Solitons in Optical Fibers,” *Physical Review Letters*, vol. 45, pp. 1095–1098, Sept. 1980.

[25] L. F. Mollenauer and R. H. Stolen, “The soliton laser,” *Optics Letters*, vol. 9, pp. 13–15, Jan. 1984.

[26] V. E. Zakharov and L. A. Ostrovsky, “Modulation instability: The beginning,” *Physica D: Nonlinear Phenomena*, vol. 238, pp. 540–548, Mar. 2009.

[27] T. B. Benjamin, “Instability of periodic wavetrains in nonlinear dispersive systems,” *Proceedings of the Royal Society of London. Series A. Mathematical and Physical Sciences*, June 1967.

[28] T. Taniuti and H. Washimi, “Self-Trapping and Instability of Hydromagnetic Waves Along the Magnetic Field in a Cold Plasma,” *Physical Review Letters*, vol. 21, pp. 209–212, July 1968.

[29] Y. S. Kivshar and M. Peyrard, “Modulational instabilities in discrete lattices,” *Physical Review A*, vol. 46, pp. 3198–3205, Sept. 1992.

[30] P. D. Miller and O. Bang, “Macroscopic dynamics in quadratic nonlinear lattices,” *Physical Review E*, vol. 57, pp. 6038–6049, May 1998.

[31] V. I. Bespalov and V. I. Talanov, “Filamentary Structure of Light Beams in Nonlinear Liquids,” *ZhETF Pisma Redaktsiiu*, vol. 3, p. 471, June 1966.

[32] L. A. Ostrovskii, “Propagation of wave packets and space-time self-focusing in a nonlinear medium,” *soviets physics JETP*, vol. 24, pp. 797–800, Apr. 1967.

[33] A. Hasegawa and W. Brinkman, “Tunable coherent IR and FIR sources utilizing modulational instability,” *IEEE Journal of Quantum Electronics*, vol. 16, pp. 694–697, July 1980.

[34] K. Tai, A. Hasegawa, and A. Tomita, “Observation of modulational instability in optical fibers,” *Physical Review Letters*, vol. 56, pp. 135–138, Jan. 1986.

[35] K. Tai, A. Tomita, J. L. Jewell, and A. Hasegawa, “Generation of subpicosecond solitonlike optical pulses at 0.3 THz repetition rate by induced modulational instability,” *Applied Physics Letters*, vol. 49, pp. 236–238, Aug. 1986.

[36] J. M. Dudley, G. Genty, and S. Coen, “Supercontinuum generation in photonic crystal fiber,” *Reviews of Modern Physics*, vol. 78, pp. 1135–1184, Oct. 2006.

[37] D. H. Peregrine, “Water waves, nonlinear Schrödinger equations and their solutions,” *The ANZIAM Journal*, vol. 25, pp. 16–43, July 1983.

[38] N. Akhmediev, B. Kibler, F. Baronio, M. Belić, W.-P. Zhong, Y. Zhang, W. Chang, J. M. Soto-Crespo, P. Vouzas, P. Grelu, C. Lecaplain, K. Hammani, S. Rica, A. Picozzi, M. Tlidi, K. Panajotov, A. Mussot, A. Bendahmane, P. Szriftgiser, G. Genty, J. Dudley, A. Kudlinski, A. Demircan, U. Morgner, S. Amiraranashvili, C. Bree, G. Steinmeyer, C. Masoller, N. G. R. Broderick, A. F. J. Runge, M. Erkintalo, S. Residori, U. Bortolozzo, F. T. Arecchi,

S. Wabnitz, C. G. Tiofack, S. Coulibaly, and M. Taki, "Roadmap on optical rogue waves and extreme events," *Journal of Optics*, vol. 18, p. 063001, Apr. 2016.

[39] K. Ikeda and O. Akimoto, "Instability Leading to Periodic and Chaotic Self-Pulsations in a Bistable Optical Cavity," *Physical Review Letters*, vol. 48, pp. 617–620, Mar. 1982.

[40] H. Gibbs, *Optical Bistability: Controlling Light With Light.* Elsevier, Dec. 2012.

[41] H. Nakatsuka, S. Asaka, H. Itoh, K. Ikeda, and M. Matsuoka, "Observation of Bifurcation to Chaos in an All-Optical Bistable System," *Physical Review Letters*, vol. 50, no. 2, pp. 109–112, 1983.

[42] K. Nozaki and N. Bekki, "Chaos in a Perturbed Nonlinear Schrödinger Equation," *Physical Review Letters*, vol. 50, pp. 1226–1229, Apr. 1983.

[43] K. J. Blow and N. J. Doran, "Global and Local Chaos in the Pumped Nonlinear Schrödinger Equation," *Physical Review Letters*, vol. 52, pp. 526–529, Feb. 1984.

[44] K. Ikeda, "Multiple-valued stationary state and its instability of the transmitted light by a ring cavity system," *Optics Communications*, vol. 30, pp. 257–261, Aug. 1979.

[45] K. Ikeda, H. Daido, and O. Akimoto, "Optical Turbulence: Chaotic Behavior of Transmitted Light from a Ring Cavity," *Physical Review Letters*, vol. 45, pp. 709–712, Sept. 1980.

[46] J. Goldstone and E. Garmire, "On the dynamic response of nonlinear Fabry-Perot interferometers," *IEEE Journal of Quantum Electronics*, vol. 17, pp. 366–374, Mar. 1981.

[47] J. L. Jewell, H. M. Gibbs, S. S. Tarng, A. C. Gossard, and W. Wiegmann, "Regenerative pulsations from an intrinsic bistable optical device," *Applied Physics Letters*, vol. 40, pp. 291–293, Feb. 1982.

[48] B. Wedding, A. Gasch, and D. Jäger, "Self-pulsing and transients of a Fabry–Perot interferometer with quadratic nonlinear medium," *Journal of Applied Physics*, vol. 54, pp. 4826–4831, Sept. 1983.

[49] R. M. Shelby, M. D. Levenson, and S. H. Perlmutter, "Bistability and other effects in a nonlinear fiber-optic ring resonator," *JOSA B*, vol. 5, pp. 347–357, Feb. 1988.

[50] R. Vallée, "Temporal instabilities in the output of an all-fiber ring cavity," *Optics Communications*, vol. 81, pp. 419–426, Mar. 1991.

[51] S. Coen and M. Haelterman, “Modulational Instability Induced by Cavity Boundary Conditions in a Normally Dispersive Optical Fiber,” *Physical Review Letters*, vol. 79, pp. 4139–4142, Nov. 1997.

[52] S. Coen, M. Haelterman, P. Emplit, L. Delage, L. M. Simohamed, and F. Reynaud, “Experimental investigation of the dynamics of a stabilized nonlinear fiber ring resonator,” *JOSA B*, vol. 15, pp. 2283–2293, Aug. 1998.

[53] S. Coen, M. Haelterman, P. Emplit, L. Delage, L. M. Simohamed, and François Reynaud, “Bistable switching induced by modulational instability in a normally dispersive all-fibre ring cavity,” *Journal of Optics B: Quantum and Semiclassical Optics*, vol. 1, no. 1, p. 36, 1999.

[54] S. Coen and M. Haelterman, “Competition between modulational instability and switching in optical bistability,” *Optics Letters*, vol. 24, pp. 80–82, Jan. 1999.

[55] S. Coen and M. Haelterman, “Continuous-wave ultrahigh-repetition-rate pulse-train generation through modulational instability in a passive fiber cavity,” *Optics Letters*, vol. 26, pp. 39–41, Jan. 2001.

[56] F. Leo, S. Coen, P. Kockaert, S.-P. Gorza, P. Emplit, and M. Haelterman, “Temporal cavity solitons in one-dimensional Kerr media as bits in an all-optical buffer,” *Nature Photonics*, vol. 4, pp. 471–476, July 2010.

[57] G. S. McDonald and W. J. Firth, “All-optical Switching in a Nonlinear Resonator,” *Journal of Modern Optics*, vol. 37, pp. 613–626, Apr. 1990.

[58] P. Del’Haye, T. Herr, E. Gavartin, M. L. Gorodetsky, R. Holzwarth, and T. J. Kippenberg, “Octave Spanning Tunable Frequency Comb from a Microresonator,” *Physical Review Letters*, vol. 107, p. 063901, Aug. 2011.

[59] Y. Okawachi, K. Saha, J. S. Levy, Y. H. Wen, M. Lipson, and A. L. Gaeta, “Octave-spanning frequency comb generation in a silicon nitride chip,” *Optics Letters*, vol. 36, pp. 3398–3400, Sept. 2011.

[60] T. Udem, R. Holzwarth, and T. W. Hänsch, “Optical frequency metrology,” *Nature*, vol. 416, p. 233, Mar. 2002.

[61] I. Coddington, W. C. Swann, L. Nenadovic, and N. R. Newbury, “Rapid and precise absolute distance measurements at long range,” *Nature Photonics*, vol. 3, pp. 351–356, June 2009.

[62] P. Trocha, M. Karpov, D. Ganin, M. H. P. Pfeiffer, A. Kordts, S. Wolf, J. Krockenberger, P. Marin-Palomo, C. Weimann, S. Randel, W. Freude, T. J. Kippenberg, and C. Koos, “Ultrafast optical ranging using microresonator soliton frequency combs,” *Science*, vol. 359, pp. 887–891, Feb. 2018.

[63] E. Obrzud, M. Rainer, A. Harutyunyan, M. H. Anderson, J. Liu, M. Geiselmann, B. Chazelas, S. Kundermann, S. Lecomte, M. Cecconi, A. Ghedina, E. Molinari, F. Pepe, F. Wildi, F. Bouchy, T. J. Kippenberg, and T. Herr, "A microphotonic astrocomb," *Nature Photonics*, vol. 13, p. 31, Jan. 2019.

[64] T. Steinmetz, T. Wilken, C. Araujo-Hauck, R. Holzwarth, T. W. Hänsch, L. Pasquini, A. Manescau, S. D'Odorico, M. T. Murphy, T. Kentischer, W. Schmidt, and T. Udem, "Laser Frequency Combs for Astronomical Observations," *Science*, vol. 321, pp. 1335–1337, Sept. 2008.

[65] I. Coddington, N. Newbury, and W. Swann, "Dual-comb spectroscopy," *Optica*, vol. 3, pp. 414–426, Apr. 2016.

[66] T. W. Hänsch, "Nobel Lecture: Passion for precision," *Reviews of Modern Physics*, vol. 78, pp. 1297–1309, Nov. 2006.

[67] H. Timmers, A. Kowligy, A. Lind, F. C. Cruz, N. Nader, M. Silfies, G. Ycas, T. K. Allison, P. G. Schunemann, S. B. Papp, and S. A. Diddams, "Molecular fingerprinting with bright, broadband infrared frequency combs," *Optica*, vol. 5, pp. 727–732, June 2018.

[68] T. Hansson, D. Modotto, and S. Wabnitz, "Dynamics of the modulational instability in microresonator frequency combs," *Physical Review A*, vol. 88, p. 023819, Aug. 2013.

[69] H. Bao, A. Cooper, M. Rowley, L. D. Lauro, J. S. T. Gongora, S. T. Chu, B. E. Little, G.-L. Oppo, R. Morandotti, D. J. Moss, B. Wetzel, M. Peccianti, and A. Pasquazi, "Laser cavity-soliton microcombs," *Nature Photonics*, vol. 13, pp. 384–389, June 2019.

[70] A. Pasquazi, M. Peccianti, L. Razzari, D. J. Moss, S. Coen, M. Erkintalo, Y. K. Chembo, T. Hansson, S. Wabnitz, P. Del'Haye, X. Xue, A. M. Weiner, and R. Morandotti, "Micro-combs: A novel generation of optical sources," *Physics Reports*, vol. 729, pp. 1–81, Jan. 2018.

[71] X. Yi, Q.-F. Yang, K. Y. Yang, and K. Vahala, "Imaging soliton dynamics in optical microcavities," *Nature Communications*, vol. 9, p. 3565, Sept. 2018.

[72] T. Herr, V. Brasch, J. D. Jost, C. Y. Wang, N. M. Kondratiev, M. L. Gorodetsky, and T. J. Kippenberg, "Temporal solitons in optical microresonators," *Nature Photonics*, vol. 8, pp. 145–152, Feb. 2014.

[73] P. Chakrabarti, *Optical Fiber Communication.* McGraw-Hill Education, 2015.

[74] S. Miller, *Optical Fiber Telecommunications.* Elsevier, Dec. 2012.

[75] G. P. Agrawal, *Nonlinear Fiber Optics.* Academic Press, 2007.

[76] Y. Tamura, H. Sakuma, K. Morita, M. Suzuki, Y. Yamamoto, K. Shimada, Y. Honma, K. Sohma, T. Fujii, and T. Hasegawa, "The First 0.14-dB/km Loss Optical Fiber and its Impact on Submarine Transmission," *Journal of Lightwave Technology*, vol. 36, pp. 44–49, Jan. 2018.

[77] R. L. Sutherland, *Handbook of Nonlinear Optics*. CRC Press, Apr. 2003.

[78] R. W. Boyd, *Nonlinear Optics*. Elsevier, May 2008.

[79] P. Russell, "Photonic Crystal Fibers," *Science*, vol. 299, pp. 358–362, Jan. 2003.

[80] J. Fatome, C. Fortier, T. N. Nguyen, T. Chartier, F. Smektala, K. Messaad, B. Kibler, S. Pitois, G. Gadret, C. Finot, J. Troles, F. Desevedavy, P. Houizot, G. Renversez, L. Brilland, and N. Traynor, "Linear and Nonlinear Characterizations of Chalcogenide Photonic Crystal Fibers," *Journal of Lightwave Technology*, vol. 27, pp. 1707–1715, June 2009.

[81] G. Agrawal, *Applications of Nonlinear Fiber Optics*. Elsevier, Jan. 2001.

[82] L. A. Lugiato and R. Lefever, "Spatial Dissipative Structures in Passive Optical Systems," *Physical Review Letters*, vol. 58, pp. 2209–2211, May 1987.

[83] A. E. Siegman, *Lasers*. University Science Books, 1986.

[84] M. Anderson, Y. Wang, F. Leo, S. Coen, M. Erkintalo, and S. G. Murdoch, "Coexistence of Multiple Nonlinear States in a Tristable Passive Kerr Resonator," *Physical Review X*, vol. 7, p. 031031, Aug. 2017.

[85] M. Conforti and F. Biancalana, "Multi-resonant Lugiato-Lefever model," *Optics Letters*, vol. 42, pp. 3666–3669, Sept. 2017.

[86] M. Haelterman, S. Trillo, and S. Wabnitz, "Dissipative modulation instability in a nonlinear dispersive ring cavity," *Optics Communications*, vol. 91, pp. 401–407, Aug. 1992.

[87] M. Haelterman, S. Trillo, and S. Wabnitz, "Additive-modulation-instability ring laser in the normal dispersion regime of a fiber," *Optics Letters*, vol. 17, pp. 745–747, May 1992.

[88] J. E. Rothenberg, "Modulational instability for normal dispersion," *Physical Review A*, vol. 42, pp. 682–685, July 1990.

[89] S. Pitois and G. Millot, "Experimental observation of a new modulational instability spectral window induced by fourth-order dispersion in a normally dispersive single-mode optical fiber," *Optics Communications*, vol. 226, pp. 415–422, Oct. 2003.

[90] M. Nakazawa, K. Suzuki, and H. A. Haus, "Modulational instability oscillation in nonlinear dispersive ring cavity," *Physical Review A*, vol. 38, pp. 5193–5196, Nov. 1988.

[91] T. J. Kippenberg, A. L. Gaeta, M. Lipson, and M. L. Gorodetsky, "Dissipative Kerr solitons in optical microresonators," *Science*, vol. 361, p. eaan8083, Aug. 2018.

[92] A. J. Scroggie, W. J. Firth, G. S. McDonald, M. Tlidi, R. Lefever, and L. A. Lugiato, "Pattern formation in a passive Kerr cavity," *Chaos, Solitons & Fractals*, vol. 4, pp. 1323–1354, Aug. 1994.

[93] F. Copie, *Modulation instabilities in dispersion oscillating passive fiber-ring cavities.* thesis, Lille 1, Oct. 2017.

[94] A. Kobyakov, M. Sauer, and D. Chowdhury, "Stimulated Brillouin scattering in optical fibers," *Advances in Optics and Photonics*, vol. 2, pp. 1–59, Mar. 2010.

[95] L. B. Jeunhomme, *Single-Mode Fiber Optics: Prinicples and Applications, Second Edition,.* Routledge, July 2019.

[96] F. Copie, M. Conforti, A. Kudlinski, A. Mussot, and S. Trillo, "Competing Turing and Faraday Instabilities in Longitudinally Modulated Passive Resonators," *Physical Review Letters*, vol. 116, p. 143901, Apr. 2016.

[97] F. Copie, M. Conforti, A. Kudlinski, S. Trillo, and A. Mussot, "Modulation instability in the weak dispersion regime of a dispersion modulated passive fiber-ring cavity," *Optics Express*, vol. 25, pp. 11283–11296, May 2017.

[98] F. Copie, M. Conforti, A. Kudlinski, S. Trillo, and A. Mussot, "Dynamics of Turing and Faraday instabilities in a longitudinally modulated fiber-ring cavity," *Optics Letters*, vol. 42, pp. 435–438, Feb. 2017.

[99] K. Goda and B. Jalali, "Dispersive Fourier transformation for fast continuous single-shot measurements," *Nature Photonics*, vol. 7, p. 102, Feb. 2013.

[100] J. Hammer, P. Hosseini, C. R. Menyuk, P. S. J. Russell, and N. Y. Joly, "Single-shot reconstruction of spectral amplitude and phase in a fiber ring cavity at a 80 MHz repetition rate," *Optics Letters*, vol. 41, pp. 4641–4644, Oct. 2016.

[101] B. H. Kolner and M. Nazarathy, "Temporal imaging with a time lens," *Optics Letters*, vol. 14, pp. 630–632, June 1989.

[102] R. Salem, M. A. Foster, and A. L. Gaeta, "Application of space-time duality to ultrahigh-speed optical signal processing," *Advances in Optics and Photonics*, vol. 5, pp. 274–317, Sept. 2013.

[103] M. A. Foster, R. Salem, D. F. Geraghty, A. C. Turner-Foster, M. Lipson, and A. L. Gaeta, “Silicon-chip-based ultrafast optical oscilloscope,” *Nature*, vol. 456, pp. 81–84, Nov. 2008.

[104] A. Mussot, A. Kudlinski, E. Louvergneaux, M. Kolobov, and M. Taki, “Impact of the third-order dispersion on the modulation instability gain of pulsed signals,” *Optics Letters*, vol. 35, pp. 1194–1196, Apr. 2010.

[105] F. Leo, S. Coen, P. Kockaert, P. Emplit, M. Haelterman, A. Mussot, and M. Taki, “Impact of third-order dispersion on nonlinear bifurcations in optical resonators,” *Physics Letters A*, vol. 379, pp. 1934–1937, Sept. 2015.

[106] J. K. Jang, M. Erkintalo, S. G. Murdoch, and S. Coen, “Observation of dispersive wave emission by temporal cavity solitons,” *Optics Letters*, vol. 39, pp. 5503–5506, Oct. 2014.

[107] S. B. Cavalcanti, J. C. Cressoni, H. R. da Cruz, and A. S. Gouveia-Neto, “Modulation instability in the region of minimum group-velocity dispersion of single-mode optical fibers via an extended nonlinear Schrödinger equation,” *Physical Review A*, vol. 43, pp. 6162–6165, June 1991.

[108] J. D. Harvey, R. Leonhardt, S. Coen, G. K. L. Wong, J. Knight, W. J. Wadsworth, and P. S. J. Russell, “Scalar modulation instability in the normal dispersion regime by use of a photonic crystal fiber,” *Optics Letters*, vol. 28, pp. 2225–2227, Nov. 2003.

[109] M. Tlidi, A. Mussot, E. Louvergneaux, G. Kozyreff, A. G. Vladimirov, and M. Taki, “Control and removal of modulational instabilities in low-dispersion photonic crystal fiber cavities,” *Optics Letters*, vol. 32, p. 662, Mar. 2007.

[110] N. L. B. Sayson, K. E. Webb, S. Coen, M. Erkintalo, and S. G. Murdoch, “Widely tunable optical parametric oscillation in a Kerr microresonator,” *Optics Letters*, vol. 42, pp. 5190–5193, Dec. 2017.

[111] N. L. B. Sayson, H. Pham, K. E. Webb, V. Ng, L. S. Trainor, H. G. L. Schwefel, S. Coen, M. Erkintalo, and S. G. Murdoch, “Origins of clustered frequency combs in Kerr microresonators,” *Optics Letters*, vol. 43, pp. 4180–4183, Sept. 2018.

[112] S. Coen, H. G. Randle, T. Sylvestre, and M. Erkintalo, “Modeling of octave-spanning Kerr frequency combs using a generalized mean-field Lugiato–Lefever model,” *Optics Letters*, vol. 38, p. 37, Jan. 2013.

[113] F. Leo, A. Mussot, P. Kockaert, P. Emplit, M. Haelterman, and M. Taki, “Nonlinear Symmetry Breaking Induced by Third-Order Dispersion in Optical Fiber Cavities,” *Physical Review Letters*, vol. 110, p. 104103, Mar. 2013.

[114] A. Mussot, E. Louvergneaux, N. Akhmediev, F. Reynaud, L. Delage, and M. Taki, “Optical Fiber Systems Are Convectively Unstable,” *Physical Review Letters*, vol. 101, no. 11, 2008.

[115] F. Bessin, F. Copie, M. Conforti, A. Kudlinski, and A. Mussot, “Modulation instability in the weak normal dispersion region of passive fiber ring cavities,” *Optics Letters*, vol. 42, pp. 3730–3733, Oct. 2017.

[116] T. Hansson and S. Wabnitz, “Frequency comb generation beyond the Lugiato-Lefever equation: multi-stability and super cavity solitons,” *JOSA B*, vol. 32, pp. 1259–1266, July 2015.

[117] T. Hansson, M. Bernard, and S. Wabnitz, “Modulational instability of nonlinear polarization mode coupling in microresonators,” *JOSA B*, vol. 35, pp. 835–841, Apr. 2018.

[118] J. Fatome, B. Kibler, F. Leo, A. Bendahmane, G.-L. Oppo, B. Garbin, Y. Wang, S. G. Murdoch, M. Erkintalo, and S. Coen, “Polarization modulation instability in a fiber Kerr resonator,” in *Advanced Photonics 2018 (BGPP, IPR, NP, NOMA, Sensors, Networks, SPPCom, SOF) (2018), paper NpTu4C.6*, p. NpTu4C.6, Optical Society of America, July 2018.

[119] M. Conforti, A. Mussot, A. Kudlinski, and S. Trillo, “Modulational instability in dispersion oscillating fiber ring cavities,” *Optics Letters*, vol. 39, p. 4200, July 2014.

[120] M. Conforti, F. Copie, A. Mussot, A. Kudlinski, and S. Trillo, “Parametric instabilities in modulated fiber ring cavities,” *Optics Letters*, vol. 41, pp. 5027–5030, Nov. 2016.

[121] M. Anderson, Y. Wang, F. Leo, S. Coen, M. Erkintalo, and S. G. Murdoch, “Coexistence of Multiple Nonlinear States in a Tristable Passive Kerr Resonator,” *Physical Review X*, vol. 7, p. 031031, Aug. 2017.

[122] K. Staliunas, C. Hang, and V. V. Konotop, “Parametric patterns in optical fiber ring nonlinear resonators,” *Physical Review A*, vol. 88, p. 023846, Aug. 2013.

[123] M. Haelterman, “Simple model for the study of period-doubling instabilities in the nonlinear ring cavity,” *Applied Physics Letters*, vol. 61, pp. 2756–2758, Dec. 1992.

[124] A. Ankiewicz and C. Pask, “Chaos in optics: field fluctuations for a nonlinear optical fibre loop closed by a coupler,” *The ANZIAM Journal*, vol. 29, pp. 1–20, July 1987.

[125] M. Haelterman, “Ikeda instability and transverse effects in nonlinear ring resonators,” *Optics Communications*, vol. 100, pp. 389–398, July 1993.

[126] D. W. McLaughlin, J. V. Moloney, and A. C. Newell, “New Class of Instabilities in Passive Optical Cavities,” *Physical Review Letters*, vol. 54, pp. 681–684, Feb. 1985.

[127] D. A. Zezyulin, V. V. Konotop, and M. Taki, “Modulational instability in a passive fiber cavity, revisited,” *Optics Letters*, vol. 36, pp. 4623–4625, Dec. 2011.

[128] T. Hansson and S. Wabnitz, “Frequency comb generation beyond the Lugiato–Lefever equation: multi-stability and super cavity solitons,” *JOSA B*, vol. 32, pp. 1259–1266, July 2015.

[129] G. Steinmeyer, D. Jaspert, and F. Mitschke, “Observation of a period-doubling sequence in a nonlinear optical fiber ring cavity near zero dispersion,” *Optics Communications*, vol. 104, pp. 379–384, Jan. 1994.

[130] N. Akhmediev, J. M. Soto-Crespo, and G. Town, “Pulsating solitons, chaotic solitons, period doubling, and pulse coexistence in mode-locked lasers: Complex Ginzburg-Landau equation approach,” *Physical Review E*, vol. 63, p. 056602, Apr. 2001.

[131] S. Boscolo, S. K. Turitsyn, and C. Finot, “Amplifier similariton fiber laser with nonlinear spectral compression,” *Optics Letters*, vol. 37, pp. 4531–4533, Nov. 2012.

[132] F. Li, P. K. A. Wai, and J. N. Kutz, “Geometrical description of the onset of multi-pulsing in mode-locked laser cavities,” *JOSA B*, vol. 27, pp. 2068–2077, Oct. 2010.

[133] L. Luo, T. J. Tee, and P. L. Chu, “Chaotic behavior in erbium-doped fiber-ring lasers,” *JOSA B*, vol. 15, pp. 972–978, Mar. 1998.

[134] G. Sucha, S. R. Bolton, S. Weiss, and D. S. Chemla, “Period doubling and quasi-periodicity in additive-pulse mode-locked lasers,” *Optics Letters*, vol. 20, pp. 1794–1796, Sept. 1995.

[135] P. Suret, R. E. Koussaifi, A. Tikan, C. Evain, S. Randoux, C. Szwaj, and S. Bielawski, “Single-shot observation of optical rogue waves in integrable turbulence using time microscopy,” *Nature Communications*, vol. 7, p. 13136, Oct. 2016.

[136] M. Närhi, B. Wetzel, C. Billet, S. Toenger, T. Sylvestre, J.-M. Merolla, R. Morandotti, F. Dias, G. Genty, and J. M. Dudley, “Real-time measurements of spontaneous breathers and rogue wave events in optical fibre modulation instability,” *Nature Communications*, vol. 7, p. 13675, Dec. 2016.

[137] P. Ryczkowski, M. Närhi, C. Billet, J.-M. Merolla, G. Genty, and J. M. Dudley, “Real-time full-field characterization of transient dissipative soliton dynamics in a mode-locked laser,” *Nature Photonics*, vol. 12, pp. 221–227, Apr. 2018.

[138] A. Nayfeh and D. Mook, *Nonlinear Oscillations.* Wiley Classics Library, Wiley, 2008.

[139] H. Adachihara, D. W. McLaughlin, J. V. Moloney, and A. C. Newell, "Solitary waves as fixed points of infinite-dimensional maps for an optical bistable ring cavity: Analysis," *Journal of Mathematical Physics*, vol. 29, pp. 63–85, Jan. 1988.

[140] S. Coulibaly, M. Taki, A. Bendahmane, G. Millot, B. Kibler, and M. G. Clerc, "Turbulence-induced rogue waves in Kerr resonators," *Physical Review X*, vol. 9, p. 011054, Mar. 2019. arXiv: 1901.02833.

[141] D. J. Jones, S. A. Diddams, J. K. Ranka, A. Stentz, R. S. Windeler, J. L. Hall, and S. T. Cundiff, "Carrier-Envelope Phase Control of Femtosecond Mode-Locked Lasers and Direct Optical Frequency Synthesis," *Science*, vol. 288, pp. 635–639, Apr. 2000.

[142] A. Hugi, G. Villares, S. Blaser, H. C. Liu, and J. Faist, "Mid-infrared frequency comb based on a quantum cascade laser," *Nature*, vol. 492, pp. 229–233, Dec. 2012.

[143] E. Myslivets, B. P. P. Kuo, N. Alic, and S. Radic, "Generation of wideband frequency combs by continuous-wave seeding of multistage mixers with synthesized dispersion," *Optics Express*, vol. 20, pp. 3331–3344, Jan. 2012.

[144] M. Zimmermann, C. Gohle, R. Holzwarth, T. Udem, and T. W. Hänsch, "Optical clockwork with an offset-free difference-frequency comb: accuracy of sum- and difference-frequency generation," *Optics Letters*, vol. 29, pp. 310–312, Feb. 2004.

[145] I. Ricciardi, S. Mosca, M. Parisi, P. Maddaloni, L. Santamaria, P. De Natale, and M. De Rosa, "Frequency comb generation in quadratic nonlinear media," *Physical Review A*, vol. 91, p. 063839, June 2015.

[146] T. J. Kippenberg, R. Holzwarth, and S. A. Diddams, "Microresonator-Based Optical Frequency Combs," *Science*, vol. 332, pp. 555–559, Apr. 2011.

[147] P. Del'Haye, A. Schliesser, O. Arcizet, T. Wilken, R. Holzwarth, and T. J. Kippenberg, "Optical frequency comb generation from a monolithic microresonator," *Nature*, vol. 450, pp. 1214–1217, Dec. 2007.

[148] A. G. Griffith, R. K. W. Lau, J. Cardenas, Y. Okawachi, A. Mohanty, R. Fain, Y. H. D. Lee, M. Yu, C. T. Phare, C. B. Poitras, A. L. Gaeta, and M. Lipson, "Silicon-chip mid-infrared frequency comb generation," *Nature Communications*, vol. 6, p. 6299, Feb. 2015.

[149] K. J. Vahala, "Optical microcavities," *Nature*, vol. 424, p. 839, Aug. 2003.

[150] T. J. Kippenberg, S. M. Spillane, and K. J. Vahala, "Kerr-Nonlinearity Optical Parametric Oscillation in an Ultrahigh-Q Toroid Microcavity," *Physical Review Letters*, vol. 93, p. 083904, Aug. 2004.

[151] A. A. Savchenkov, A. B. Matsko, D. Strekalov, M. Mohageg, V. S. Ilchenko, and L. Maleki, "Low Threshold Optical Oscillations in a Whispering Gallery Mode CaF_2 Resonator," *Physical Review Letters*, vol. 93, p. 243905, Dec. 2004.

[152] S. H. Lee, D. Y. Oh, Q.-F. Yang, B. Shen, H. Wang, K. Y. Yang, Y.-H. Lai, X. Yi, X. Li, and K. Vahala, "Towards visible soliton microcomb generation," *Nature Communications*, vol. 8, p. 1295, Nov. 2017.

[153] S. B. Papp, K. Beha, P. Del'Haye, F. Quinlan, H. Lee, K. J. Vahala, and S. A. Diddams, "Microresonator frequency comb optical clock," *Optica*, vol. 1, pp. 10–14, July 2014.

[154] M. Yu, Y. Okawachi, A. G. Griffith, M. Lipson, and A. L. Gaeta, "Mode-locked mid-infrared frequency combs in a silicon microresonator," *Optica*, vol. 3, pp. 854–860, Aug. 2016.

[155] F. Castelli, M. Brambilla, A. Gatti, F. Prati, and L. A. Lugiato, "The LLE, pattern formation and a novel coherent source," *The European Physical Journal D*, vol. 71, p. 84, Apr. 2017.

[156] Y. K. Chembo and C. R. Menyuk, "Spatiotemporal Lugiato-Lefever formalism for Kerr-comb generation in whispering-gallery-mode resonators," *Physical Review A*, vol. 87, p. 053852, May 2013.

[157] X. Yi, Q.-F. Yang, K. Y. Yang, M.-G. Suh, and K. Vahala, "Soliton frequency comb at microwave rates in a high-Q silica microresonator," *Optica*, vol. 2, pp. 1078–1085, Dec. 2015.

[158] S.-W. Huang, A. K. Vinod, J. Yang, M. Yu, D.-L. Kwong, and C. W. Wong, "Quasi-phase-matched multispectral Kerr frequency comb," *Optics Letters*, vol. 42, pp. 2110–2113, June 2017.

[159] X. Xue, Y. Xuan, Y. Liu, P.-H. Wang, S. Chen, J. Wang, D. E. Leaird, M. Qi, and A. M. Weiner, "Mode-locked dark pulse Kerr combs in normal-dispersion microresonators," *Nature Photonics*, vol. 9, pp. 594–600, Sept. 2015.

[160] P. Parra-Rivas, E. Knobloch, D. Gomila, and L. Gelens, "Dark solitons in the Lugiato-Lefever equation with normal dispersion," *Physical Review A*, vol. 93, p. 063839, June 2016.

[161] A. M. Perego, S. K. Turitsyn, and K. Staliunas, "Gain through losses in nonlinear optics," *Light: Science & Applications*, vol. 7, p. 43, Aug. 2018.

[162] T. Tanemura, Y. Ozeki, and K. Kikuchi, “Modulational Instability and Parametric Amplification Induced by Loss Dispersion in Optical Fibers,” *Physical Review Letters*, vol. 93, p. 163902, Oct. 2004.

[163] V. Lucarini, J. J. Saarinen, K.-E. Peiponen, and E. M. Vartiainen, *Kramers-Kronig Relations in Optical Materials Research.* Springer Science & Business Media, Apr. 2005.

[164] J. Bechhoefer, “Kramers–Kronig, Bode, and the meaning of zero,” *American Journal of Physics*, vol. 79, pp. 1053–1059, Sept. 2011.

[165] M. Feldman, *Hilbert Transform Applications in Mechanical Vibration.* John Wiley & Sons, Mar. 2011.

[166] P. Del’Haye, A. Coillet, W. Loh, K. Beha, S. B. Papp, and S. A. Diddams, “Phase steps and resonator detuning measurements in microresonator frequency combs,” *Nature Communications*, vol. 6, p. 5668, Jan. 2015.

[167] B. Yao, S.-W. Huang, Y. Liu, A. K. Vinod, C. Choi, M. Hoff, Y. Li, M. Yu, Z. Feng, D.-L. Kwong, Y. Huang, Y. Rao, X. Duan, and C. W. Wong, “Gate-tunable frequency combs in graphene–nitride microresonators,” *Nature*, vol. 558, p. 410, June 2018.

[168] M. Zhang, B. Buscaino, C. Wang, A. Shams-Ansari, C. Reimer, R. Zhu, J. M. Kahn, and M. Lončar, “Broadband electro-optic frequency comb generation in a lithium niobate microring resonator,” *Nature*, vol. 568, p. 373, Apr. 2019.

[169] T. Hansson and S. Wabnitz, “Bichromatically pumped microresonator frequency combs,” *Physical Review A*, vol. 90, p. 013811, July 2014.

[170] G. Lin, R. Martinenghi, S. Diallo, K. Saleh, A. Coillet, and Y. K. Chembo, “Spectro-temporal dynamics of Kerr combs with parametric seeding,” *Applied Optics*, vol. 54, pp. 2407–2412, Mar. 2015.

[171] C. Bao, P. Liao, A. Kordts, L. Zhang, M. Karpov, M. H. P. Pfeiffer, Y. Cao, Y. Yan, A. Almaiman, G. Xie, A. Mohajerin-Ariaei, L. Li, M. Ziyadi, S. R. Wilkinson, M. Tur, T. J. Kippenberg, and A. E. Willner, “Dual-pump generation of high-coherence primary Kerr combs with multiple sub-lines,” *Optics Letters*, vol. 42, pp. 595–598, Feb. 2017.

[172] S. B. Papp, P. Del’Haye, and S. A. Diddams, “Parametric seeding of a microresonator optical frequency comb,” *Optics Express*, vol. 21, pp. 17615–17624, July 2013.

[173] A. Bendahmane, J. Fatome, C. Finot, G. Millot, and B. Kibler, “Selective generation of Kerr combs induced by asymmetrically phase-detuned dual pumping of a fiber ring cavity,” *Optics Letters*, vol. 43, pp. 4449–4452, Sept. 2018.

[174] A. Bendahmane, J. Fatome, C. Finot, G. Millot, and B. Kibler, “Coherent and incoherent seeding of dissipative modulation instability in a nonlinear fiber ring cavity,” *Optics Letters*, vol. 42, pp. 251–254, Jan. 2017.

[175] A. Fülöp, C. J. Krückel, D. Castelló-Lurbe, E. Silvestre, and V. Torres-Company, “Triply resonant coherent four-wave mixing in silicon nitride microresonators,” *Optics Letters*, vol. 40, pp. 4006–4009, Sept. 2015.

[176] A. Mussot, C. Naveau, M. Conforti, A. Kudlinski, F. Copie, P. Szriftgiser, and S. Trillo, “Fibre multi-wave mixing combs reveal the broken symmetry of Fermi–Pasta–Ulam recurrence,” *Nature Photonics*, p. 1, Apr. 2018.

[177] S. Trillo, S. Wabnitz, and T. A. B. Kennedy, “Nonlinear dynamics of dual-frequency-pumped multiwave mixing in optical fibers,” *Physical Review A*, vol. 50, pp. 1732–1747, Aug. 1994.

[178] S. Coen, *Passive nonlinear optical fiber resonators: fundamentals and applications.* thesis, ULB, 1999.

[179] M. Tabor, *Chaos and integrability in nonlinear dynamics: an introduction.* Wiley, 1989.

[180] F. Friederich, G. Schuricht, A. Deninger, F. Lison, G. Spickermann, P. H. Bolívar, and H. G. Roskos, “Phase-locking of the beat signal of two distributed-feedback diode lasers to oscillators working in the MHz to THz range,” *Optics Express*, vol. 18, pp. 8621–8629, Apr. 2010.

[181] S. Coen, M. Tlidi, P. Emplit, and M. Haelterman, “Convection versus Dispersion in Optical Bistability,” *Physical Review Letters*, vol. 83, no. 12, pp. 2328–2331, 1999.

[182] T. I. Kuznetsova, “On the phase retrieval problem in optics,” *Soviet Physics Uspekhi*, vol. 31, no. 4, p. 364, 1988.

[183] E. N. Lorenz, “Deterministic Nonperiodic Flow,” *Journal of the Atmospheric Sciences*, vol. 20, pp. 130–141, Mar. 1963.

[184] H. Haken, “Analogy between higher instabilities in fluids and lasers,” *Physics Letters A*, vol. 53, pp. 77–78, May 1975.

[185] C. O. Weiss, N. B. Abraham, and U. Hübner, “Homoclinic and Heteroclinic Chaos in a Single-Mode Laser,” *Physical Review Letters*, vol. 61, pp. 1587–1590, Oct. 1988.

[186] M. Virte, K. Panajotov, H. Thienpont, and M. Sciamanna, “Deterministic polarization chaos from a laser diode,” *Nature Photonics*, vol. 7, pp. 60–65, Jan. 2013.

[187] M. Haelterman, S. Trillo, and S. Wabnitz, "Low dimensional modulational chaos in diffractive nonlinear cavities," *Optics Communications*, vol. 93, pp. 343–349, Oct. 1992.

Author's bibliography

Publications in peer-reviewed journals

- **F. Bessin**, F. Copie, M. Conforti, A. Kudlinski, A. Mussot, and S. Trillo, "Real-Time Characterization of period-doubling dynamics in uniform and dispersion oscillating fiber ring cavities", *Phys. Rev. X*, **9**, 041030 (2019).
- **F. Bessin**, A. M. Perego, K. Staliunas, S. K. Turitsyn, A. Kudlinski, M. Conforti, and A. Mussot, "Gain-through-filtering enables tuneable frequency comb generation in passive optical resonators", *Nat Commun*, **10**, 1 (2019)
- **F. Bessin**, F. Copie, M. Conforti, A. Kudlinski, and A. Mussot, "Modulation instability in the weak normal dispersion region of passive fiber ring cavities", *Opt. Lett*, **42**, 3730–3733 (2017).
- C. Mas Arabí, **F. Bessin**, A. Kudlinski, A. Mussot, D. Skryabin, and M. Conforti, "Efficiency of four-wave mixing between orthogonally polarized linear waves and solitons in a birefringent fiber", *Phys. Rev. A*, **94**, 063847 (2016).

Orals in peer-reviewed national conferences

- **F. Bessin**, F. Copie, M. Conforti, A. Kudlinski, and A. Mussot. "Instabilité de modulation dans un cavité fibrée monostable en régime de dispersion normale", Journée Nationales de l'Optique Guidée, Limoges, France (2017)

Orals in peer-reviewed international conference

- C. M. Arabi, **F. Bessin**, A. Mussot, A. Kudlinski, and D. V. Skryabin, "Conversion efficiency of vector scattering between solitons and dispersive waves", Photonics and Fiber Technology, Nice, France (2016)
- **F. Bessin**, F. Copie, M. Conforti, A. Kudlinski, and A. Mussot, "Modulational instabilities in the weak normal dispersion region of uniform fiber ring cavities", Conference on Lasers and Electro-Optics, Munich, Germany (2017)

- F. Copie, **F. Bessin**, M. Conforti, A. Kudlinski, S. Trillo, and A. Mussot, "Observation of period-doubling dynamics of modulation instability in uniform and dispersion oscillating fiber-ring cavities", in Advanced Photonics, Zurich, Switzerland (2018)

Invited orals in peer-reviewed international conferences

- A. Mussot, C. Naveau, **F. Bessin**, P. Szriftgiser, M. Conforti, A. Kudlinski, ans S. Trillo, "Full characterisation in phase an amplitude of the Fermi Pasta Ulam recurrence process in optical fibers", International Conference on Laser Optics, St- Petersburg, Russia (2018)
- A. Mussot, C. Naveau, **F. Bessin**, P. Szriftgiser, M. Conforti, A. Kudlinski, ans S. Trillo, "Full characterisation in phase an amplitude of the Fermi Pasta Ulam recurrence process in optical fibers", Days on Diffraction, St- Petersburg, Russia (2018)
- A. Mussot, C. Naveau, **F. Bessin**, P. Szriftgiser, M. Conforti, A. Kudlinski, and S. Trillo, "Observation of the symmetry breaking of the Fermi Pasta Ulam recurrence in nonlinear optical fibers", Latin America Optics and Photonics Conference, Lima, Peru (2018)
- A. Mussot, C. Naveau, **F. Bessin**, P. Szriftgiser, M. Conforti, A. Kudlinski, and S. Trillo, "New Insights on Modulation Instability in Optical Fibers, Optical Fiber Communication Conference", San Diego, USA (2019)

Posters in peer-reviewed international conferences

- **F. Bessin**, A. M. Perego, K. Staliunas, S. K. Turitsyn, A. Kudlinski, M. Conforti, and A. Mussot, "Experimental evidence of gain-through-loss mechanism in passive fiber ring cavities: toward tunable frequency comb generation", Conference on Lasers and Electro-Optics, Munich, Germany (2019)
- **F. Bessin**, C. Naveau, M. Conforti, A. Kudlinski, A. Mussot "Phase and power characterization of seeded modulation instability in passive fiber ring cavities", Conference on Lasers and Electro-Optics, Munich, Germany (2019)

Abstract: Modulation instability (MI) in optics is a nonlinear process where a weak periodic perturbation exponentially grows at the expanse of a strong carrier wave as a result of the perfect balance between dispersion and non-linearity. In passive optical cavities, the coherent superposition between the driving field and the intra-cavity field adds a extra-degree of freedom to this mechanism that enriches its dynamics. In this thesis, we mostly led experimental study of MI in such devices made of optical fibers in unexplored regimes. In particular, we experimentally investigated this process in cavities that operate under weak normal dispersion. We showed that the MI dynamics in such regime is strongly modified compared to standard MI in cavities. We also studied the real-time dynamics of MI in the temporal domain highlighting that the generated temporal pattern can exhibit two distinct behaviors. A part of this work is also dedicated to the experimental study of the gain through loss mechanism. Under specific conditions this process can generate MI and tunable optical frequency combs. These studies are in pretty good agreement with theoretical models and numerical simulations. Finally, we explored analytically the process of coherent seeded MI. We reported that the dynamics of the process is phase-sensitive, which was confirmed experimentally by recording the power and phase evolution of the waves involved in the process.

Keywords: Nonlinear optics; optical fiber; passive fiber cavities; modulation instability

Résumé: L'instabilité de modulation (IM) en optique est un processus non-linéaire responsable de l'amplification exponentielle d'une faible perturbation périodique au dépend d'une onde porteuse de forte puissance, cela en raison du parfait équilibre entre la dispersion et la non linéarité. Dans les cavités optiques passives, la superposition entre le champ injecté dans le système et le champ intra-cavité ajoute un degré de liberté supplémentaire à ce mécanisme, ce qui enrichit sa dynamique. Dans cette thèse, nous avons principalement mené des études expérimentales de l'IM dans de tels dispositifs faits de fibres optiques, dans des régimes inexplorés. En particulier, nous avons étudié expérimentalement ce processus dans des cavités fonctionnant en régime de dispersion faible. Nous avons montré que la dynamique de l'IM dans un tel régime est fortement modifiée par rapport à celle de l'IM standard dans les cavités. Nous avons également étudié la dynamique temporelle de l'IM montrant que le motif temporel généré peut présenter deux comportements distincts. Une partie de ces travaux est également consacrée à l'étude expérimentale du mécanisme de gain induit par les pertes. Dans des conditions spécifiques, ce processus peut générer de l'IM ainsi que des peignes de fréquence ajustables. Ces études sont en bon accord avec les modèles théoriques et les simulations numériques. Dans la dernière partie de ce travail, nous avons exploré analytiquement le processus de l'IM amorcée de façon cohérente. Nous avons montré que la dynamique du processus est sensible à la phase, ce que nous confirmons expérimentalement en enregistrant l'évolution de la puissance et de la phase des ondes impliquées dans le processus.

Mots clés: Optique non-linéaire ; fibres optiques ; cavités fibrées passives ; instabilité de modulation